Correlated Charge Noise and Relaxation Errors in Superconducting Qubits

By

Christopher D. Wilen

A dissertation submitted in partial fulfillment of
the requirements for the degree of

Doctor of Philosophy
(Physics)

at the
UNIVERSITY OF WISCONSIN-MADISON
2021

Date of final oral examination: 09/21/2021

The dissertation is approved by the following members of the Final Oral Committee:
Robert F. McDermott, Professor, Physics
Victor W. Brar, Assistant Professor, Physics
Deniz Yavuz, Professor, Physics
Randall Goldsmith, Professor, Chemistry

Acknowledgements

The success of my Ph.D. would not have been possible without an enormous support network, to whom I extend my deepest appreciation and gratitude.

First and foremost, I would like to thank my advisor, Professor Robert McDermott, who guided me on several projects throughout my graduate career with a seemingly endless source of knowledge of even the most minute details. A day never went by without a new idea to try or a new theory to test. Under him, I grew from knowing virtually nothing about the field to asking my own questions and coming up with my own theories to test. And when we got him out of the lab, Robert always had a fun story to tell about things such as an exploding cryostat or secret Russian bunkers.

I would also like to thank the rest of the McDermott lab for their work and companionship during these years. In particular, I would like to thank Guilhem for taking me under his wing as I started out, Ted for kickstarting my understanding of qubits, Ivan and Alex for helping me in my quest to update the lab's software infrastructure, and Brad for teaching me all about noise. Working here would not have been the same without each of you. My work has built on the work of each and every one of the other students in the lab, whether that be already-tested fabrication recipes or the setup and wiring of cryostats, and for that I owe a great deal of gratitude.

I have been fortunate to have many mentors along the way that pushed my physics career forward. Mr. Richardson first opened my eyes to the wonders of physics in my high school physics class, teaching us how to work through fun, interesting problems (some of which I borrowed years later as a TA!). In college, there were numerous professors, students, and research opportunities to which I owe a huge thank you for sustaining my excitement with physics. After college, I was mentored by Brent Vandevender at Pacific Northwest National Lab. It was this mentorship and experience that influenced my decision to go to grad school and continue researching physics.

As I'm finishing this chapter of my physics career, I cannot thank my family enough. When I was a kid, my parents supplied me with circuit and science experiment kits and did their best to answer all my "why's?" My dad was always super supportive of my ideas and encouraged my critical thinking. My mom repeatedly exclaimed, "I can't wait until you take a physics class!" It turns out she was right about my passion for physics. My sister Anna, my grandmother, and the rest of my extended family have also offered endless encouragement and love. None of this would have been possible without my family, and I am forever grateful for their continual support.

Grad school can be frustrating, tiresome, and daunting at times. I am grateful for my huge and loving network of friends that have helped me through the hard times and provided balance to my work life. To those near and far who went on adventures with me, listened to and supported me, watched sunsets or movies with me, played frisbee with me, and generally kept me sane on this journey, thank you.

To close and bring these acknowledgments full circle, I want to share a bit of family history. My great great great (great^3) grandfather, Levi Booth, was born in New York in 1829. When he was eight years old, he was orphaned and sent to Madison to live with his childless aunt and uncle. Entering UW–Madison in the first class of 1849, he was the first student to graduate with a BA. During the commencement, he welcomed the guests in Latin and gave a speech entitled "Imperfections of the Social System." Four years later, he was one of the first graduate degree recipients, obtaining an MA in Law. So thank you, Levi, for paving the way–from a distant grandson, over a century and a half later.

Abstract

We have used Ramsey tomography to characterize charge noise in a weakly charge-sensitive superconducting qubit. We find a charge noise that scales with frequency as $1/f^{\alpha}$ over 5 decades with $\alpha = 1.93$ and a magnitude $S_q(1\,\mathrm{Hz}) = 2.9 \times 10^{-4}\ e^2/\mathrm{Hz}$. The noise exponent and magnitude of the low-frequency noise are much larger than those seen in prior work on single electron transistors, yet they are consistent with reports of frequency noise in other superconducting qubits. Moreover, we observe frequent large-amplitude jumps in offset charge exceeding $0.1e$. These large discrete charge jumps are incompatible with a picture of localized dipole-like two-level fluctuators. The data reveal an unexpected dependence of charge noise on device scale that suggest a mechanism with a large spatial footprint that could lead to correlated errors.

A crucial requirement for quantum error correction is that errors cannot be correlated. In a second set of experiments, we characterize a superconducting multi-qubit circuit and find that charge fluctuations are highly correlated on a length scale over 600 μm; moreover, discrete charge jumps are accompanied by a strong transient suppression of qubit energy relaxation time across the millimeter-scale chip. The resulting correlated errors are explained in terms of the charging event and phonon-mediated quasiparticle poisoning associated with absorption of gamma rays and cosmic-ray muons in the qubit substrate. Robust quantum error correction will require the

development of mitigation strategies to protect multiqubit arrays from correlated errors due to particle impacts.

Contents

Chapter 1

Superconducting quantum bits

1.1 Quantum bits

Classical computers operate by performing operations (gates) on bits, two-state systems usually made up of a transistor through which a current can be turned *on* (1) or *off* (0). Quantum computers operate similarly by performing operations on quantum bits, called "qubits." Qubits differ from their classical counterpart in that they need to be able to hold a quantum superposition of their *on* and *off* states:

$$|\psi\rangle = \alpha|0\rangle + \beta|1\rangle, \tag{1.1}$$

where $|\alpha|^2$ and $|\beta|^2$ are the probabilities of being in the states $|0\rangle$ and $|1\rangle$, respectively. Because the total probability $|\alpha|^2 + |\beta|^2 = 1$, it is natural to map a qubit state onto the surface of the so-called *Bloch sphere* [1], with the state alternatively being represented

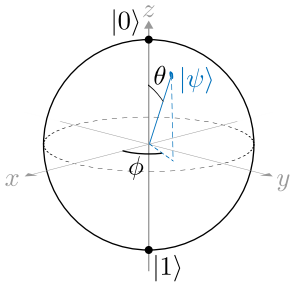

Figure 1.1: **Bloch sphere.** The computational basis of a qubit can be represented by a vector pointing to the surface of a unit sphere. Ensemble averages can lead to state vectors pointing within the sphere.

by the polar and azimuthal angles:

$$|\psi\rangle = \cos\frac{\theta}{2}|0\rangle + e^{i\phi}\sin\frac{\theta}{2}|1\rangle. \tag{1.2}$$

This is shown in Fig. 1.1. Single-qubit gates induce rotations on the Bloch sphere, and when taking into account ensemble averages, the state vector can point within the sphere. Part of the power of quantum computing comes from the unique properties of superpositions. While N classical bits can be in one of 2^N states, N qubits can be in a superposition of all the possible states, holding exponentially more information.

More generally, an architecture could be designed to use three-state "qutrits" or even higher numbers of states, but it is rare to consider anything more than two-state systems (although higher numbers of states are often considered to account for errors out of the computational basis).

There are many physical implementations of a system that can hold a quantum state that would satisfy the requirements for a qubit. Popular examples are using two of the many energy states in an atom [2–4] or ion [5, 6], quantum dots with an electron

spin in either the up or down state [7–9], or two polarizations of a photon [10–13]. In this thesis we will concetrate on qubits made with superconducting circuits, where two states can be realized with the amount of charge trapped on a capacitor, the magnitude, direction, or phase of currents, the magnitude of magnetic flux threading through a loop, or combinations of these [14–19].

1.2 Josephson junctions

Josephson junctions are nonlinear, dissipationless elements that turn out to be essential for the superconducting circuits used to construct quantum computers. A Josephson junction [20–22] is created when two superconductors are separated by a "weak link," usually a small insulating gap that gives the geometry a capacitance C. Below the superconducting temperature, some of the electrons in the conduction band of the superconductor loosely bind together ("condense") to form Cooper pairs, which behave as a gas of bosons, and can tunnel without dissipation across the insulating gap to the other superconductor. A junction acts like a capacitor and non-linear inductor in parallel, as will be shown shortly.

The condensate in a superconductor can be described by the wavefunction,

$$\Psi_i = \sqrt{n_i} e^{i\delta_i}, \tag{1.3}$$

where n_i is the number of Cooper pairs, and δ_i the quantum phase. This is called the "Ginzberg Landau Approximation." Note that the density of cooper pairs is $|\Psi_i|^2$.

When two superconductors are combined into a junction (hence the subscript i above), we can combine the parameters and use $n = n_1 - n_2$ and $\delta = \delta_1 - \delta_2$. The voltage across the junction is

$$V = \frac{Q}{C} = \frac{ne}{C}, \tag{1.4}$$

where there is a difference in charge of e on each side when a Cooper pair (charge $2e$) tunnels across. We can now go back and plug the wavefunction into the Hamiltonian for two weakly coupled (coupling constant K) systems:

$$i\hbar\frac{\partial\Psi}{\partial t} = U_i\Psi_i - K\Psi_j \tag{1.5}$$

$$\frac{\dot{n}_i}{2\sqrt{n_i}} + i\sqrt{n_i}\dot{\delta}_i = -iU_i\sqrt{n_i} - iK\sqrt{n_J}e^{i(\delta_j-\delta_i)}. \tag{1.6}$$

Using the potential energy difference $U_1 - U_2 = qV = (2e)\frac{ne}{C}$, and $\dot{n}_1 = -\dot{n}_2$, we can equate the imaginary and real parts:

$$\dot{\delta} = \dot{\delta}_1 - \dot{\delta}_2 = -\frac{2ne^2}{\hbar C} - \frac{K}{\hbar}\left(\sqrt{\frac{n_2}{n_1}} - \sqrt{\frac{n_1}{n_2}}\right)\cos\delta \tag{1.7}$$

$$\dot{n} = \dot{n}_1 - \dot{n}_2 = \frac{2K}{\hbar}\sqrt{n_1 n_2}\sin\delta. \tag{1.8}$$

If we assume $n_1 \approx n_2$, the second term in Eq. (1.7) goes away. It should also be noted that solving the Schröinger equation shows that $n_1 + n_2$ is a constant. Rewriting Eqs. (1.7) and (1.8) in terms of current $I = 2e\dot{n}$, we can arrive at the canonical equations

for a Josephson junction [23–25]:

$$V = \frac{\hbar}{2e}\dot{\delta} = \frac{\Phi_0}{2\pi}\dot{\delta} \tag{1.9}$$

$$I = I_0 \sin\delta. \tag{1.10}$$

In Eq. (1.9), we defined the magnetic flux quantum $\Phi_0 = h/2e$. The critical current I_0 depends on the parameters of the junction, the temperature, etc. These two formulas describe both the AC and DC Josephson effects.

The *DC Josephson Effect* takes place when we have a constant phase across the junction, and simply states that there will be a constant current of cooper pairs tunneling through.

The *AC Josephson Effect* describes what happens when a voltage is applied across the junction. If the voltage is constant, the phase has to vary according to the relation $\dot{\delta} = V(2e)/\hbar$. Plugging this back into Eq. (1.10), we find that the current oscillates at the *Josephson frequency* $\omega = 2eV/\hbar = 2\pi V/\Phi_0$.

The *Josephson energy* is the potential energy accumulated in a Josephson junction when a supercurrent flows through it. One can think of a Josephson junction as a non-linear inductance which accumulates (magnetic field) energy when a current passes through it. In contrast to real inductance, no magnetic field is created by a supercurrent in a Josephson junction – the accumulated energy is the Josephson energy. Imagine that initially at time $t = 0$ the junction was in the ground state $\delta = 0$ and finally at

time t the junction has the phase δ. The work done on the junction, and therefore the energy acquired by the junction, is

$$U = \int_0^t IV\,dt = \int_0^t (I_0 \sin\delta)\left(\frac{\Phi_0}{2\pi}\frac{d\delta}{dt}\right)dt = \frac{I_0\Phi_0}{2\pi}\int_0^\phi \sin\delta\, d\delta = \frac{I_0\Phi_0}{2\pi}(1-\cos\delta), \tag{1.11}$$

which sets the characteristic energy scale, $E_J = \frac{\Phi_0 I_0}{2\pi}$.

1.2.1 RCSJ model

Real-world junctions are not ideal, of course. In addition to the supercurrent of Cooper pairs described by (1.10), some current will flow classically through the weak link of the junction, which has some resistance R. We can represent a junction as a resistor, a capacitance C, and an ideal junction, in parallel. This is called the resistively and capacitively shunted junction (RCSJ) model [26, 27], shown in Fig. 1.2b. The full current through all the branches is

$$I = I_0 \sin\delta + \frac{V}{R} + C\dot{V} \tag{1.12}$$

$$= I_0 \sin\delta + \frac{\Phi_0}{2\pi R}\frac{d\delta}{dt} + C\frac{\Phi_0}{2\pi}\frac{d^2\delta}{dt^2}. \tag{1.13}$$

Introducing the washboard potential gives us insight into the different regimes of the junctions behavior.

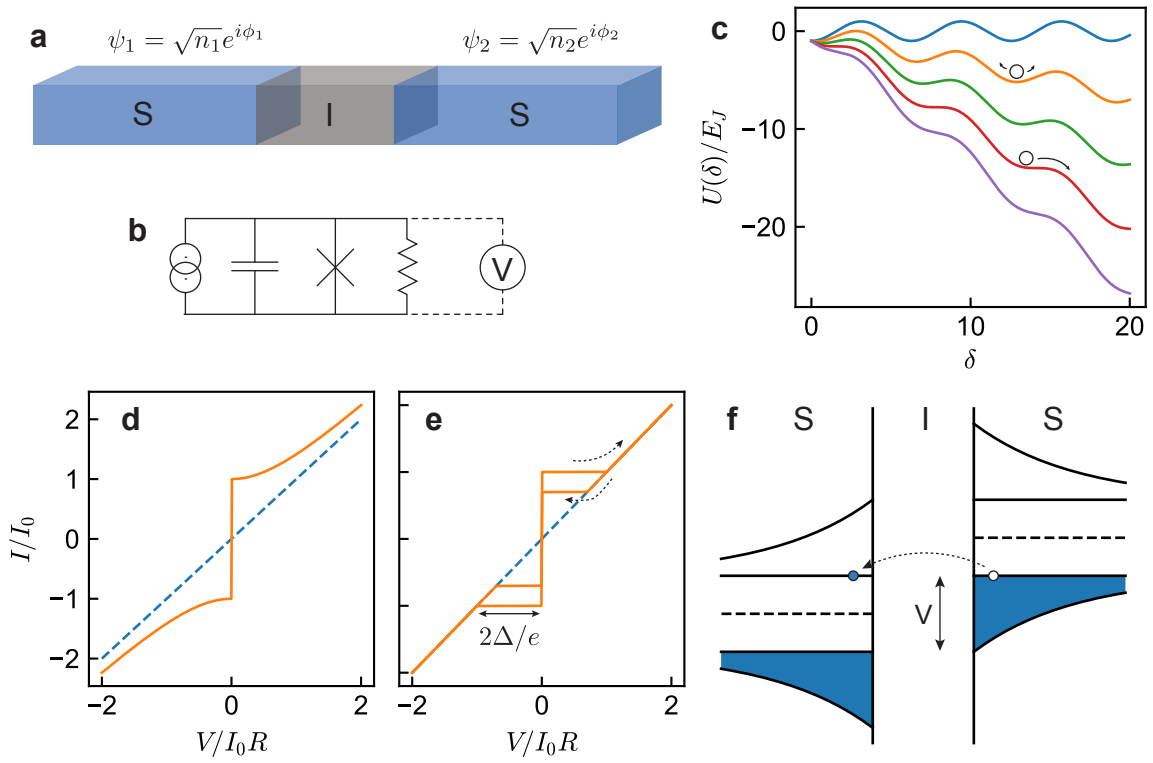

Figure 1.2: **Josephson junctions.** (**a**) Cartoon of a Josephson junction, with two superconductors (S, blue) separated by a thin insulating gap (I, grey). (**b**) Circuit diagram for the RCSJ model of a junction. The 'X' symbol represents an ideal Josephson junction. (**c**) Tilted washboard potential for bias currents $I/I_0 = \{0, 1/3, 2/3, 1, 4/3\}$ from blue to purple. In the supercurrent state (ex: orange curve), a phase particle is trapped in a local minimum of the potential and oscillates at the plasma frequency. In the voltage state (ex: red curve), the phase particle rolls down the "tilted washboard." (**d**) IV curve for an overdampled junction given by Eq. 1.34. (**e**) IV curve for an underdamped junction. As the current increases, the phase particle escapes and starts rolling down the potential, moving the junction out of the supercurrent state and into the voltage state. As the current decreases, a phase particle needs to slow down enough to become retrapped in a local minimum of the potential. In an underdamped junction, this requires a lower current than it took to start the particle rolling, causing the hysteresis seen here. (**f**) Energy diagram for a junction in the voltage state. With a high enough voltage raising the energy of one side, electrons can tunnel across the gap and become unpaired quasiparticles.

1.2.2 Washboard potential

A particle with mass m under a force of a spring $F_s = -kx$ and a damping force $F_d = -c\dot{x}$ moves satisfying the differential equation $\ddot{x} + \frac{c}{m}\dot{x} + \sqrt{\frac{k}{m}}x = 0$. We can rearrange Eq. (1.13) into a similar form:

$$C\left(\frac{\Phi_0}{2\pi}\right)^2 \frac{d^2\delta}{dt^2} + \left(\frac{\Phi_0}{2\pi}\right)^2 \frac{1}{R}\frac{d\delta}{dt} + \frac{\Phi_0}{2\pi}(I_0 \sin\delta - I) = 0. \tag{1.14}$$

The analogy can easily be made, then, between the dynamics of a junction and a particle with mass $\left(\frac{\Phi_0}{2\pi}\right)^2 C$ moving in a potential

$$U = \int F d\delta = -\frac{\Phi_0 I_0}{2\pi}\left(\frac{I}{I_0}\delta + \cos\delta\right) \tag{1.15}$$

$$= -E_J\left(\frac{I}{I_0}\delta + \cos\delta\right). \tag{1.16}$$

with damping force. This is commonly referred to as the *washboard potential*, and using this analogy we are able to analyze the dynamics of the system.

There are two behaviors a junction can exhibit, shown in Fig 1.2c. If the phase particle has too much energy, it will jump out of one of the wells and cascade down the potential landscape. This is known as the *voltage state* because as the particle slides down the tilted washboard, its phase changes rapidly and a voltage across the junction is generated as per Eq. (1.9). The particle can also escape if the washboard becomes steep enough ($I > I_0$) that no wells form, or if the particle tunnels out of one of the wells.

Once a particle is out of the well, we can get an idea of the steady-state junction dynamics by setting the first term (phase acceleration) in Eq. (1.14) to zero. It is then evident that the damping term (middle) and the potential term (right) need to balance each other. The potential term should always be negative in the voltage state, since $I > I_0$ is usually required to get the particle out of the well. The phase particle therefore slips down the washboard at a constant averaged rate, with the damping term defining the voltage across the junction. As I is increased, the voltage also increases to balance out the damping term and the potential term. If I is decreased below I_0, the particle can still slide down the washboard without being caught in a well. If I gets low enough, the particle will eventually become trapped in a well again, but if this transition happens below I_0, there is a voltage state below the critical current, causing hysteresis in the junction IV curve.

It should be noted that the voltage as the particle slips down the washboard is not constant. As the phase particle whips down a steep portion of the potential, and slows down as it overcomes the well wall, single flux quantum (SFQ) pulses are emitted in time with the passing of each well. The pulses come fast enough that it is the time averaged voltage of these pulses that is usually measured, which was already calculated above in Eq. (1.34).

In addition, a voltage caused by a junction in the voltage-state can break Cooper pairs into unpaired electrons, called quasiparticles (Fig 1.2f). The more phase slips of

the junction, and the higher the energy released in each slip (E_J), the more quasiparticles are generated.

Alternatively, the phase particle can sit in the bottom of one of the potential wells and oscillate around the minimum. This is known as the *zero-voltage state* or *current state*, because the potential does not change greatly from its local minimum δ_0, and so, according to Eq. (1.9), the voltage across the junction is small. Let us look at the small deviations around this minimum, starting with Eq. (1.10):

$$I = I_0 \sin \delta_0 \tag{1.17}$$

$$dI = (I_0 \cos \delta) d\delta_0 \tag{1.18}$$

$$dV = \frac{\Phi_0}{2\pi} \frac{d\delta}{dt} \tag{1.19}$$

$$= \frac{\Phi_0}{2\pi} \frac{1}{I_0 \cos \delta_0} \frac{dI}{dt}. \tag{1.20}$$

This gives rise to what is known as the *Josephson Inductance*,

$$L_J = \frac{\Phi_0}{2\pi} \frac{1}{I_0 \cos \delta_0}. \tag{1.21}$$

Although no energy is actually stored in a magnetic field, the relationship in the last line above looks like that of an inductor. Recall that this "inductance" is in parallel with the capacitance across the junction, creating a simple LC resonator. The resonator

oscillates at the *Plasma Frequency*,

$$\omega_p = \frac{1}{\sqrt{LC}} = \sqrt{\frac{2\pi I_0 \cos\delta_0}{\Phi_0 C}} \tag{1.22}$$

$$= \sqrt{\frac{2\pi I_0}{\Phi_0 C}} \left[1 - \left(\frac{I}{I_0}\right)^2\right]^{1/4}, \tag{1.23}$$

which is the frequency at which the particle stuck in a well of the washboard potential oscillates around a minimum. In the second line, we simply rewrite the $\cos\delta_0$ term using Eq. (1.10). Alternatively, we can reach this same result by using $m = \left(\frac{\Phi_0}{2\pi}\right)^2 C$ in

$$\omega_p = \sqrt{\frac{U''(\delta_0)}{m}}. \tag{1.24}$$

In general, inductances follow $L = 1/U''(\delta)$.

Only a limited number of states can fit in each well. To find an approximation for this, we first expand the potential (around $\delta = \pi/2$) to approximate it as a cubic:

$$U(\delta) = -\frac{\Phi_0}{2\pi}(I\delta + I_0\cos\delta) \tag{1.25}$$

$$= -\frac{\Phi_0}{2\pi}\left[I\delta + I_0 \sin\left(\frac{\pi}{2} + \delta\right)\right] \tag{1.26}$$

$$= -\frac{\Phi_0}{2\pi}\left\{I\delta + I_0 \sin\left[-\left(\delta - \frac{\pi}{2}\right) + \frac{1}{6}\left(\delta - \frac{\pi}{2}\right)^3\right]\right\}. \tag{1.27}$$

By setting the derivative to zero, we find the critical points to be $\delta_c = \pi/2 \pm \sqrt{2}\sqrt{1 - I/I_0}$.

Plugging this back into Eq. (1.27), we find a barrier height of

$$= \frac{4\sqrt{2}}{3}\frac{\Phi_0}{2\pi}I_0\left(1-\frac{I}{I_0}\right)^{3/2}, \tag{1.28}$$

which can be used to estimate of the number of states in the well through

$$n \approx \frac{\Delta U}{\hbar\omega_p}. \tag{1.29}$$

1.2.3 Under- and over-damped junctions

To better understand the retrapping dynamics of a junction's phase particle, we can rewrite Eq. (1.13) as

$$\frac{I}{I_0} = \sin\delta + \frac{d\delta}{d\tau} + \beta_C\frac{d^2\delta}{d\tau^2}, \tag{1.30}$$

where we have plugged in Eq. 1.9 to get Eq. 1.13 and then simplified the expression by defining the Josephson time constant,

$$\tau_J = \frac{\Phi_0}{2\pi I_0 R}, \tag{1.31}$$

the Stewart-McCumber Parameter,

$$\beta_C = \frac{\tau_{RC}}{\tau_J} = \frac{RC}{\tau_J} = \frac{2\pi R^2 C}{\Phi_0}, \tag{1.32}$$

and $\tau = t/\tau_J$.

We can now analyze two limits: the overdamped regime when $\beta_C \ll 1$ and the

underdamped regime when $\beta_C \gg 1$. In an *overdamped junction*, $\tau_J \gg \tau_{RC}$, and we can simplify Eq. (1.30) to

$$\frac{I}{I_0} = \sin\delta + \frac{d\delta}{d\tau}. \tag{1.33}$$

The solution to this for $I > I_0$ is a phase $\delta(t)$ oscillating according to a tangent function with a period $\Theta = 2\pi\tau_J/\sqrt{(I/I_0)^2 - 1}$. It is useful to look at the average voltage across the junction. Integrating over one period, we can obtain the relation

$$\langle v(t)\rangle = IR\sqrt{1 - \left(\frac{I_0}{I}\right)^2}, \tag{1.34}$$

which is plotted in Fig. 1.2d. The dotted line shows the IV curve for a resistor with resistance R of the junction, to which the junction IV curve asymptotically trends. To get to the voltage state, cooper pairs need to be broken, so the voltage difference between the top of the current branch and the dotted line is the voltage needed to break a cooper pair, or $2\Delta/e$.

In an *underdamped junction*, $\tau_J \ll \tau_{RC}$, and the acceleration of the phase particle has to be overcome by the damping for it to retrap. Once it has escaped a well, the phase particle continues to roll down the tilted washboard even after the current has dropped below I_0 again, giving the IV curve the historesis described in the previous section and shown in Fig. 1.2e. Normally one does not want a hysteric junction. Choosing a value of $\beta_C > 1$ removes this hysteresis.

Both underdamped and overdamped limits have a static solution for $I < I_0$:

$$\delta = \sin^{-1} \frac{I}{I_0}. \tag{1.35}$$

For a constant δ, there will be no voltage across the junction. This so-called "current branch" appears as a vertical line near the origin in the IV curves. Between these limiting cases, analytic solutions cannot be found for the differential equation, and numerical methods must be used.

1.3 Transmon qubits

The most commonly used superconducting qubit today is the transmission line shunted plasma oscillation qubit [28], or transmon for short. An isolated transmon is simply a Josephson Junction shunted with a capacitor, as shown in Fig. 1.4. The capacitor and junction separate a "qubit island" from ground, which physically is usually a quasi-continuous plane of metal surrounding the qubit island. Charge can tunnel on and off of this qubit island. Following Ref. [29], we can quantize this circuit, starting with the definitions for branch flux and branch charge:

$$\phi_b(t) \equiv \int_{-\infty}^{t} v_b(t')dt' \tag{1.36}$$

$$Q_b(t) \equiv \int_{-\infty}^{t} i_b(t')dt'. \tag{1.37}$$

Taking the derivative of Eq. 1.36 gives us $V = \dot{\phi}$. In addition to allowing us to trivially write down the energy in a capacitor, this relation helps us relate ϕ to position and V to velocity. With this in mind, and using the energy for the Josephson junction that we calculated in the last section ($I = 0$), we can write down the Lagrangian for the circuit in Fig. 1.3:

$$\mathcal{L} = \frac{1}{2}C\dot{\phi}^2 - \left[-E_J \cos\left(\frac{2\pi}{\phi_0}\phi\right)\right]. \tag{1.38}$$

Calculating the generalized momentum,

$$p_\phi = \frac{\partial \mathcal{L}}{\partial \dot{\phi}} = C\dot{\phi}, \tag{1.39}$$

we perform the simple redefinition $C\dot{\phi} = CV = q$ and find that the generalized momentum is just the charge q on the qubit island (capacitor). From here, it is simple to write out the Hamiltonian for the system:

$$\begin{aligned}
\mathcal{H} &= \dot{\phi}p_\phi - \mathcal{L} && (1.40)\\
&= C\dot{\phi}^2 - \frac{1}{2}C\dot{\phi}^2 - E_J \cos\left(\frac{2\pi}{\phi_0}\phi\right) && (1.41)\\
&= \frac{q^2}{2C} - E_J \cos\left(\frac{2\pi}{\phi_0}\phi\right). && (1.42)
\end{aligned}$$

Promoting ϕ and it's generalized momentum q to quantum operators $\hat{\phi}$ and $\hat{q}$ gives the commutation relation,

$$[\hat{\phi}, \hat{q}] = i\hbar. \tag{1.43}$$

Another change of variables leads to a more natural coordinate system:

$$\delta = \frac{2\pi\hat{\phi}}{\phi_0}$$
$$n = \frac{\hat{q}}{2e}.$$

Here we have gone from flux $\hat{\phi}$ to the superconducting phase δ across the junction, where ϕ_0 is the flux quantum, and from the charge q on the qubit island to the number of cooper pairs n that have tunneled onto the conducting island that makes up the qubit, where e is the fundamental charge. We have also omitted the hats on $\hat{\delta}$ and $\hat{n}$, and will do so for all operators going forward. They are, however, still quantum operators, with the commutation relation $[\delta, n] = i$. Defining a charging energy as the additional energy stored on the capacitor with the addition of a single unit of charge e,

$$E_C = \frac{e^2}{2C}, \tag{1.44}$$

the Hamiltonian can be rewritten as

$$\mathcal{H} = 4E_C n^2 - E_J \cos\delta. \tag{1.45}$$

The n^2 term represents the kinetic energy of the system, while the $\cos\delta$ represents the potential energy. This Hamiltonian can be solved exactly, but first it is useful to use a perturbative approach to find the first few energy levels. Asserting $E_C \ll E_J$,

we can imagine a "phase particle" trapped near the bottom of a potential well with shape $E_J \cos\delta$, oscillating around $\delta = 0$. Transmon qubits, which are generally have an E_J/E_C in the range of 50-100, easily satisfy this condition, allowing us to expand the potential well:

$$-E_J \cos\delta \approx -E_J \left(1 - \frac{\delta^2}{2!} + \frac{\delta^4}{4!} + \dots\right). \tag{1.46}$$

Using this expansion to second order and discarding the the constant term, the Hamiltonian,

$$\mathcal{H} = 4E_C n^2 + \frac{1}{2} E_J \delta^2 \tag{1.47}$$

is directly comparable to the well-studied quantum harmonic oscillator, with a mass C and an angular frequency ω given by

$$\hbar\omega = \sqrt{8E_J E_C}. \tag{1.48}$$

Following the normal procedure for the quantum harmonic oscillator, the Hamiltonian can be rewritten in terms of raising and lowering ladder operators $a^\dagger$ and a:

$$\mathcal{H} = \hbar\omega \left(a^\dagger a + \frac{1}{2}\right), \tag{1.49}$$

$$a = \sqrt{\frac{E_J}{2\hbar\omega}}\delta + 2i\sqrt{\frac{E_C}{\hbar\omega}}n \tag{1.50}$$

$$a^\dagger = \sqrt{\frac{E_J}{2\hbar\omega}}\delta - 2i\sqrt{\frac{E_C}{\hbar\omega}}n. \tag{1.51}$$

This form of the Hamiltonian brings forth a crucial piece of understanding. The corresponding eigen-energies of this Hamiltonian are $E_n = \left(n + \frac{1}{2}\right)\hbar\omega$, with $n \in \{1, 2, \dots\}$ denoting the n'th state. These discrete energies are equally spaced by an energy difference of $\hbar\omega$, preventing the isolated addressing of the transition between the ground and excited state; a tone driving the transition will equally drive transitions between the first excited state and the second excited state, etc. This system is, in fact, the same as if we replaced the Josephson junction with an inductor $L = \phi_0^2/4\pi^2 E_J$. To see the equal spacing of the energy levels in the transmon qubit fall away, we need to incorporate the fourth order phase term in the expansion of the Hamiltonian.

We do so using perturbation theory, with our second order Hamiltonian $\mathcal{H}_{QHO} = \hbar\omega(a^\dagger a + 1/2)$ undergoing the perturbation of the fourth order term:

$$\mathcal{H}' = -E_J\frac{\delta^4}{4!} \tag{1.52}$$

$$= -\frac{E_C}{12}\left(a + a^\dagger\right)^4. \tag{1.53}$$

Calculating the first few energy levels, we get:

$$E_n = \langle n|\mathcal{H}_{QHO}|n\rangle + \langle n|\mathcal{H}'|n\rangle \tag{1.54}$$

$$E_0 = \frac{1}{2}\hbar\omega - \frac{E_C}{12}(3) \tag{1.55}$$

$$E_1 = \frac{3}{2}\hbar\omega - \frac{E_C}{12}(15) \tag{1.56}$$

$$E_2 = \frac{5}{2}\hbar\omega - \frac{E_C}{12}(39) \tag{1.57}$$

$$E_n = \hbar\omega\left(n + \frac{1}{2}\right) - \frac{E_C}{12}\left(6n^2 + 6n + 3\right). \tag{1.58}$$

Already we can see that the energy levels are no longer evenly spaced. More precisely, the energy spacing is given by:

$$E_1 - E_0 = \hbar\omega - E_C \tag{1.59}$$

$$E_2 - E_1 = \hbar\omega - 2E_C. \tag{1.60}$$

In terms of frequency, this gives us a difference between energy spacing of

$$\alpha \equiv \omega_{12} - \omega_{01} = -\frac{E_C}{\hbar}, \tag{1.61}$$

which we call the "anharmonicity" α of the qubit. In the next section we will learn how to drive transitions between the states of our qubit. The larger the anharmonicity, the more uneven the energy spacing is between states, and the less likely it is for our qubit to be excited into a higher state outside the computational basis.

We have now seen that to second order in phase, the transmon acts just like a capacitor and inductor in parallel, with quantized energy levels that are evenly spaced by $\hbar\omega$. Keeping a fourth order term changes this energy spacing such that our oscillator is "anharmonic," with energy spacing that decreases with increasing state number. Now that we have some intuition for the system, let us return to our original Hamiltonian in Eq. 1.45. This can be solved in either the charge basis or the phase basis.

In the phase representation, we can replace n, which represents a momentum, with a derivative with respect to position ϕ [25]:

$$n = \frac{1}{i}\frac{\partial}{\partial\phi}. \tag{1.62}$$

This results in the Hamiltonian

$$-4E_C\frac{\partial^2}{\partial\phi^2}\psi(\delta) - E_J\cos\delta\psi(\delta) = E\psi(\delta), \tag{1.63}$$

and we enforce the periodic boundary condition $\psi(\delta) = \psi(\delta + 2\pi)$. This Hamiltonian can be solved exactly using Mathieu functions, giving wavefunctions and eigen energies that match those we found using perturbation theory. These are shown in Fig. 1.3a.

It is potentially more instructive to solve this Hamiltonian in the charge basis, but there are no analytic solutions. We first need to convert $\cos\delta = \left(e^{i\delta} - e^{-i\delta}\right)/2$ into the charge basis, which we do by invoking the relation

$$e^{\pm i\delta}|n\rangle = |n \pm 1\rangle. \tag{1.64}$$

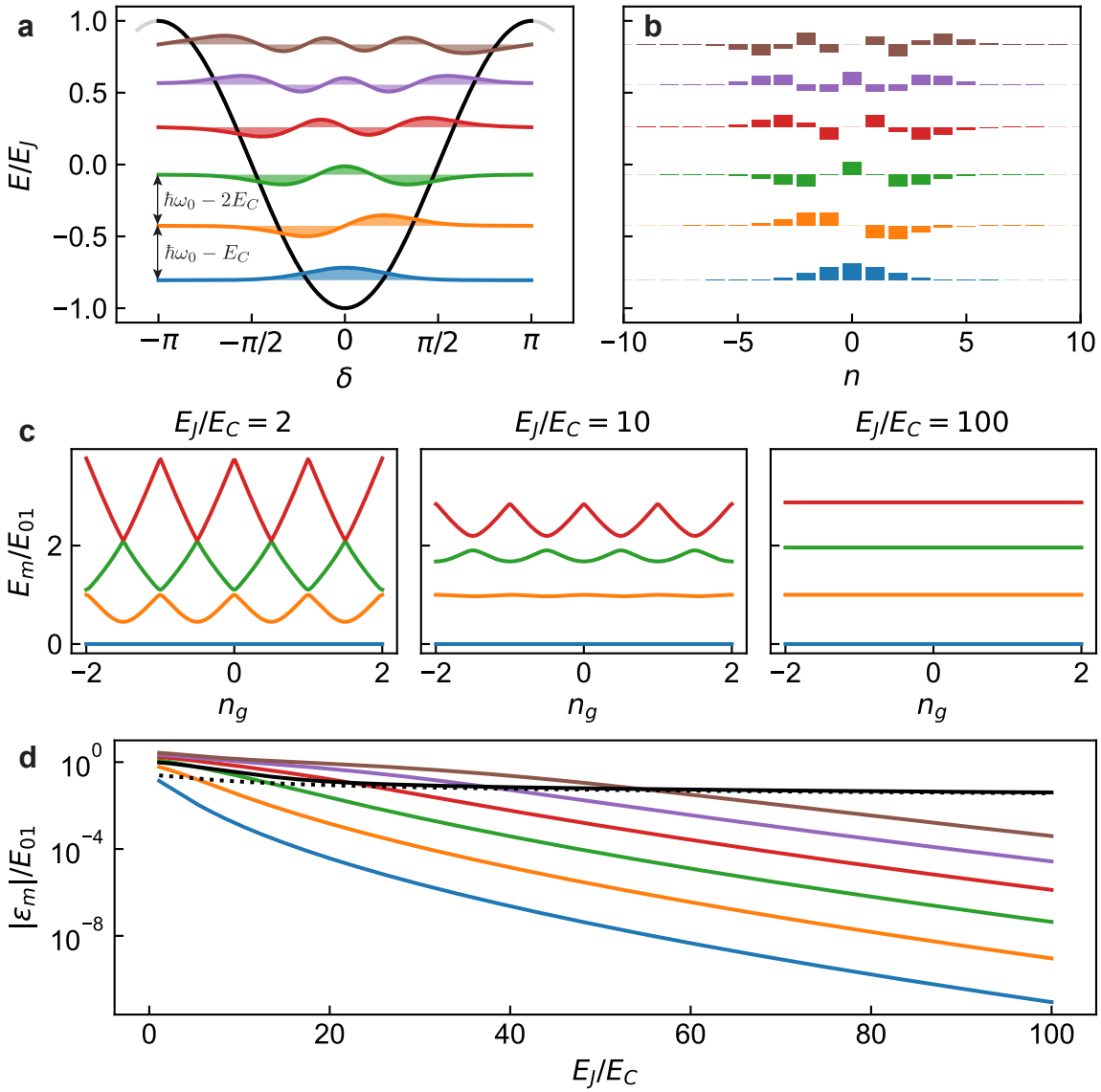

Figure 1.3: **Wavefunctions and charge dispersion of transmon qubits.** In all panels, the state number $|m\rangle$ increases with increasing energy, so blue = $|0\rangle$, orange = $|1\rangle$, etc. (**a**) Wavefunctions in the phase basis for a transmon qubits. (**b**) Wavefunctions for a transmon in the charge basis, solved from a 31×31 matrix. (**c**) Energy spectra for different E_J/E_C ratios. As the ratio increases, charge dispersion is exponentially supressed. (**d**) Exponential suppression of charge dispersion as a function of E_J/E_C. Anharmonicity, however, does not fall off as rapidly; This is shown by the solid black line, with the dotted line showing E_C/E_{01}, representing the asymptotic behavior of the anharmonicity.

With this we can rewrite our Hamiltonian in the charge basis,

$$\mathcal{H} = \sum_n \left(4E_C n^2 |n\rangle\langle n| - \frac{E_J}{2} \left(|n+1\rangle\langle n| + |n-1\rangle\langle n| \right) \right) \tag{1.65}$$

$$= \begin{array}{c} \\ \langle -2| \\ \langle -1| \\ \langle 0| \\ \langle 1| \\ \langle 2| \\ \\ \end{array} \begin{array}{c} \begin{array}{ccccccc} |-2\rangle & |-1\rangle & |0\rangle & |1\rangle & |2\rangle & & \end{array} \\ \begin{pmatrix} \ddots & & & & & & \\ & 4E_C(-2)^2 & -E_J/2 & & & & \\ & -E_J/2 & 4E_C(-1)^2 & -E_J/2 & & & \\ & & -E_J/2 & 0 & -E_J/2 & & \\ & & & -E_J/2 & 4E_C(1)^2 & -E_J/2 & \\ & & & & -E_J/2 & 4E_C(2)^2 & \\ & & & & & & \ddots \end{pmatrix} \end{array}. \tag{1.66}$$

Although there are no analytic solutions to this Hamiltonian, it is straightforward to solve this matrix analytically, with the results shown in Fig. 1.3b.

1.4 Transmon drive

To use the simple circuit in Fig. 1.4b as a qubit, we need to be able to drive transitions between the states. To do so, we capacitively couple a bias line to the qubit island,

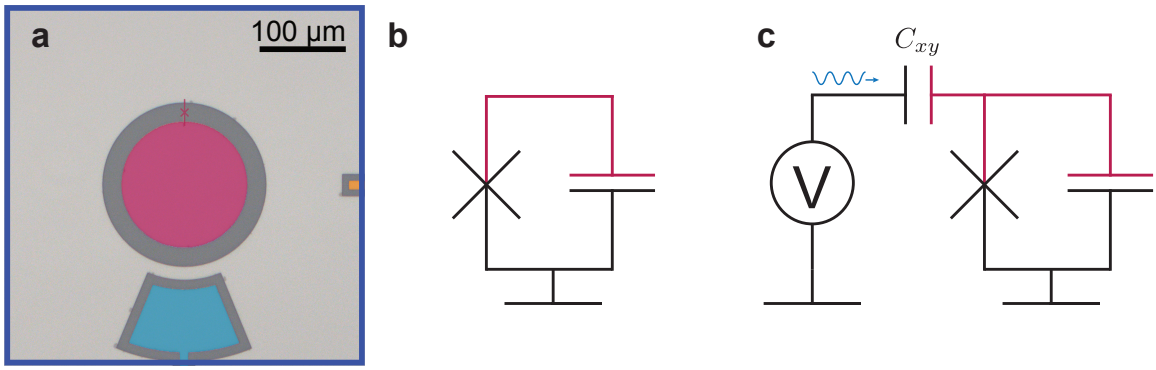

Figure 1.4: **Transmon qubits.** (**a**) A representative micrograph of a transmon qubit. The pink qubit island is separated from the light grey ground plane by a josephson junction at the top of the circle, and has a self-capacitance to the ground plane. The qubit island is capacitively coupled to a readout resonator, the end of which is shown in blue beneath the qubit. (**b**) The circuit diagram for an isolated transmon. (**c**) Transitions in the isolated transmon shown in (b) can be driven by capacitively coupling signals to the qubit island.

as shown in part (c) of the same figure. As in the last section, our analysis of this circuit starts with the writing down of the Lagrangian, which now includes a term for the energy in the capacitor coupling the drive:

$$\mathcal{L} = \frac{1}{2}C_{xy}\left(\dot{\phi} - V_d(t)\right)^2 + \frac{1}{2}C\dot{\phi}^2 + E_J \cos\left(\frac{2\pi}{\phi_0}\phi\right). \tag{1.67}$$

This time the generalized momentum is

$$p_\phi = \frac{\partial \mathcal{L}}{\partial \dot{\phi}} = C_\Sigma \dot{\phi} - C_{xy}V_d(t) \equiv q, \tag{1.68}$$

where we have defined $C_\Sigma \equiv C_{xy} + C$. From here, the Hamiltonian falls out as

$$\mathcal{H} = \dot{\phi} p_\phi - \mathcal{L} \tag{1.69}$$

$$= \frac{q^2}{2C_\Sigma} - E_J \cos\left(\frac{2\pi}{\phi_0}\phi\right) + \frac{C_{xy}}{C_\Sigma} q V_d(t) \tag{1.70}$$

$$= 4E_C \left(n - n_g\right)^2 - E_J \cos\delta, \tag{1.71}$$

where we follow last section in making the substitutions $n = -q/2e$, $n_g = C_{xy}V_d(t)/2e$, and $\delta = 2\pi\phi/\phi_0$ as before. Additionally, we have dropped a constant n_g^2 term and have slightly changed our definition of $E_C = e^2/2C_\Sigma$ to incorporate the coupling capacitance as well as the junction capacitance. Note that n_g is a time dependent quantity depending on the drive voltage $V_d(t)$, but the dependence has been dropped from the notation for simplicity.

This Hamiltonian can be solved as above, either in the phase basis (resulting in solutuions using Mathieu functions) or by changing the $n^2 \to (n - n_g)^2$ in the diagonal of the matrix in Eq. 1.66. The resulting eigen-energies can be plotted as a function of n_g, as shown in Fig. 1.3. Each energy level of the transmon fluctuates with offset charge, introducing a path to decoherence. As external electric fields closing on the qubit island change in an uncontrolled way (ex: a charge moving within the chip substrate), the qubit frequency can change. This will be explained in detail in later chapters, where we measure this "charge noise." Fortunately, as the E_J/E_C ratio

increases, the "charge dispersion" caused by changes in n_g decreases exponentially, as can be seen in Fig. 1.3, where the energy bands become flatter with increasing E_J/E_C. More precisely, the charge dispersion of the m'th energy level goes as [28]

$$\epsilon_m \equiv E_m(n_g = 1/2) - E_m(n_g = 0) \tag{1.72}$$

$$\simeq (-1)^m E_C \frac{2^{4m+5}}{m!}\sqrt{\frac{2}{\pi}}\left(\frac{E_J}{2E_C}\right)^{\frac{m}{2}+\frac{3}{4}} e^{-\sqrt{8E_J/E_C}}. \tag{1.73}$$

Keeping the frequency $f \propto \sqrt{E_J E_C}$ constant, the anharmonicity $\alpha = -E_C$ will decrease as $(E_J/E_C)^{-1/2}$. Ideally, a qubit will have a large anharmonicity to help isolate the 01 transition as much as possible, while having a low charge dispersion to reduce decoherence from charge noise. Although both the anharmonicity and the charge dispersion decrease with increasing E_J/E_C, the charge dispersion decreases much faster, and using an E_J/E_C ratio in the range of 50-100 gives us a qubit that is mostly insensitive to charge noise and with an anharmonicity large enough to drive reasonably fast gates without driving the qubit into higher levels.

In a moment we will show that driving the qubit with a coherent tone at the qubit frequency f_{01} through the capacitor C_{xy} will induce rotations of the qubit state around the x- and y-axes of the Bloch sphere. Transitions to higher states can also be realized through driving at other transition frequencies, but for pulse lengths beyond a few nanoseconds, the Fourier components of the drive signal are low enough at these frequencies that this "leakage" is not generally a large concern. For more information

about pulse shaping to get faster and higher fidelity gates, see Ref. [30]. Under the assumption that higher level states are out of the picture, it is useful at this point to approximate the qubit as a two-level system.

Working with a the harmonic approximation of the transmon and limiting it to only the first two levels allows the following substitutions to be made to the Hamiltonian:

$$a \to \sigma_- \tag{1.74}$$

$$a^\dagger \to \sigma_+ \tag{1.75}$$

$$a + a^\dagger \to \sigma_x \tag{1.76}$$

$$i(a^\dagger - a) \to \sigma_y \tag{1.77}$$

$$1 - 2a^\dagger a = 1 - 2n \to \sigma_z. \tag{1.78}$$

Here the σ operators are the normal Pauli operators. We leave it as an exercise for the reader to show that making these substitutions does not affect how each operator acts on the states $|0\rangle$ and $|1\rangle$. The q operator is transformed,

$$q = -i\sqrt{\frac{\hbar\omega C_\Sigma}{2}}(a - a^\dagger) \tag{1.79}$$

$$= \sqrt{\frac{\hbar\omega C_\Sigma}{2}}\sigma_y, \tag{1.80}$$

resulting in a rewrite of the Hamiltonian in Eq. 1.70 to

$$\mathcal{H} = \frac{\hbar\omega_{01}}{2}\sigma_z + \frac{C_{xy}}{C_\Sigma}V_d(t)Q_{\text{zpf}}\sigma_y, \tag{1.81}$$

where we define the zero-point charge fluctuations $Q_{\text{zpf}} = \sqrt{\hbar\omega_{01}C_\Sigma/2}$ and include the anharmonicity in the frequency, using $\omega_{01} = (\sqrt{8E_JE_C} - E_C)/\hbar$.

Moving to the interaction picture gives good intuition for how different drive functions affect the qubit. We split the above Hamiltonian into two parts, a base term $\mathcal{H}_0 = \frac{\hbar\omega_{01}}{2}\sigma_z$, and a time-dependent interaction term $V(t) = \hbar\Omega_R\sigma_y$, where we define the angular Rabi frequency as

$$\Omega_R \equiv \frac{1}{\hbar}\frac{C_{xy}}{C_\Sigma}V_d(t)Q_{\text{zpf}}. \tag{1.82}$$

Applying the time-dependent Schröinger equation to $\mathcal{H}_0$ shows us that the qubit state vector precesses around the z-axis on the Bloch sphere at a rate ω_{01}.

In the interaction picture, the qubit state moves only according to the interaction $V(t)$, while the operator moves according to $\mathcal{H}_0$. This is often called the *rotating frame* and is effectively moving to a coordinate system that co-rotates with the precession. To illustrate the rotating frame, let us look at a simple example, where the qubit frequency has some small time dependence:

$$\omega_q(t) = \omega_{01} + \delta\omega(t), \tag{1.83}$$

giving us a the Hamiltonian

$$\mathcal{H} = \underbrace{\frac{\hbar\omega_{01}}{2}\sigma_z}_{\mathcal{H}_0} + \underbrace{\frac{\hbar\delta\omega(t)}{2}\sigma_z}_{V(t)}. \tag{1.84}$$

An arbitrary state on the Bloch sphere is given by

$$\psi = \begin{pmatrix} \cos(\theta/2)e^{-i\phi/2} \\ \sin(\theta/2)e^{+i\phi/2} \end{pmatrix} = \begin{pmatrix} \alpha_0 \\ \alpha_1 \end{pmatrix} \tag{1.85}$$

Inserting ψ into the time dependent Schröinger equation in the interaction picture,

$$i\hbar\frac{\partial\psi}{\partial t} = V(t)\psi, \tag{1.86}$$

we find that the state evolves as

$$\alpha_0(t) = \alpha_0(t=0)e^{-i\delta\omega t/2} \tag{1.87}$$

$$\alpha_1(t) = \alpha_1(t=0)e^{i\delta\omega t/2}, \tag{1.88}$$

indicating that a variation in qubit frequency of $\delta\omega$ causes an arbitrary state to precess around the z-axis at a rate $\delta\omega$ in the rotating frame. Changing the frequency like this can be done by, for example, using a flux-tunable transmon, and is the basis for a Z gate.

Let us now return to our more complicated drive term of $V(t) = \frac{C_{xy}}{C_\Sigma}V_d(t)Q_{\text{zpf}}\sigma_y$. As we will now show, we can drive rotations around the x- and y-axes by driving the qubit with a coherent tone with amplitude V_d, frequency ω_d, and phase ϕ_d, allowing us to drive state transitions. Again in the interaction picture, the time-dependent part of

the Hamiltonian is

$$V_I = e^{i\mathcal{H}_0 t/\hbar} V(t) e^{-i\mathcal{H}_0 t/\hbar} \tag{1.89}$$

$$= e^{i\mathcal{H}_0 t/\hbar} \hbar\Omega_R \sin(\omega_d t + \phi_d)\sigma_y e^{-i\mathcal{H}_0 t/\hbar} \tag{1.90}$$

$$= \hbar\Omega_R \sin(\omega_d t + \phi_d) \begin{pmatrix} e^{i\omega_{01}t/2} & 0 \\ 0 & e^{-i\omega_{01}t/2} \end{pmatrix} \begin{pmatrix} 0 & -i \\ i & 0 \end{pmatrix} \begin{pmatrix} e^{-i\omega_{01}t/2} & 0 \\ 0 & e^{i\omega_{01}t/2} \end{pmatrix} \tag{1.91}$$

$$= \hbar\Omega_R \frac{e^{i(\omega_d+\phi_d)} - e^{-i(\omega_d+\phi_d)}}{2i} \begin{pmatrix} 0 & -ie^{i\omega_{01}t} \\ ie^{-i\omega_{01}t} & 0 \end{pmatrix} \tag{1.92}$$

$$= \frac{\hbar\Omega_R}{2} \begin{pmatrix} 0 & e^{i[\Delta\omega t+\phi_d]} - e^{i[(\omega_d+\omega_{01})t+\phi_d]} \\ e^{-i[\Delta\omega t+\phi_d]} - e^{-i[(\omega_d+\omega_{01})t+\phi_d]} & 0 \end{pmatrix}. \tag{1.93}$$

In the last step, we have defined $\Delta\omega \equiv \omega_d - \omega_{01}$. The terms $e^{-i[(\omega_d+\omega_{01})t+\phi_d]}$ can be thrown out according to the *rotating wave approximation* (RWA), which does so on the basis that they oscillate much faster than any time scale we are looking at and quickly average to zero. This can be understood by considering the time-dependent Schröinger equation. Integrating the terms of V_I, we get

$$\int e^{-i[(\omega_d\pm\omega_{01})t+\phi_d]} dt = \frac{e^{-i[(\omega_d\pm\omega_{01})t+\phi_d]}}{\omega_d \pm \omega_{01}}. \tag{1.94}$$

This approximation can be made when $(\omega_d - \omega_{01})/\omega_{01} \ll 1$. For the '+' terms, the numerator oscillates at a frequency in the tens of GHz, while being divided by that same tens of GHz. This averages out quickly. This frequency is generally in the several

MHz range for the '-' terms, which quickly dominate. If the drive is on resonance with the qubit frequency, $\Delta\omega = 0$, and taking the RWA, the interaction can be simplified to

$$V_I = \frac{\hbar\Omega_R}{2}\begin{pmatrix} 0 & e^{-i\phi_d} \\ e^{i\phi_d} & 0 \end{pmatrix} \tag{1.95}$$

$$= \frac{\hbar\Omega_R}{2}(\cos\phi_d\sigma_x + \sin\phi_d\sigma_y). \tag{1.96}$$

Note that this expression is time-independent, and that we can select between σ_x and σ_y by changing the phase ϕ_d.

1.5 Transmon readout

We now have a two level system that we can use as a qubit, and have a way to drive transitions between the states. The final piece in creating a useful qubit is a way to read out the qubit state. This is most commonly done with for transmons by coupling the qubit to a resonator and observing an induced frequency shift, an effect we will now show. Although practically the resonators used are usually (but not always) coplanar waveguides (CPWs) capacitively coupled to the qubit island, it is simple to map CPWs to a lumped LC mode [31], resulting in the circuit shown in Fig. 1.5.

As always, the first step to studying this system is to quantize the circuit. We can start by writing down the Lagrangian by inspection:

$$\mathcal{L} = \underbrace{\frac{1}{2}C_q\dot{\phi}_q^2 + E_J\cos\left(\frac{2\pi\phi_q}{\phi_0}\right)}_{\text{qubit}} + \underbrace{\frac{1}{2}C_r\dot{\phi}_r^2 - \frac{\phi_r^2}{2L_r}}_{\text{resonator}} + \underbrace{\frac{1}{2}C_g(\dot{\phi}_q - \dot{\phi}_r)^2}_{\text{coupling}}. \tag{1.97}$$

The first part of this Lagrangian, denoted 'qubit,' should be familiar. Finding the conjugate momentums,

$$p_{\{q,r\}} = \begin{pmatrix} \partial\mathcal{L}/\partial\dot{\phi}_q \\ \partial\mathcal{L}/\partial\dot{\phi}_r \end{pmatrix} \tag{1.98}$$

$$= \begin{pmatrix} C_q + C_g & -C_g \\ -C_g & C_r + C_g \end{pmatrix} \begin{pmatrix} \dot{\phi}_q \\ \dot{\phi}_r \end{pmatrix} \tag{1.99}$$

$$= C\dot{\phi} \equiv Q, \tag{1.100}$$

we again find them to be charges, either on the qubit island or on the capacitor of the resonator. The Hamiltonian for the circuit can be written down as

$$\mathcal{H} = \dot{\phi}^T Q - \mathcal{L} \tag{1.101}$$

$$= \frac{1}{2}\dot{\phi}^T Q + \frac{\phi_r^2}{2L_r} - E_J\cos\left(\frac{2\pi\phi_q}{\phi_0}\right). \tag{1.102}$$

The kinetic part of this Hamiltonian can be rewritten using Eq. 1.100 as

$$T = \frac{1}{2}\dot{\phi}^T Q \tag{1.103}$$

$$= \frac{1}{2} Q^T C^{-1} Q \tag{1.104}$$

$$= \frac{1}{2} \begin{pmatrix} q_q & q_r \end{pmatrix} \frac{1}{\det(C)} \begin{pmatrix} C_q + C_g & C_g \\ C_g & C_r + C_g \end{pmatrix} \begin{pmatrix} q_q \\ q_r \end{pmatrix} \tag{1.105}$$

$$= \frac{q_r^2}{2C_r'} + \frac{q_q^2}{2C_q'} + \frac{q_r q_q}{2C_g'}. \tag{1.106}$$

Here we have defined new capacitances

$$C_r' = C_r + \frac{C_q C_g}{C_q + C_g} \tag{1.107}$$

$$C_q' = C_q + \frac{C_r C_g}{C_r + C_g} \tag{1.108}$$

$$C_g' = \frac{(C_r + C_g)(C_q + C_g) - C_g^2}{C_g}, \tag{1.109}$$

such that the C_r' and C_q' represent the capacitance to ground from each respective node, and C_g' is calculated for consistent notation. This leaves us with the Hamiltonian

$$\mathcal{H} = \underbrace{\frac{q_r^2}{2C_r'} + \frac{\phi_r^2}{2L_r}}_{\mathcal{H}_\mathrm{r}} + \underbrace{\frac{q_q^2}{2C_q'} - E_J \cos\left(\frac{2\pi\phi_q}{\phi_0}\right)}_{\mathcal{H}_\mathrm{q}} + \underbrace{\frac{q_r q_q}{2C_g'}}_{\mathcal{H}_\mathrm{g}}. \tag{1.110}$$

We are already familiar with the Hamiltonian H_q for the qubit, and we know the resonator Hamiltonian H_r to be that of a quantum harmonic oscillator. Under the

second quantization and the RWA with the qubit asserted to be a two-level system, we can define raising and lower operators for the qubit and the resonator:

$$q_r = -i\sqrt{\frac{\hbar\omega_r C_r'}{2}}(a_r - a_r^\dagger) \tag{1.111}$$

$$q_q = -i\sqrt{\frac{\hbar\omega_{01} C_q'}{2}}(\sigma_- - \sigma_+). \tag{1.112}$$

The Hamiltonians then become

$$\mathcal{H}_r = \hbar\omega_r \left(a_r^\dagger a_r + \frac{1}{2}\right) \tag{1.113}$$

$$\mathcal{H}_q = \frac{1}{2}\hbar\omega_{01}\sigma_z \tag{1.114}$$

$$\mathcal{H}_g = \hbar g(a_r - a_r^\dagger)(\sigma_- - \sigma_+). \tag{1.115}$$

Here g is the angular coupling strength between the resonator and qubit, given by

$$g \equiv \frac{1}{2}\frac{C_g}{(C_q + C_g)(C_r + C_g)}\sqrt{\omega_r\omega_{01}}. \tag{1.116}$$

Let's take a closer look at the coupling Hamiltonian H_g. Expanding this Hamiltonian,

$$\mathcal{H}_g = \hbar g(\cancel{a_r\sigma_-} - a_r\sigma_+ - a_r^\dagger\sigma_- + \cancel{a_r^\dagger\sigma_+}), \tag{1.117}$$

we see that two of these terms induce a swap of an excitation at an angular frequency of g, using a photon in the resonator to drive a transition from $|0\rangle_q \rightarrow |1\rangle_q$ or vice versa. The other two terms, which have been crossed out above, do not conserve excitation number.

The canceling of these terms can also be seen through the lens of the rotating wave approximation. Defining $\mathcal{H}_0 = \mathcal{H}_r + \mathcal{H}_q$ and the time evolution operator $U = e^{-i\mathcal{H}_0 t/\hbar}$, and using the Baker-Campbell-Hausdorf formula, we find the following relations:

$$U^\dagger a U = a e^{-i\omega_r t} \tag{1.118}$$

$$U^\dagger a^\dagger U = a e^{+i\omega_r t} \tag{1.119}$$

$$U^\dagger \sigma_- U = \sigma_- e^{-i\omega_{01} t} \tag{1.120}$$

$$U^\dagger \sigma_+ U = \sigma_+ e^{+i\omega_{01} t}. \tag{1.121}$$

Disguarding constant terms, the coupling Hamiltonian in the interaction picture can then be written as

$$\mathcal{H}_{I,g} = \hbar g \left(\cancel{a_r \sigma_- e^{-i(\omega_r + \omega_{01})t}} - a_r \sigma_+ e^{-i(\omega_r - \omega_{01})t} - a_r^\dagger \sigma_- e^{i(\omega_r - \omega_{01})t} + \cancel{a_r^\dagger \sigma_+ e^{i(\omega_r + \omega_{01})t}} \right), \tag{1.122}$$

where this time terms have been crossed out due to the RWA. Returning to the Schröinger picture, we arrive at the so-called *Jaynes-Cummings Hamiltonian*:

$$\frac{\mathcal{H}_{JC}}{\hbar} = \omega_r a_r^\dagger a_r + \frac{\omega_{01}}{2}\sigma_z - g\left(a_r \sigma_+ + a_r^\dagger \sigma_-\right). \tag{1.123}$$

As described before, the coupling term exchanges excitations between the cavity and the qubit. If we rewrite our $|0\rangle_q$ and $|1\rangle_q$ qubit states as ground $|g\rangle$ and excited $|e\rangle$, the Hamiltonian is a block-diagonal matrix:

$$\frac{\mathcal{H}_{JC}}{\hbar} = \begin{matrix} \\ \langle n,e| \\ \langle n+1,g| \end{matrix} \begin{matrix} |n,e\rangle & |n+1,g\rangle \\ \end{matrix} \begin{pmatrix} n\omega_r + \frac{1}{2}\omega_{01} & \sqrt{n+1}g \\ \sqrt{n+1}g & (n+1)\omega_r - \frac{1}{2}\omega_{01} \end{pmatrix}. \tag{1.124}$$

The eigen-energies for this Hamiltonian are[1]

$$E_{n,\pm} = \left(n + \frac{1}{2}\right)\hbar\omega_r \pm \hbar\frac{|\Delta|}{2}\sqrt{1 + 4(n+1)\left(\frac{g}{\Delta}\right)^2}, \tag{1.125}$$

with corresponding eigenstates

$$|n,+\rangle = \cos\theta_n|n,e\rangle + \sin\theta_n|n+1,g\rangle \tag{1.126}$$

$$|n,-\rangle = -\sin\theta_n|n,e\rangle + \cos\theta_n|n+1,g\rangle. \tag{1.127}$$

Here we define detuning $\Delta = \omega_{01} - \omega_r$, and θ_n is given by $\tan 2\theta_n = 2g\sqrt{n+1}/\Delta$. Under the binomial approximation, this can be expanded in the $g/\Delta \ll 1$ limit to

$$E_{n,\pm} \approx \left(n + \frac{1}{2}\right)\hbar\omega_r \pm \hbar\frac{|\Delta|}{2}\left[1 + 2(n+1)\left(\frac{g}{\Delta}\right)^2\right] \tag{1.128}$$

$$= \begin{cases} (\omega_r + \chi)n + \omega_{01}/2 + \chi & \leftarrow |n,e\rangle \\ (\omega_r - \chi)(n+1) - \omega_{01}/2 & \leftarrow |n+1,g\rangle \end{cases}, \tag{1.129}$$

where in the second step we have defined the *dispersive shift* $\chi \equiv g^2/\Delta$. The two braced terms do not correspond to the + or -, but rather to which state the energy corresponds to in the appropriate limit, which can be found by calculating θ_n. This is

[1] It is easier to solve for the eigenvalues if we first subtract $\mathbb{1} \times \left(n + \frac{1}{2}\right)\omega_r$.

shown and labeled in Fig. 1.5c.

With n photons in the resonator, we see that the frequency of the resonator is altered to

$$\omega_r \rightarrow \begin{cases} \omega_r - \chi & |g\rangle \\ \\ \omega_r + \chi & |e\rangle \end{cases}. \tag{1.130}$$

Similarely, the qubit frequency is altered by the number of photons in the resonator:

$$\omega_{01} \rightarrow \omega_{01} + \chi(2n+1). \tag{1.131}$$

Note that this approximation breaks down once $4(n+1)\left(\frac{g}{\Delta}\right)^2$ is no longer a small parameter, leading to the definition

$$n_{\text{crit}} \equiv \frac{1}{4}\left(\frac{\Delta}{g}\right)^2. \tag{1.132}$$

The disperisve approximation breaks down when more than n_{crit} photons occupy the resonator.

The effect of the cavity-qubit coupling can be seen more clearly by perturbing the

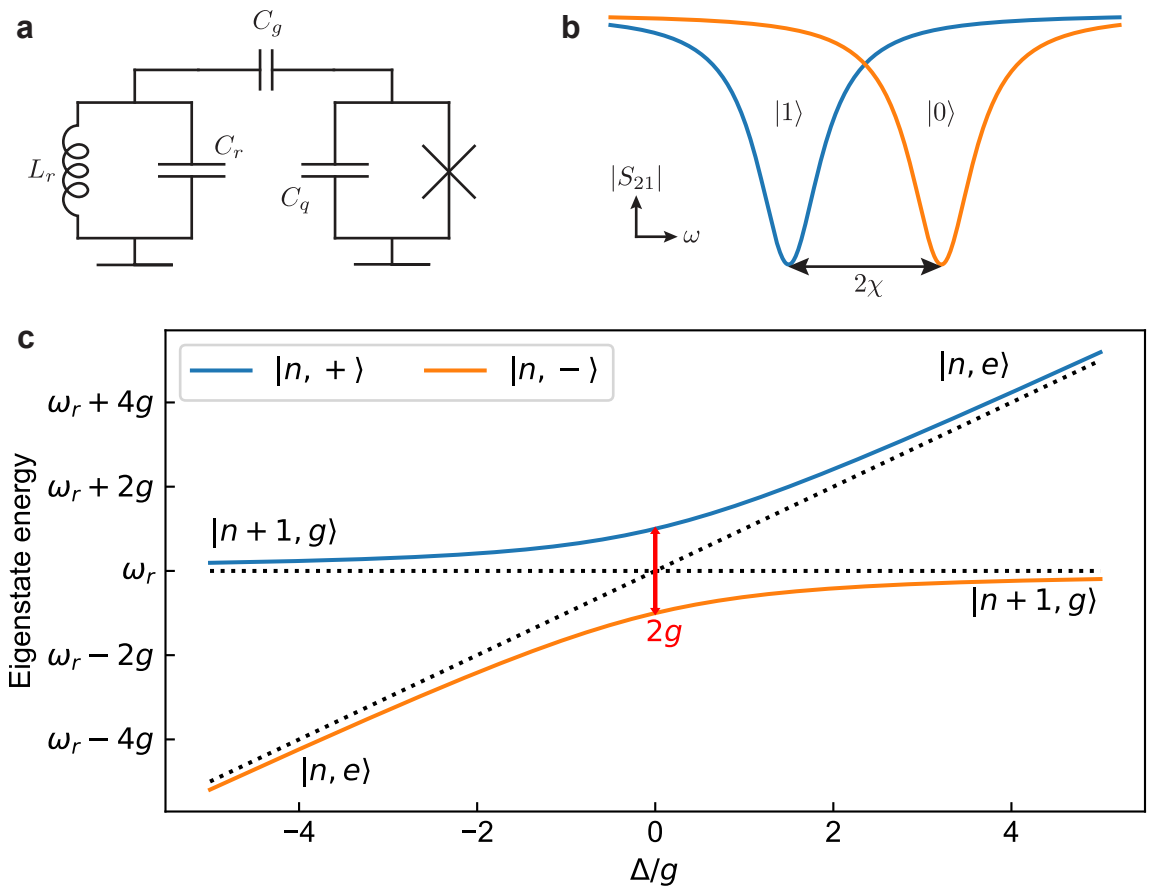

Figure 1.5: **Transmon coupled to readout resonator.** (**a**) Circuit diagram of a transmon qubit capacitively coupled to a (lumped-element) readout resonator. (**b**) Depending on the state of the qubit, the frequency of the readout resonator shifts by $\pm\chi$. (**c**) An avoided level crossing is seen when the qubit frequency gets close to that of the coupled resonator. As the frequencies get closer, the states hybridize.

Hamiltonian $\mathcal{H}_0 = \mathcal{H}_r + \mathcal{H}_q$ to second order in the interaction $V = \mathcal{H}_g$:

$$E^{(0)}_{g,n} = \langle g, n|\mathcal{H}_0|g, n\rangle = \omega_r n - \frac{\Delta}{2} \tag{1.133}$$

$$E^{(0)}_{e,n} = \langle e, n|\mathcal{H}_0|e, n\rangle = \omega_r (n+1) + \frac{\Delta}{2} \tag{1.134}$$

$$E_{g,n} = E^{(0)}_{g,n} + \cancelto{0}{\langle g, n|V|g, n\rangle} + \frac{|\langle e, n-1|\mathcal{H}_0|g, n\rangle|^2}{E^{(0)}_{g,n} - E^{(0)}_{e,n-1}} \tag{1.135}$$

$$= \omega_r n - \frac{\Delta}{2} + \frac{g^2 n}{-\Delta} \qquad \left[-\frac{1}{2}\frac{g^2}{\Delta}\right] \tag{1.136}$$

$$= \omega_r n - \frac{\Delta}{2} - \frac{g^2}{\Delta}\left(n + \frac{1}{2}\right) \tag{1.137}$$

$$E_{e,n} = E^{(0)}_{e,n} + \cancelto{0}{\langle e, n|V|e, n\rangle} + \frac{|\langle g, n+1|\mathcal{H}_0|e, n\rangle|^2}{E^{(0)}_{e,n} - E^{(0)}_{g,n+1}} \tag{1.138}$$

$$= \omega_r (n+1) + \frac{\Delta}{2} + \frac{g^2 (n+1)}{-\Delta} \qquad \left[-\frac{1}{2}\frac{g^2}{\Delta}\right] \tag{1.139}$$

$$= \omega_r (n+1) + \frac{\Delta}{2} + \frac{g^2}{\Delta}\left(n + \frac{1}{2}\right) \tag{1.140}$$

$$\widetilde{|g, n\rangle} = |g, n\rangle - \frac{g\sqrt{n}}{\Delta}|e, n-1\rangle \tag{1.141}$$

$$\widetilde{|e, n\rangle} = |e, n\rangle - \frac{g\sqrt{n+1}}{\Delta}|g, n+1\rangle \tag{1.142}$$

Under this perturbation, we see that after subtracting a constant from the energy, the coupling Hamiltonian can be simplified to $\mathcal{H}_g = -\frac{\hbar}{2}\chi\sigma_z(2n+1)$, bringing the full

Hamiltonian to

$$\frac{\mathcal{H}}{\hbar} = \omega_r n - \frac{\omega_{01}}{2}\sigma_z - \frac{\chi}{2}\sigma_z(2n+1) \tag{1.143}$$

$$= \omega_r n - \frac{\sigma_z}{2}\left(\omega_{01} + 2\chi\left(n + \frac{1}{2}\right)\right) \tag{1.144}$$

$$= (\omega_r - \chi\sigma_z)n - \frac{\sigma_z}{2}(\omega_{01} + \chi). \tag{1.145}$$

Here we have rewritten the Hamiltonian in two ways to highlight different effects. In Eq. 1.144, it is evident that the the qubit frequency is shifted by $2n\chi$, known as the *ac Stark effect*. This shift, dependent on the number of photons in the cavity, is the origin of *photon shot-noise dephasing*, where changes in the photon number induce changes in the qubit frequency and therefore cause precession around the bloch sphere in the rotating frame. There is an extra shift of χ that is not number dependent, known as the *Lamb shift*.

Alternatively, we can rewrite the Hamiltonian as in Eq. 1.145. In this form, we see that the frequency of the resonator shifts by $\pm\chi$ depending on the qubit state, an effect known as the *dispersive shift*. This allows us to read out the state of the qubit by looking at the frequency of the resonator.

These same results can be recovered through the Schrieffer–Wolff transformation or by directly diagonalizing Eq. 1.124 in the dispersive limit $g/\Delta \ll 1$. Including a third qubit state and bringing back anharmonicity α, the dispersive shift is modified to [28]

$$\chi = \frac{g^2}{\Delta} \rightarrow \frac{g^2}{\Delta}\left(\frac{\alpha}{\Delta+\alpha}\right), \tag{1.146}$$

where α is the qubit anharmonicity. Without this modification, the resonator frequency would always be shifted away from an excited qubit. With this correction, however, and under the assumption that $\Delta \gg \alpha$, we have $\chi \approx (g^2/\Delta^2)\alpha$, indicating that resonator frequency will always be lower for an excited qubit than a qubit in the ground state.

1.6 Heterodyne readout

To measure the state of the qubit via changes in frequency of the readout resonator, one generally drives the readout resonator with a tone near its resonance in a heterodyne setup. The reflection coefficients of our qubit and readout circuit change with frequency and with qubit state, as detailed in chapter 3 of Daniel Sank's thesis [32]. An incoming coherent tone will induce an outgoing coherent tone with an altered magnitude and phase that depend on the qubit state.

To generate a coherent tone in the 4-8 GHz frequency range normally used for readout resonators, we utilize an IQ mixer to mix a high frequency tone from a function generator with a lower frequency tone (in the hundreds of MHz range) output from a digital to analog converter (DAC). This allows pulses to be shaped and quickly turned on and off without the cost and complexity of a high frequency arbitrary waveform

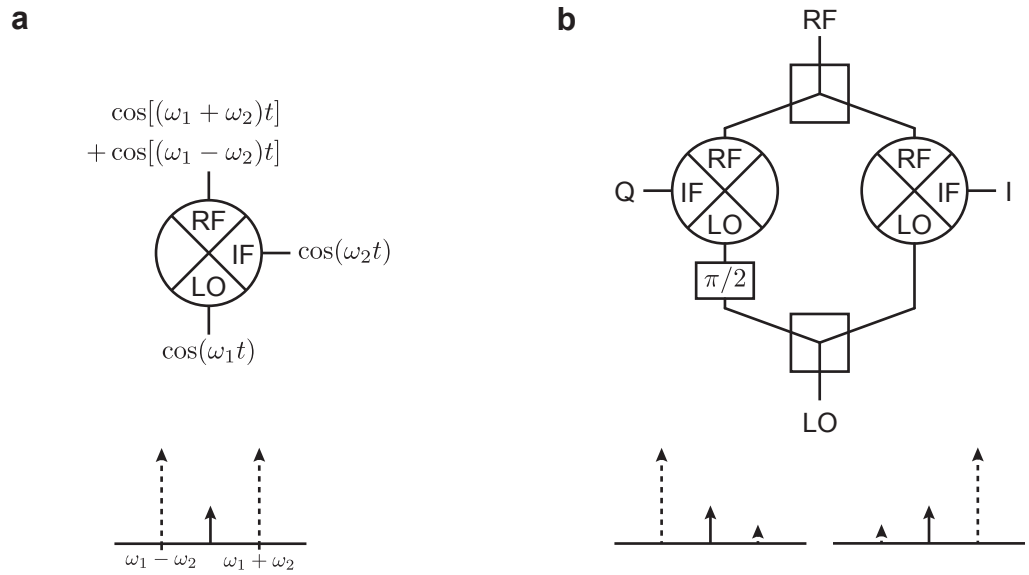

Figure 1.6: **(IQ) mixers.** (**a**) A mixer combines two tones (LO and IF) into a tone (RF) with Fourier components at the sum and difference frequencies. The cartoon below the diagram of the mixer shows the sidebands in frequency space, with a small amount of bleedthrough at the LO frequency in the middle. (**b**) An IQ mixer combines two mixers to remove one of the sidebands. Which one is negated depends on the phase of the input signals. Without perfect calibration, there will be a small amount of bleedthrough at the suppressed sideband as well.

generator (AWG).

A mixer uses the nonlinearity of diodes to multiply two input signals. Given inputs of two harmonic tones at angular frequencies ω_{LO} and ω_{IF}, and with phases $\phi_{LO} = 0$ and ϕ_{IF}, the output of the mixer will be

$$\cos(\omega_{LO}t)\cos(\omega_{IF}t+\phi_{IF}) = \frac{1}{2}\{\cos[(\omega_{LO}-\omega_{IF})t-\phi_{IF}]+ \cos[(\omega_{LO}+\omega_{IF})t+\phi_{IF}]\}. \quad (1.147)$$

The two input tones are the local oscillator (LO), which comes from the function generator, and the intermediate frequency (IF), which is generated by the DAC. The output at the RF port of the mixer is the convolution of two tones, with frequency components at the sum of the inputs, $\omega_{LO}+\omega_{IF}$, as well as at the difference, $\omega_{LO}-\omega_{IF}$. These are known as "sidebands." Already this is beneficial, as we can put the readout resonance at one of the sideband frequencies and quickly turn on or off the drive by changing the IF frequency with the DAC, or even turning it off by setting the frequency to 0. Any leakage of the LO tone will be at a frequency that does not overlap with the cavity.

The extra sideband, however, can cause problems if it overlaps with other modes (of other readout resonators, qubits, etc.). It can be even better to operate with a single sideband using an *IQ mixer*. An IQ mixer combines two mixers, each with the same LO, but one with a $\pi/2$ phase shifter, as shown in Fig. 1.6b. Adding the signals from each mixer together, we get:

$$\cos(\omega_{LO}t)\cos(\omega_I t+\phi_I)+\cos(\omega_{LO}t+\pi/2)\cos(\omega_Q t+\phi_Q) \tag{1.148}$$

$$=\frac{1}{2}\{\cos[(\omega_{LO}-\omega_I)t-\phi_I]+\cos[(\omega_{LO}+\omega_I)t+\phi_I]+$$

$$\cos[(\omega_{LO}-\omega_Q)t-\phi_Q+\pi/2]+\cos[(\omega_{LO}+\omega_Q)t+\phi_Q+\pi/2]\}. \tag{1.149}$$

If we assert $\omega_I=\omega_Q=\omega$ and set $\phi_Q=\phi_I\pm\pi/2$, two of the terms will cancel, leaving us with a single sideband at angular frequency $\omega_{LO}\mp\omega$ and phase $\phi=\mp\phi_I$. Practically,

the two mixers are never perfectly balanced, and there will be small amounts of leakage at both the LO frequency and the suppressed sideband.

The labels (I)n-phase and (Q)uadrature derive from the Q input tone having a phase offset of $\pm\pi/2$ from the I tone. If we multiply $Q(t)$ by i, we can represent both signals with a single time-dependent complex number $z_{IQ}(t)$ that traces a circle in the complex plane at angular frequency ω and phase ϕ:

$$z_{IQ}(t) = e^{i(\pm\omega t+\phi)}. \tag{1.150}$$

An IQ mixer is also used to demodulate a high frequency signal into its in-phase and quadrature components for readout by an analog to digital converter (ADC). Consider a signal returning from the fridge with amplitude A, frequency $\omega_{LO} \mp \omega$, and phase δ. After returning to the RF port of the mixer, and with the same applied LO tone, the I and Q ports output:

$$\begin{aligned} I(t) &= A\cos[(\omega_{LO} \mp \omega)t + \delta]\cos[\omega_{LO}t] \\ &= \frac{A}{2}\{\cos[\mp\omega t + \delta] + \cancel{\cos[(2\omega_{LO} \mp \omega)t + \delta]}\} \end{aligned} \tag{1.151}$$

$$\begin{aligned} Q(t) &= A\cos[(\omega_{LO} \mp \omega)t + \delta]\cos[\omega_{LO}t + \pi/2] \\ &= \frac{A}{2}\{\cos[\mp\omega t + \delta - \pi/2] + \cancel{\cos[(2\omega_{LO} \mp \omega)t + \delta + \pi/2]}\}. \end{aligned} \tag{1.152}$$

Here the canceled terms are high frequency and average out quickly (or can be filtered).

With $I(t)$ and $Q(t)$ again representing the real and imaginary parts of a point on the complex plane, we can rewrite this as

$$z_{RF}(t) = \frac{A}{2} e^{i(\mp\omega t + \delta)}. \tag{1.153}$$

The final step to demodulation is multiplying by $e^{\mp i\omega t}$ and taking the time average, leaving us with

$$\bar{z}_{RF}(t) = \frac{A}{2} e^{i\delta}. \tag{1.154}$$

This analysis has used the local oscillator phase as a reference, and has ignored several constant factors, such as loss in the lines, the amplitude of the of the local oscillator, and the splitters and combiners within the mixer or on the LO line, but in the end we are projecting the final point $\bar{z}$ onto a state label. Taking many single shot measurements leaves us with clusters of points in IQ space, and although these constant factors can effect the SNR of a measurement, the state differentiation process does not depend on them. It is important to be able to accurately separate and identify clusters of IQ points in order to project measurements to the correct state, but there are many ways to do this and these are beyond the scope of this thesis.

1.7 Optimal readout

The higher the Q of the readout resonator, or the more separated (higher χ) the dispersively shifted resonances, the less overlap there will be between the IQ clusters

for the $|0\rangle$ and $|1\rangle$ states. However, a higher-Q resonator also releases information more slowly and results in the need for longer integration times during readout. As it turns out, for a given χ shift, there is an optimal resonator Q that gives the highest fidelity readout in the shortest time.

Consider two resonances separated by 2χ from each other. We are able to project all the effects of the qubit measurement onto this classical problem of differentiating these resonances, since in the dispersive limit, the interaction Hamiltonian goes like σ_z and commutes with the qubit Hamiltonian. For a hanging resonator, the scattering parameters, which are effectively measured by the heterodyne setup described above, go like

$$S_{21} = \frac{S_{\min} - 2iQ_L\delta y}{1 + 2iQ_L\delta y} \tag{1.155}$$

$$= \frac{S_{\min} + (2Q_L\delta y)^2}{1 + (2Q_L\delta y)^2} + i\frac{(2Q_L\delta y)(1 - S_{\min})}{1 + (2Q_L\delta y)^2}, \tag{1.156}$$

where $S_{\min} = Q_c/(Q_i + Q_c)$, the resonator is loaded such that $Q_L^{-1} = Q_i^{-1} + Q_c^{-1}$, $\delta y = (\omega - \omega_r)/\omega_r$, Q_i and Q_c are the internal and coupling quality factors, and ω_r is the resonance frequency. In the second line, we have simply separated the real and imaginary parts. Plotting S_{21} in the complex plane as a function of δy (normalized frequency) gives a circle with the closest point from the origin at $(S_{\min}, 0)$.

For cleanest readout, we want the measured S_{21} of the two resonators to be maximally separated at our readout frequency, i.e. we want to maximize $d = S_{21}^{\mathrm{A}} - S_{21}^{\mathrm{B}}$ for

resonators A and B. If we measure between the resonances, the resonators are detuned from the measurement frequency by $\pm\chi$, or $\delta y = \pm\chi/\omega_r$. The real part of d is an even function and will cancel, while the imaginary part constructively adds together. Equating the derivative with zero, we find the extrema of the imaginary part to be at $\delta y = \pm 1/2Q_L$, showing that for maximum separation and optimal readout,

$$\chi = \frac{\omega_r}{2Q_L} = \frac{\kappa_r}{2}, \tag{1.157}$$

where κ_r is the 1/e decay time of the readout resonator. On the circle representing the resonance in the complex plane, the two extrema are on opposite sides and as far apart as possible on the circle, confirming our choice of readout frequency.

Chapter 2

Decoherence and errors

2.1 Noisy qubits

Ideally, a qubit would stay in a state to which it is initialized for eternity. Unfortunately, the need for control of the qubit introduces channels for qubits to interact with their surrounding, making them susceptible to inadvertent rotations on the Bloch sphere caused by noise [33]. Many of these decoherence mechanisms are already well studied in transmon qubits, and will be briefly summarized here. First, however, it is useful to go over the types of errors that can be caused by noise.

The first type of error is an excitation or relaxation, where the state vector rotates such that the value after projecting along the z-axis is changed. This is sometimes referred to as "depolarization," and requires an exchange of energy between the qubit and its environment. Such an energy exchange requires the interaction to be a x- or

y-rotation at the qubit frequency, with the relaxation rate and corresponding T_1 time defined as

$$\Gamma_1 \equiv \frac{1}{T_1} = \Gamma_\downarrow + \Gamma_\uparrow. \tag{2.1}$$

Here $\Gamma_\downarrow$ and $\Gamma_\uparrow$ are the up and down transition rates, respectively. Practically, Γ_1 is usually dominated by $\Gamma_\downarrow$ in a dilution refrigerator at 20 mK, but this is not necessarily always true.

The second type of error is qubit dephasing, in which the state vector rotates around the Bloch sphere, affecting future operations on the qubit. Experimentally it is hard to measure the pure dephasing rate Γ_ϕ, so instead we measure T_1 and the transverse relaxation rate Γ_2:

$$\Gamma_2 \equiv \frac{1}{T_2} = \Gamma_1/2 + \Gamma_\phi. \tag{2.2}$$

Dephasing can couple at any frequency and is a z-rotation, usually caused by a change in the qubit frequency such that it no longer matches the frequency of the rotating frame. Unlike relaxation or excitation, there is no energy exchanged with the environment, and many dephasing errors can be undone with more complex qubit control sequences.

It is common to measure the power spectral density (PSD) of a noise source λ, defined as the Fourier transform of the autocorrelation function:

$$S_\lambda(\omega) = \int_{-\infty}^{\infty} \langle \lambda(\tau)\lambda(0)\rangle e^{-i\omega t} d\tau. \tag{2.3}$$

This measurement can be tied directly to both dephasing errors through a σ_z interaction or excitation/relaxation errors through a σ_x interaction, and so provides a good way to characterize noise.

If we consider a small perturbation of type σ_x to the qubit Hamiltonian $\mathcal{H}_q$, we can use first-order time-dependent perturbation theory (or Fermi's Golden Rule) to find the up and down transition rates:

$$\Gamma_{\uparrow\downarrow} = \frac{1}{\hbar^2}|\langle 0|\frac{\partial \mathcal{H}_q}{\partial \lambda}|1\rangle|^2 S_\lambda(\pm\omega_{01}). \tag{2.4}$$

Similarly, we can calculate dephasing due to a σ_z-type noise source:

$$\delta\phi(t) = \frac{\partial\omega_{01}}{\partial\lambda}\int_0^t \delta\lambda(t')dt' \tag{2.5}$$

$$= \frac{1}{\hbar}\left|\frac{\partial \mathcal{H}_q}{\partial\lambda}\right|\int_0^t \delta\lambda(t')dt'. \tag{2.6}$$

A large number of fluctuators coupled to the qubit give a coherence decay function with a Gaussian ensemble average

$$\langle e^{i\delta\phi(t)}\rangle = \exp\left[-\frac{t^2}{2}\frac{\partial\omega_{01}}{\partial\lambda}\int_{-\infty}^{\infty} g_N(\omega,t)S(\omega)d\omega\right]. \tag{2.7}$$

This function is often non-exponential and hard to write in terms of a pure dephasing time, which would take the form e^{-t/T_2}. This is in large part because of the filter function $g_N(\omega,t)$. Filters at various frequencies can be constructed with a series of π gates, allowing the dephasing from an ensemble of fluctuators to be undone. When

using "echo pulses" to filter out low frequency noise, only white noise ends up being important.

Before moving on to describing some of the main noise mechanisms that cause qubit decoherence, it is worth quickly describing some common types of noise spectra. *White noise* has a flat spectrum, with every frequency containing the same noise power. Integrating white noise gives Brownian motion, and results in a $1/f^2$ spectrum. This can easily be seen by considering two time series X_W and X_B governed by white and brown noise, respectively, and relating their power spectra: [34]

$$S_W = |\mathcal{F}(X_W(t))|^2 = |\mathcal{F}\left(\frac{d}{dt}X_B(t)\right)|^2 = \omega^2 S_B(\omega). \tag{2.8}$$

Here $\mathcal{F}()$ represents the Fourier transform, and we see that with a constant spectra S_W, we get $S_B(\omega) = S_W/\omega^2$. In the experiments that follow in later chapters, the Brownian motion comes from liberated charge flowing through the substrate, leading to a $1/f^2$ charge noise spectrum.

It is also common to see a noise spectrum that follows a "$1/f$" distribution that takes the form

$$S_\phi(f) = A^2 \left(\frac{1\text{ Hz}}{f}\right)^\alpha. \tag{2.9}$$

This is known to arise from an ensemble of damped fluctuators evenly distributed between two frequencies f_1 and f_2. Between these two frequencies, $\alpha = 1$. Below f_1, the spectrum will exhibit white noise, and above f_2, the spectrum will be $1/f^2$. Changing the distribution of fluctuators can change α to be higher, in the range 1-2.

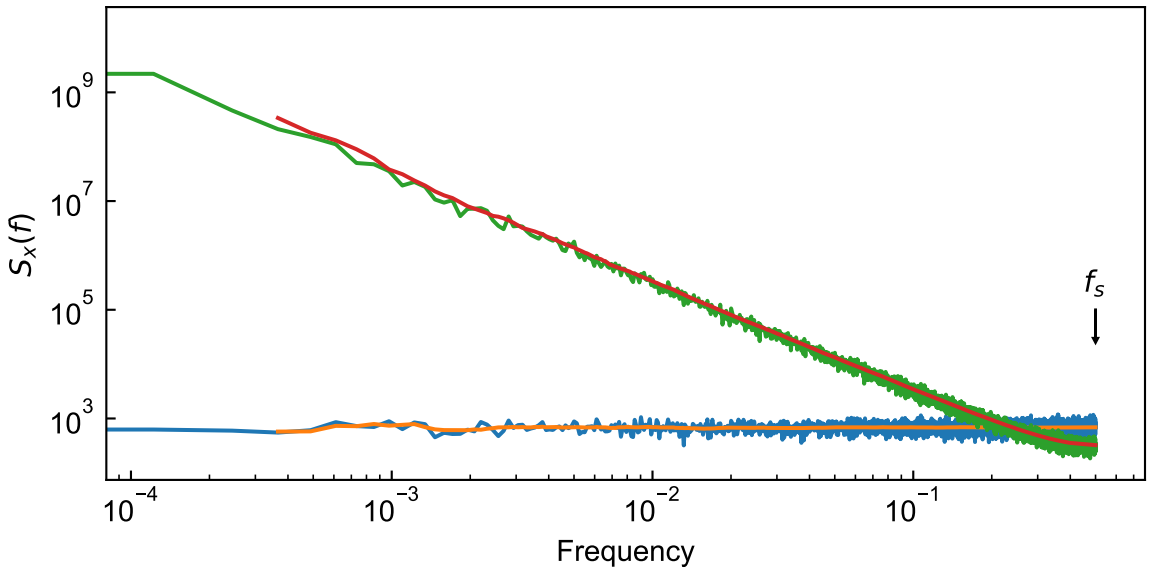

Figure 2.1: **White and brown noise.** Shown here are the power spectra of simulated noise. In blue, we have the PSD for simulated white noise. Cumulatively summing the white noise gives brown noise, with a power spectrum shown in green. The orange and red curves are windowed averages of the white and brown spectra.

In the single-fluctuator limit ($f_1 = f_2$), we are left with a Lorentzian power spectrum.

Lastly, digitization in an experiment can lead to noise. With each measurement, a (usually continuous) value will be projected onto a number with some finite resolution. Assuming the process being measured does not line up with the measurement resolution in an odd way, the experimental variable will be rounded up or down with equal probability on average, giving the measurement a white-noise floor.

2.1.1 Magnetic flux noise

Replacing the junction in a transmon with a SQUID allows for tuning of the qubit frequency with an applied magnetic field. In large systems with lots of overlapping

frequencies, this is probably necessary, and is the foundation of some coupling schemes between qubits. Adding this variability, however, introduces a channel for dephasing, in which variations of the magnetic field change the qubit frequency and noise is introduced. The exact microscopic source of these variations in magnetic fields is still unknown, but it is suspected to be oxygen molecules adsorbed onto the surface of the device during cooldown [35]. The PSD of flux noise generally follows a $1/f$ distribution with $A = 1\ \mu\Phi_0/\sqrt{\text{Hz}}$ and $\alpha = 0.8 - 1$. Although most of the spectral content induces dephasing, noise at the qubit frequency can also cause qubit transitions. Magnetic flux noise can limit the performance of flux-tunable transmons, but operating them at the "upper sweet spot" makes them insensitive to flux noise to first order. Surface treatments may be effective at mitigating some flux noise.

2.1.2 Dielectric defects

Qubits are susceptible to loss whenever their electric fields penetrate a dielectric. The current understanding is that two level systems (TLS) within the dielectrics can change state, absorbing energy from the fields. The exact microscopic origin of TLS is not known, but they are expected to be bonds that tunnel between two sites, and can give rise to a number of important phenomena. Although qubits are generally fabricated on dielectric substrates, high purity crystalline silicon has a low enough *loss tangent* – a measure of a material's inherent dissipation, defined with the relative permitivity ϵ_r

as $\tan\delta = \mathrm{Re}(\epsilon_r)/\mathrm{Im}(\epsilon_r)$ – to not be a large concern for superconducting qubits [36].

Of more concern are dielectric oxides that form on the surfaces and interfaces of devices. TLS defects within the oxide of the Josephson junctions that make up a qubit are particularely harmful, as they are coupled strongly enough that they can coherently exchange excitations with the qubit. The density of TLS are low enough, however, that this can be easily avoided by moving to smaller junction sizes below 1-10 $\mu\mathrm{m}^2$, in which a TLS is unlikely to occur [37].

Lossy oxides also form at a variety of interfaces around the qubit structure. These oxides are often characterized by the *participation ratio*, or the portion of the electric field that penetrates the material of concern. Large advances in coherence time were achieved by designing qubits with large planar capacitor pads that spread out the field and minimized the participation ratios with lossy materials, ideally concentrating the fields in lossless vacuum [38]. In general, the larger the device footprint, the lower the participation ratios will be. 3D devices have an inherent advantage in this area since they concentrate fields in vacuum instead of a substrate [39, 40]. Inevitably, defects in interface oxides will still couple to the qubit at some level, especially when closely matched in frequency with the qubit, causing T1 "dropouts" at certain frequencies. This remains a huge problem in state-of-the-art quantum computing, limiting the frequency space in which qubits can be operated [41]. Recent studies [42, 43] show most TLS defects reside on the surface of the device – either on the surface of the supercon-

ducting metal or on the substrate, within 50 nm of the boundary – or in the oxides of parasitic junctions that form from double-angle evaporation.

A signature of TLS-induced relaxation in qubits is the temperature and/or power dependence. At low temperatures and powers, power is lost to resonant defects, decreasing the quality factor of resonators and qubits. As the temperature or power increases, however, more TLS get saturated and the Q factor goes up. Eventually, quasiparticles overwhelm this effect and cause Q to drop again.

Careful attention must be applied to the deposition of metals on substrates to minimize lossy TLS's. Dipping the wafer in hydrofluoric acid prior to deposition can clean up oxides in the substrate-metal interface and improve coherence times, but removing the oxide with an ion mill roughs up the surface and decreases coherence [44]. One solution is to use the "bandaid process" [45] to avoid ion milling the area under the junction, which always has a high participation ratio and can be a concentrated source of loss. This can also help prevent the burning on of lossy ebeam resist residue by ion milling.

2.1.3 Photon number fluctuations

We were introduced to the Stark effect in Eq. 1.144, where we saw that the qubit frequency is shifted by $2n\chi$, where n is the number of photons in the readout resonator. Any fluctuations in n result in a change in the qubit frequency and a precession in

the rotating frame. In dispersive readout, this shift is modified by a scaling factor $\eta = \kappa^2/(\kappa^2 + 4\chi^2)$, where κ is the cavity decay rate. These changes can come from active ringup or ringdown of the readout cavity, excitation of cavity modes from IR radiation, or zero-point fluctuations, and are thought to limit dephasing times [46, 47]. An average of $\bar{n}$ photons in the readout cavity leads to a dephasing rate

$$\Gamma_\phi = \eta \frac{4\chi^2}{\kappa} \bar{n}, \tag{2.10}$$

with a Lorentzian spectral density

$$S(\omega) = 4\chi^2 \frac{2\eta\bar{n}\kappa}{\omega^2 + \kappa^2}. \tag{2.11}$$

The easiest way to limit this so-called "shot noise dephasing" is by increasing the rate at which photons leave the readout resonator. This can be done through active reset or through a resonator with a lower quality factor, often in conjunction with a Purcell filter as described below.

2.1.4 Charge noise

Charge noise refers to any effects of changing electric fields near the qubit. Changing an external electric field on the qubit island changes n_g, which can vary the qubit frequency and introduce dephasing. Transmons are exponentially insensitive to this effect, but higher level transitions are more sensitive, and other types of devices including topologically protected qubits can be much more susceptible to charge noise. Additionally, rapid changes in offset charge can induce state transitions [48]. Char-

acterizing this noise is one of the main focuses of this thesis, so we will discuss this in detail in future chapters. In the meantime, suffice it to say we found charge noise follows a $1/f$ distribution with $A^2 = 2.9 \times 10^{-4}\ e^2/\text{Hz}$ and $\alpha = 1.93$.

2.1.5 Radiative losses and the Purcell effect

Any of the on-chip microwave components that hold an RF electromagnetic field can radiate energy away, causing decoherence. The coplanar waveguide resonators usually used for readout have a highly contained field, and very little is radiated. They can, however, enhance the radiative coupling of a qubit to an external bath through the so-called *Purcell effect*. Because of the slight mixing of states (Eqs. 1.141-1.142) of the readout resonator modes and the qubit state, any dissipative modes coupled to the resonator will also couple to the qubit. Inserting the mixed states into Fermi's golden rule yields a Purcell limited T1 of [28]

$$T_1 = \frac{1}{\kappa}\left(\frac{\Delta}{g}\right)^2. \tag{2.12}$$

A close approximation to this can also be found by finding the decay time of a dissipationless LC oscillator (the qubit) when coupled to a second oscillator that has a some resistance (the readout resonator and external bath).

Making higher-Q readout resonators would help decouple the qubit from these loss channels, and lead to a longer relaxation time. However, the readout resonator needs to be reset (relax to ground state) between qubit operations to avoid Stark shifts and

partial measurements during operation. It would also be harder to read out the qubit state. The most common solution is to use a *Purcell filter* [49]: an additional resonator centered at the readout frequency that acts as a bandpass filter. Such a filter can be made broadband enough to fit multiple multiplexed readout resonators within its bandwidth while still significantly decreasing the coupling to the external dissipative (50 Ohm) environment at the qubit frequency. This allows the qubits to be frequency tuned without loosing this protection, and results in a relaxation time limit of [50]

$$T_1 = \frac{1}{\kappa}\left(\frac{\Delta}{g}\right)^2\left(\frac{\omega_r}{\omega_{01}}\right)\left(\frac{\Delta}{\omega_r/2Q_F}\right)^2, \tag{2.13}$$

where Q_F is the quality factor of the Purcell filter.

Lastly, the qubit itself can act as an antenna with several detrimental effects. Our recent work [51] shows that common qubit geometries and parameters result in standing wave modes in the 100 GHz range that strongly couple to free space and result in enhanced relaxation times that can easily be limited to tens or hundreds of microseconds. Additionally, the absorption of blackbody radiation through these antenna modes can lead to quasiparticle poisoning that can limit qubit coherence. A more extensive discussion of this work is beyond the scope of this thesis.

2.1.6 Nonequilibrrium quasiparticles

Quasiparticles (QPs) are unpaired electrons that have been excited out of the superconducting ground state. As electrons (fermions), they follow a Fermi-Dirac energy dis-

tribution, and with the further assumption that we are operating in a low-temperature limit in which there are very few quasiparticles that are concentrated near the gap edge, we can find the ratio of electrons that are quasiparticles to be [52]

$$x_{\mathrm{QP}} \equiv \frac{n_{\mathrm{QP}}}{n_{\mathrm{CP}}} = \sqrt{2\pi k_B T/\Delta} e^{-\Delta/k_B T}. \tag{2.14}$$

Here T is the temperature of the superconductor, Δ is the superconducting gap, k_B is the Boltzmann constant, and $n_{\mathrm{QP}}(n_{\mathrm{CP}})$ is the number of quasiparticles (cooper pairs) per unit volume. These thermally excited "equilibrium" quasiparticles are extremely uncommon at dilution refrigerator temperatures, with $x_{\mathrm{QP}} \approx 10^{-53}$ at 20 mK. Experimentally, however, quasiparticle densities have been inferred to be in the range of $x_{\mathrm{QP}} \approx 10^{-9} - 10^{-5}$, corresponding to an effective quasiparticle temperature of 120-210 mK and indicating there are non-thermal sources of quasiparticles that dominate by tens of orders of magnitude.

Non-equilibrium quasiparticles follow an occupation function $f(\epsilon)$ for energy ϵ governed by

$$\frac{df(\epsilon)}{dt} = g(\epsilon) + I^s_{\mathrm{e-ph}} + I^r_{\mathrm{e-ph}} + I_{\mathrm{e-e}}. \tag{2.15}$$

The first term describes the generation of quasiparticles at a rate $g(\epsilon) = \eta_g S_g(\epsilon)\nu_s(\epsilon)$, where η_g is an absorption coefficient, $S_g(\epsilon)$ is the power spectrum of incident radiation (potentially blackbody), and $\nu_s(\epsilon)$ is the density of states in the superconductor. The next two terms describe energy-changing (s)cattering and (r)ecombination between electrons and phonons. The last term describes electron-electron collisions, which are

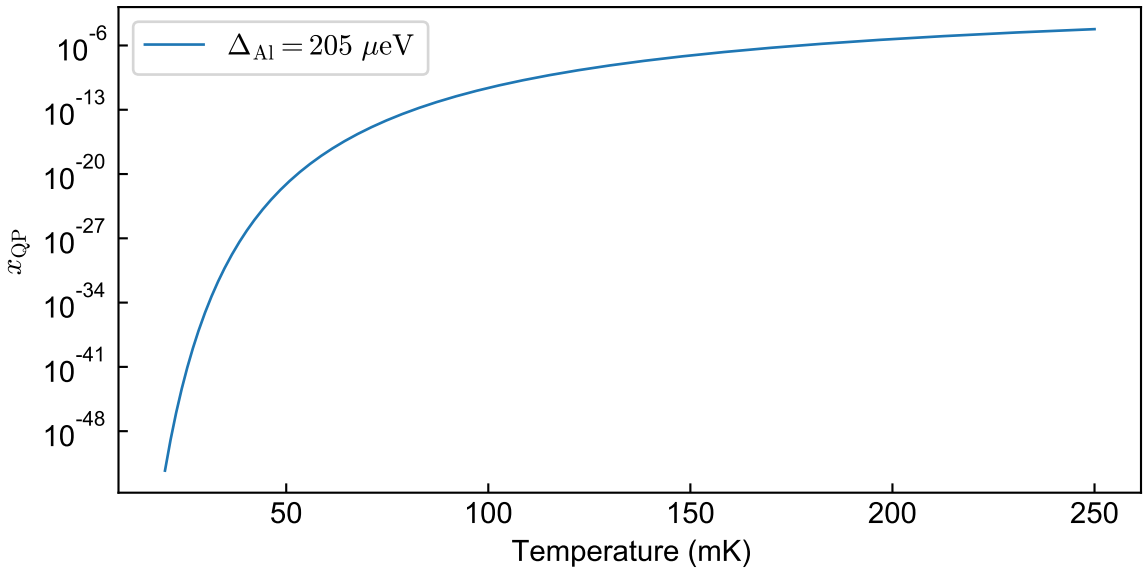

Figure 2.2: **Nonequilibrium quasiparticles.** For the range of temperatures normally reached in modern dilution refrigerators (20 mK), the density of quasiparticles should be absurdly low.

usually vanishingly rare at low QP densities.

Non-equilibrium quasiparticles cause a variety of detrimental effects to superconducting circuits. They can increase the kinetic inductance of superconductors, changing frequencies of resonators and qubits. Every time a quasiparticle tunnels across a junction in a qubit, the parity of the island charge changes by ± 1, changing the qubit frequency by twice the charge dispersion, leading to dephasing errors. The spectrum of tunneling events can be obtained by taking the Fourier transform of a random telegraph process, resulting in [53]

$$S(f) = \frac{4\Gamma_{\mathrm{rts}}}{(2\Gamma_{\mathrm{rts}})^2 + (2\pi f)^2}, \tag{2.16}$$

where Γ_{rts} is the tunneling rate. These tunneling events can lead to excitations or

relaxation of the qubit, with the relative rates given by [54]

$$\Gamma_{10} \approx \frac{x_{\mathrm{QP}}}{\pi}\sqrt{2\Delta\omega_{01}} \tag{2.17}$$

$$\Gamma_{01} \approx \Gamma_{10} e^{-\hbar\omega_{01}/k_B T_{\mathrm{eff}}}. \tag{2.18}$$

One interesting note is that a single quasiparticle on a chip gives a coherence limit on the order of seconds.

Potentially more damaging is photon-assisted tunneling (PAT) processes [55], in which a photon with energy greater than 2Δ is absorbed by a qubit, breaking a Cooper pair across the junction. Noteably, the excitation and relaxation rates are the same for transmons being acted on by PAT processes:

$$\Gamma_{01} \approx \Gamma_{10} \approx \bar{n}_\nu \frac{g^2\omega_r}{\pi\omega_{ij}\omega_\nu}\sqrt{\frac{E_C}{8E_J}}. \tag{2.19}$$

Here we have transmon coupled with rate g to a readout resonator with angular frequency ω_r. An average mode occupation $\bar{n}_\nu$ of photons with angular frequency ω_ν is incident on the transmon, and $\hbar\omega_{ij}$ is the energy between initial and final quasiparticle states. As mentioned briefly in the previous section, the qubit structure itself acts as an efficient resonant absorber of pair-breaking radiation. This could even potentially be a source for the non-equilibrium quasiparticles seen across devices.

2.2 Error correction

Classical computers make errors at remarkably low rates, but are able to use error detection and correction schemes to reduce error rates to even lower levels. Classical errors appear as flipped bits, and can be detected and corrected in a number of ways. Perhaps the simplest way is encoding each bit in three duplicate bits and using majority rules to overcome single bit flips. This can be made more efficient with parity bits or Hamming codes, where a small number of extra bits can detect errors in a much larger array of bits.

The future of quantum computers also relies on having robust error correction, but the problem becomes much harder. For one, the quantum no cloning theorem makes it impossible to duplicate qubits to enact a simple majority rules. The errors themselves are also harder to work with. In addition to bit flips, there are also phase flips, and both operate on a continuum instead of full discrete flips. Lastly, measuring the state of a qubit to see if an error has occured destroys the quantum state stored in that qubit.

Fortunately, numerous clever schemes have been developed that overcome these challenges and make for a promising future of error-resistant quantum computation. Most schemes encode a logical quantum state across numerous qubits, together called a *codeword*, and entangle them with ancilla qubits that can then be measured to detect errors without affecting the original quantum state. Finding the right codewords, along

with *stabilizers* – groups of operators that have an eigenstate of +1 when there has not been an error and -1 when an error has occured – is the key to effective error detection. To enforce eigenvalues of ± 1, we define projectors for a stabilizer A as

$$P_{\pm}^{A} = \frac{I \pm A}{2}. \tag{2.20}$$

This allows us to separate the extended Hilbert space that spans all the qubit states into two subspaces: $P_{+}^{A}|\psi\rangle$ in which no error has occurred, and $P_{-}^{A}|\psi\rangle$, which spans all the states in which an error as occurred.

An important property of stabilizers is that they must commute with each other. They are measured continuously in a cycle during computation, so if they do not commute, information would be lost each time a new stabilizer is measured. For example, after measuring Z_1 (the subscript denotes 'qubit 1'), a subsequent measurement of X_1 will be useless, as the state has been collapsed onto the z-basis. As it turns out, pairs of Pauli matrices commute and make good stabilizers. The operators $Z_1 Z_2$[1] and $X_1 X_2$ have the same eigenstates (Bell states), so sequential measurements do not loose information.

In order to avoid collapsing the quantum state we care about by directly measuring the data qubits, we instead project the stabilizers onto ancilla qubits through controlled gates. An example circuit that detects bit-flip errors is shown in Fig. 2.3. Different stabilizers will indicate (have eigenvalue of -1) errors in different pairs of qubits. By

[1] We re-express the Pauli matrices σ_x, σ_y, and σ_z in the standard syntax for error correction literature, with $X = \sigma_x$, $Y = -i\sigma_y$, and $Z = \sigma_z$.

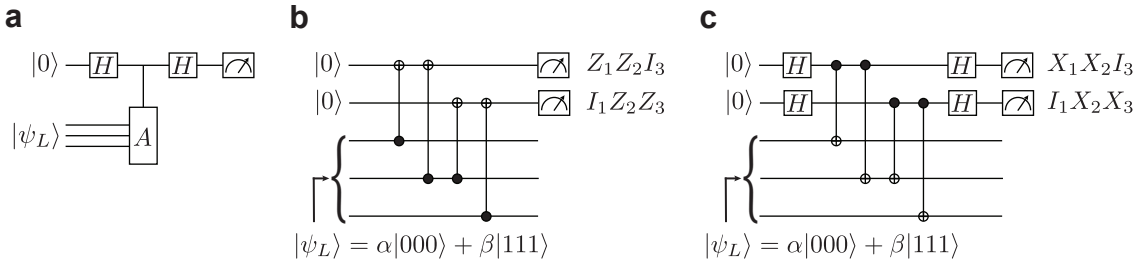

Figure 2.3: **Error correction algorithms.** (**a**) Sandwiching a controlled-A gate between Hadamards projects the result of the stabilizer A onto the ancilla qubit. (**b,c**) Example codes for bit-flip (a) and phase-flip (b) detection. A logical qubit is composed of three data qubits that store a logical quantum state, and two ancilla qubits that can detect errors.

looking at which stabilizers show errors, it is possible to deduce which qubits have errors, and correct them. If only ancilla 1(2) projects to -1, we know qubit 1(3) has an error. If they both go to -1, we know the error is in qubit 2. Of course, if all of them show +1, we know there is no error.

The circuit in Fig. 2.3b shows the measurement of the $Z_1Z_2I_3$ and $I_1Z_2Z_3$ stabilizers. The Z_i's show up as controlled-X gates in order to flip the ancilla qubits as needed. This is a basic bit flip code using three data qubits and two ancillas. A similar code can be developed to detect phase flips using the stabilizers $X_1X_2I_3$ and $I_1X_2X_3$, as shown in part (c) of the same figure.

More generally, for a stabilizer A, we can project the error state onto an ancilla with a controlled-A gate sandwiched between two Hadamard gates, as shown in Fig. 2.3a and executed as follows. Initializing the ancilla to $|0\rangle$ and applying the first Hadamard gate yields the state

$$\frac{1}{\sqrt{2}}(|0\rangle + |1\rangle) \otimes |\psi\rangle. \tag{2.21}$$

Dropping the '$\otimes$' notation and applying the controlled-A gate, we get

$$\frac{1}{\sqrt{2}}(|0\rangle|\psi\rangle + |1\rangle A|\psi\rangle). \tag{2.22}$$

The second Hadamard gate returns

$$\frac{1}{2}[(|0\rangle + |1\rangle)|\psi\rangle + (|0\rangle - |1\rangle)A|\psi\rangle] \tag{2.23}$$

$$= |0\rangle \left(\frac{I+A}{2}\right)|\psi\rangle + |1\rangle \left(\frac{I-A}{2}\right)|\psi\rangle \tag{2.24}$$

$$= |0\rangle P_+^A|\psi\rangle + |1\rangle P_-^A|\psi\rangle. \tag{2.25}$$

Measuring the ancilla qubit collapses the state of the system into one of two states. If the ancilla measures $|0\rangle$, the system is in the no-error state $P_+^A|\psi\rangle = |\psi\rangle$. If the ancilla qubit measures $|1\rangle$, however, we know the data qubit is in an error state $P_-^A|\psi\rangle = -|\psi\rangle$ and corrections need to be made.

This is a crucial result. We have used the measurement of the ancilla qubit to project the state into no error at all or a full bit-flip that can be easily flipped back. Let me emphasize this again. If a qubit undergoes a marginal error in which its state vector is rotated only slightly around the Bloch sphere, measuring the ancilla projects that rotation onto either no rotation or a full π-rotation.

Let's continue to look at our three-qubit bit-flip code as an example. We want

to preserve the quantum state $|\psi\rangle = \alpha|0\rangle + \beta|1\rangle$. Using controlled-not gates, we can encode this state in a three-qubit codeword, $|\psi_L\rangle = \alpha|000\rangle + \beta|111\rangle$, where the '$L$' subscript denotes 'logical.' As previously mentioned, the bit-flip stabilizers for this code are $Z_1Z_2I_3$ and $I_1Z_2Z_3$. We entangle the data qubits with two ancilla qubits, giving us

$$|\psi\rangle = (\alpha|000\rangle + \beta|111\rangle) \otimes |00\rangle. \tag{2.26}$$

Let us now consider a small rotation of data qubit 1, such that $|0\rangle \rightarrow \gamma|0\rangle + \delta|1\rangle$. This brings our system state to

$$|\psi\rangle_{\text{err}} = [\gamma(\alpha|000\rangle + \beta|111\rangle) + \delta(\alpha|100\rangle + \beta|011\rangle)] \otimes |00\rangle. \tag{2.27}$$

In our error correction algorithm, the stabilizer is sandwiched between two Hadamard gates. Each controlled-Z gate, when combined with the Hadamards, becomes a controlled-X (CNOT) gate, since $HZH = X$. After this CNOT gate, we are left with the state

$$|\psi\rangle = \quad (\alpha|000\rangle + \beta|111\rangle) \otimes \gamma|00\rangle \tag{2.28}$$

$$+ \ (\alpha|100\rangle + \beta|011\rangle) \otimes \delta|10\rangle. \tag{2.29}$$

After measuring the ancilla qubits, the system is projected into the original errorless state with probability $|\gamma|^2$, or into a state with a full bit flip, with probability $|\delta|^2$. In both cases, our quantum state stored in α and β is preserved, and appropriate corrections can be made.

We have now introduced a simple algorithm to correct bit-flip errors without destroying the quantum state of the data qubits. A similar algorithm exists for correcting phase-flips using the stabilizers $X_1X_2I_3$ and $I_1X_2X_3$. Errors will manifest as X-, Y-, or Z-rotations, but since $Y = ZX$ rotations can be composed of X- and Z-rotations, it is sufficient to correct for bit-flips and phase-flips. By concatenating the bit-flip and phase-flip correction codes, a nine-qubit code can be developed that can detect and correct any arbitrary errors on the qubits, provided that errors occur infrequently enough that two qubits will not simultaneously need to be corrected. This limit on error frequency is commonly referred to as the *fault tolerant threshold*.

2.2.1 The surface code

The nine-qubit code, along with the related five- and seven-qubit codes, require a high level of connectivity between all the qubits, and the thresholds on fault tolerance are higher than current qubits have managed. A much more lenient scheme is the *surface code* [56], which requires only nearest neighbor connectivity, and currently achievable fidelities, at the expense of using many qubits per logical qubit. The surface code works within a lattice of data qubits, each of which is surrounded by two sets of four ancilla qubits. Qubits in the first set of ancillas enforce $Z_aZ_bZ_cZ_d$ stabilizers on the surrounding data qubits (labeled a, b, c, and d), while the second group of ancillas enforces $X_aX_bX_cX_d$ stabilizers.

This lattice can hold an arbitrary quantum state $|\psi\rangle$ and correct errors that alter it, but we still need to define logical qubits and be able to implement gates between them. To make a logical qubit, we stop enforcing pairs of stabilizers. This relaxes a degree of freedom such that if two measure-Z (measure-X) qubits are not measured, X-flips (Z-flips) in a chain between the "defects" cannot be detected, nor can a loop of Z-flips (X-flips) around a defect. This gives us logical operators X_L and Z_L that can be applied to a logical qubit. Inter-qubit (ex: CNOT) gates can be performed by dragging qubits through and around each other. To measure a logical qubit, we simply start measuring the stabilizers again. The measured stabilizer eigenvalue will be a projection of the logical qubit state.

The surface code is described in much more detail in Ref. [56], but I wanted to give a brief overview here before mentioning correlated errors. As it turns out, errors that effect multiple qubits in a row can be much more damaging. More specifically, for some single-qubit error threshold p given by the surface code, and for an error that couples to m qubits in a row, the fault-tolerant threshold for correlated errors becomes [57]

$$p_m \approx p^m. \tag{2.30}$$

Correlated errors are then exponentially more damaging to the surface code, and need to be studied carefully. In chapter 5 we will look at correlated errors due to particle impacts with the qubit chip substrate.

Chapter 3

Anomalous charge noise in superconducting qubits[1]

We have used Ramsey tomography to characterize charge noise in a weakly charge-sensitive superconducting qubit. We find a charge noise that scales with frequency as $1/f^{\alpha}$ over 5 decades with $\alpha = 1.93$ and a magnitude $S_q(1\,\mathrm{Hz}) = 2.9 \times 10^{-4}\ e^2/\mathrm{Hz}$. The noise exponent and magnitude of the low-frequency noise are much larger than those seen in prior work on single electron transistors, yet are consistent with reports of frequency noise in other superconducting qubits. Moreover, we observe frequent large-amplitude jumps in offset charge exceeding $0.1e$; these large discrete charge jumps are incompatible with a picture of localized dipole-like two-level fluctuators. The data reveal an unexpected dependence of charge noise on device scale and suggest models

[1] This chapter is a lightly edited and reformatted version of Ref. [58].

involving either charge drift or fluctuating patch potentials.

Superconducting quantum circuits are a leading physical platform for scalable quantum computing, with small-scale qubit arrays nearing the threshold of quantum supremacy [19, 59]. The progress of recent years has been enabled by designs that isolate the qubit mode from sources of noise and dissipation inherent in the materials used to realize the device. However, these approaches entail design compromises that could impede continued scaling. For example, the highly successful transmon design [28] achieves exponential insensitivity against charge noise at the expense of reduced anharmonicity. As a result, leakage out of the computational subspace represents a significant problem for large-scale transmon arrays, as it cannot be mitigated with standard error correction codes [60]. At the same time, there are proposals for new qubit designs that provide protection against noise at the hardware level, including charge-parity qubits [61, 62], fluxon pair qubits [63], and 0-π qubits [64]. However, in many of these implementations one needs accurate control over the offset charge environment. These considerations motivate a detailed study of charge noise in modern superconducting qubit circuits.

Excess low-frequency charge noise (or equivalently electric field noise) impacts a wide range of physical systems, including nitrogen-vacancy centers [65], trapped ions [66], semiconducting quantum dots [67], and single electron transistors (SETs) [68–76], and there has been extensive prior work to understand the origin and scaling of the

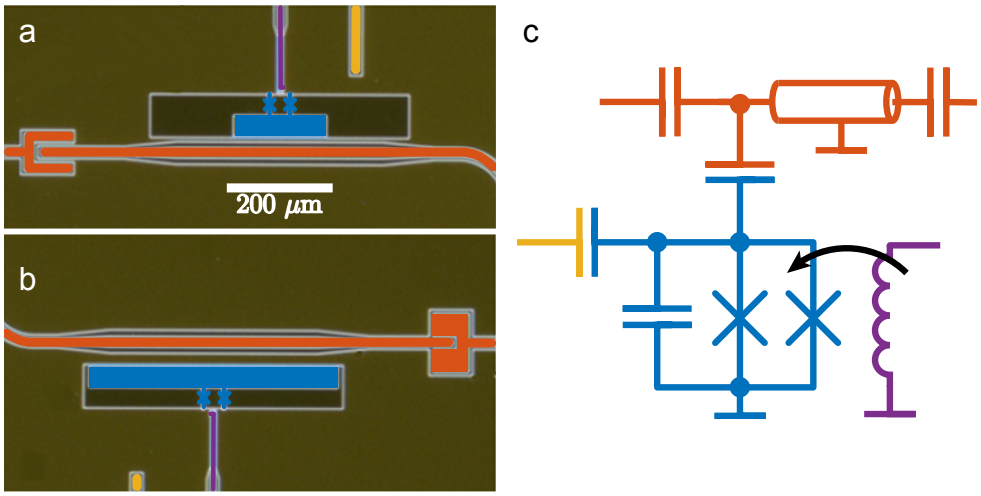

Figure 3.1: **Device geometry.** Micrograph of the charge-sensitive qubit (**a**; $E_C/h =$ 390 MHz, $E_J/h = 10.8$ GHz) and the reference transmon (**b**; $E_C/h = 230$ MHz, $E_J/h = 16$ GHz). The qubit structures are shown in blue; the readout resonator and feedline are red; and the charge and flux bias lines are colored orange and purple, respectively. (**c**) Diagram of the qubit circuit.

noise. Previous measurements in SET devices and first-generation charge qubits [77] showed a $1/f$ power spectral density $S_q(f) \propto 1/f^\alpha$ with α between 1.0 and 1.25 [67–77] and noise magnitude $S_q(1\,\mathrm{Hz}) \sim 10^{-5} - 10^{-7}$ e^2/Hz. The standard microscopic picture of this noise is a distribution of two-level fluctuators (TLF) [75, 78, 79] that can activate or tunnel between local minima in a potential energy landscape, leading to switching behavior in the time domain and a Lorentzian power spectral density. A bath of TLF with a broad distribution of characteristic rates gives rise to the ubiquitous $1/f$ noise.

Here we describe measurements of charge noise in a charge-tunable qubit that departs slightly from the transmon regime. We find a charge noise power spectral density that is up to 4 orders of magnitude larger at 1 Hz than that seen in SETs, suggest-

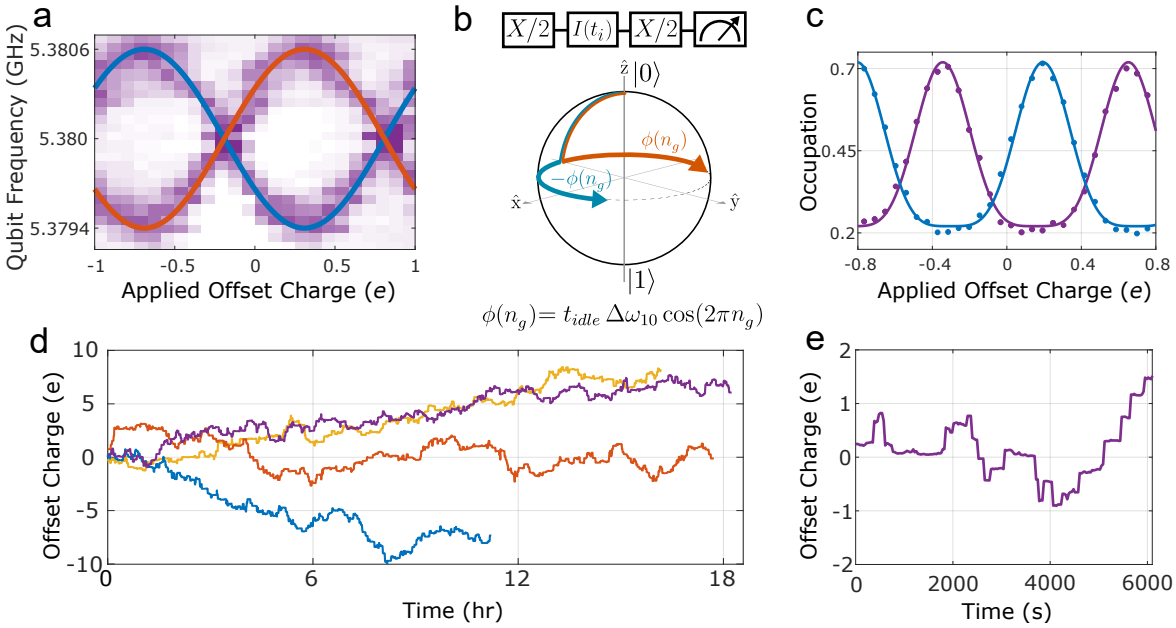

Figure 3.2: Ramsey-based extraction of offset charge. (a) Qubit spectroscopy versus charge bias at the flux-insensitive point. As QP tunneling rates far exceed the experimental repetition rate, we observe both QP parity bands (red and blue traces). (b) Pulse sequence used to estimate the offset charge, along with diagram of the trajectory of the qubit state vector on the Bloch sphere for the two values of QP parity. (c) Representative Ramsey-based charge tomography for two values of δn_g. The pulse sequence of (b) is repeated for a range of applied offset charge. From a fit to Eq. (3.1) we extract the change to the island offset charge δn_g due to intrinsic noise processes. (d) Time series of fluctuating offset charge. (e) Expanded view of measured δn_g. Frequent large-magnitude ($> 0.1e$) jumps are clearly visible.

ing an unexpected dependence of the noise on device scale. Moreover, we observe a large number of discrete charge jumps in excess of $0.1e$. The measured distribution of charge jumps is not compatible with charge motion over microscopic length scales, as described by the standard picture of dipole-like TLF. Finally, the measured noise exponent $\alpha = 1.9$ is incompatible with the exponents reported for SETs, pointing to a new noise mechanism. While our measured noise is strikingly different from that seen in SETs, it is consistent with reports of frequency noise in other superconducting qubits [80, 81].

The device geometry is shown in Fig. 3.1. Each die consists of a charge-sensitive qubit and a charge-insensitive reference transmon coupled to a common $\lambda/2$ readout resonator. The devices were fabricated on high-resistivity silicon; the circuit ground-plane, qubit islands, and all control and readout elements were made from sputtered niobium and defined using optical lithography and reactive ion etching. The Al-AlO_x-Al compound Josephson junctions of the qubits were fabricated using electron-beam lithography and double-angle evaporation[2].

The qubit parameters are $E_J/h = 10.8$ GHz at the flux-insensitive point and $E_C/h = 390$ MHz, corresponding to a qubit transition frequency $\omega_{10}/2\pi = 5.38$ GHz. The readout mode resonates at 6.744 GHz. The qubit is coupled to the resonator with a coupling strength of $g/2\pi = 100$ MHz and the state is read out dispersively with a

[2]The devices were originally designed to probe correlations of low-frequency flux and charge noise; these measurements, which set an upper limit on flux-charge correlations at 6%, are described in the next chapter.

qubit state-dependent shift of $\chi/\pi = 3.7$ MHz. The resonator is strongly coupled to the output port with a decay time $1/\kappa = 75$ ns to allow for rapid repeated measurements. The offset charge is controlled through an on-chip capacitance to the qubit island of 100 aF, with a 20:1 voltage division at the millikelvin stage. The device is measured in a dilution refrigerator with a base temperature of 35 mK.

While typical transmon devices involve a ratio E_J/E_C in the range 50-100 [28, 82], leading to a charge dispersion ranging from 10 kHz to 1 Hz, the ratio $E_J/E_C = 28$ yields a charge dispersion $\Delta\omega_{10}/2\pi = 600$ kHz. The qubit energy spectrum is given by $\overline{\omega_{10}} + \Delta\omega_{10}\cos(2\pi n_g)$, where $\overline{\omega_{10}}$ is the charge-averaged qubit frequency and n_g is the offset charge on the qubit island expressed in units of $2e$ (Fig. 3.2a). The dependence of the qubit transition frequency on offset charge renders the device sensitive to quasiparticle (QP) poisoning [83]. Here, single QPs tunnel across the Josephson junctions on sub-millisecond timescales [80, 81], changing n_g by 0.5 and giving rise to distinct parity bands in the qubit spectrum.

To measure fluctuations in the offset charge on the qubit island, we perform a series of Ramsey experiments at varying charge bias points using a pulse sequence that maps offset charge onto population of the qubit excited state (Fig. 3.2b). With QP tunneling rates far exceeding the repetition rate of the Ramsey experiments, we require the experiment to be independent of parity of the qubit island. The sequence begins with a broadband (40 ns long) $X/2$ gate that addresses both parity bands.

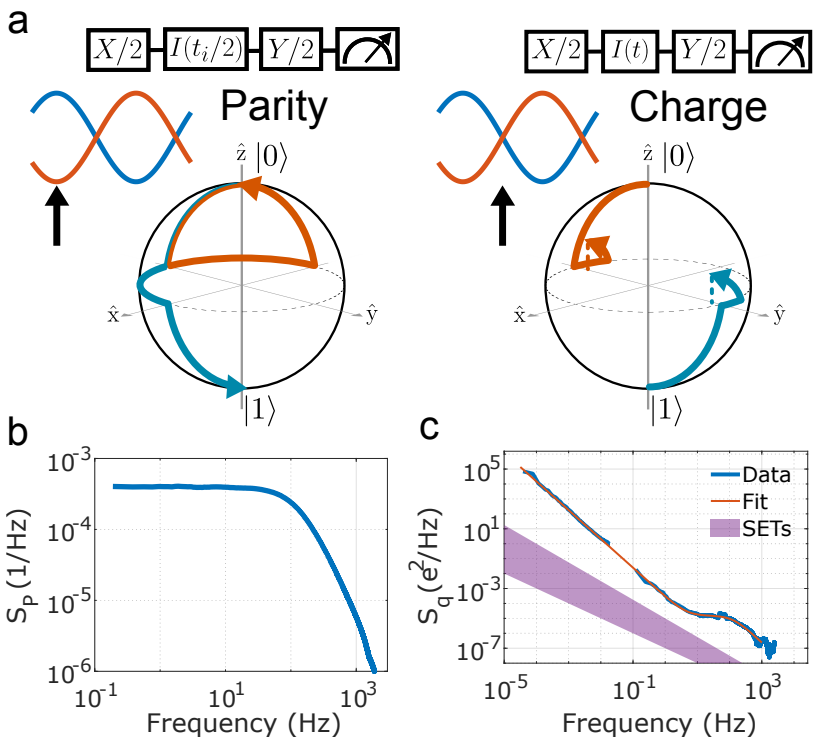

Figure 3.3: (a) Pulse sequences for Ramsey-based single-shot measurement of QP parity and charge noise. In the first sequence, the qubit is biased to a parity-sensitive point; the $X/2$ – idle – $Y/2$ sequence is designed to map QP parity to the north and south poles of the Bloch sphere. The sequence is immediately followed by a second experiment that maps fluctuating offset charge to qubit population. Here the device is biased to the point of maximal charge sensitivity; following an initial $X/2$ pulse, states that reside on the two QP parity bands accumulate phase with opposite sign; a final $Y/2$ pulse maps the qubit state to the same polar angle on the Bloch sphere irrespective of QP parity. (b) Power spectral density of QP parity fluctuations. The spectrum is Lorentzian with a characteristic frequency at $\Gamma/2\pi = 255$ Hz. (c) Power spectral density of offset charge noise. The low-frequency portion of the spectrum is obtained from the time series presented in Fig. 3.2d, while the high-frequency portion of the spectrum is derived from the single-shot protocol of (a). Residual QP tunneling dominates the spectrum above 10 Hz. The orange trace is a fit to the sum of a power law spectrum $S_q(f) = A/f^{\alpha}$ and a single Lorentzian. We find $S_q(1\,\mathrm{Hz}) = 2.9 \times 10^{-4}$ e^2/Hz and $\alpha = 1.93$.

The qubit then undergoes free evolution for an interval t_i, accumulating the phase $\pm\Delta\omega_{10} t_i \cos 2\pi n_g$, where the two signs correspond to the two possible parity states. While the two parity states evolve in different directions around the equator of the Bloch sphere, they maintain the same projection onto the y-axis. We set the idle time $t_i = \pi/\Delta\omega_{10}$ and use a final $X/2$ gate to map this projection onto the z-axis of the Bloch sphere. Measurement of the qubit finds an excited state probability

$$P_1 = \frac{1}{2}\left[d + \nu \cdot \cos(\pi \cos 2\pi n_g)\right], \tag{3.1}$$

where $n_g = n_g^{\text{ext}} + \delta n_g$ is the sum of an applied gate charge n_g^{ext} and a fluctuating intrinsic offset charge δn_g and the parameters d and ν account for qubit decay during measurement and finite measurement visibility, respectively. Critically, P_1 is periodic in offset charge with period $n_g = 0.5$, and is thus insensitive to QP parity. We sweep the externally applied gate charge n_g^{ext} and determine δn_g by fitting the measured Ramsey data to Eq. (3.1). Using this technique, we can determine the offset charge to a precision of $0.02e$ over 20 s. Once δn_g is measured, we can then deterministically bias to any point in charge space.

Repeated Ramsey scans of this type generate a time series of fluctuating offset charge (Fig. 3.2d). Interestingly, the charge trace shows occasional (once per $\sim$250 s) extremely large discrete jumps $> 0.1e$. The observed distribution of offset charge jumps is difficult to reconcile with a model of dipole-like microscopic TLF. Note that, as Ramsey tomography is periodic in an offset charge of $1e$, we can only determine

changes in offset charge within the range $[-0.5e, 0.5e)$; any larger jump is aliased to a reduced value of offset charge (e.g., a $0.6e$ change looks identical to a -0.4e change).

In order to characterize the fluctuating offset charge at higher frequency, we adopt a fast single-shot Ramsey protocol that simultaneously probes island parity and fluctuating offset charge (Fig. 3.3a). An initial Ramsey sequence maps the two parity states to the north and south poles of the Bloch sphere. Single-shot measurement of the qubit state provides access to QP parity of the qubit island. Following a short delay of 1 μs $\sim 13/\kappa$ to allow the cavity to return to its ground state, we perform a second single-shot Ramsey experiment that maps offset charge to qubit population irrespective of island parity. We bias the qubit to the point of maximal charge sensitivity and perform an $X/2$ gate that rotates the qubit parity states to opposite sides of the equator of the Bloch sphere. Noise in the charge bias causes the two states to accumulate phase in opposite directions; however, a subsequent $Y/2$ gate maps the accumulated phase to the same polar angle on the Bloch sphere. Due to the presence of large jumps in offset charge on a few-minute timescale, we interleave with this sequence a separate Ramsey-based scan of offset charge every 15 s in order to compensate large jumps in offset charge. By repeating the two-step protocol with a duty cycle of 10 kHz, we generate two time series of single-shot measurement results, the first of which provides access to island parity and the second of which provides access to fluctuating offset charge. For each separate time series (QP parity or charge), we partition the time

trace into two interleaved traces, compute the cross spectrum, and average over many measurement cycles to suppress quantum projection noise, after [84, 85].

The power spectrum of QP parity (Fig. 3.3b) is Lorentzian with a characteristic frequency of 255 Hz set by the rate of QP tunneling onto or off of the qubit island; this QP poisoning rate is consistent with other reported values in the superconducting qubit literature [80, 81]. For the charge noise results (Fig. 3.3c), we combine the fast single-shot Ramsey results with the low-frequency charge noise power spectral density obtained from the time series presented in Fig. 3.2d. The power spectral density of offset charge fluctuations displays a $1/f^{\alpha}$ spectrum, with $S_q(1\,\mathrm{Hz}) = 2.9 \times 10^{-4}$ e^2/Hz and $\alpha = 1.93$. The measured charge noise is inconsistent with a large body of literature on charge noise in SETs, both in the noise magnitude at 1 Hz and in the noise exponent.

While charge noise has not previously been reported on weakly charge-sensitive qubits of the transmon type, there are reports of frequency noise [80, 81]. To compare our data to these prior experiments, we convert our measured offset charge to difference frequency using the relation $\delta f = |\Delta\omega_{10} \cos(2\pi n_g)|$. In this case, we find $S_{\delta f}(1\,\mathrm{Hz}) = 5.9 \times 10^7$ Hz^2/Hz with noise exponent $\alpha = 1.76$, which closely matches the other measured values (after proper normalization to the same charge dispersion) of $S_{\delta f}(1\,\mathrm{Hz}) = 8.1 \times 10^7$ Hz^2/Hz and $\alpha = 1.7$ [80], and $S_{\delta f}(1\,\mathrm{Hz}) = 3.7 \times 10^7$ Hz^2/Hz and $\alpha = 1.70$ [81]. More details on this comparison can be found in the next chapter. While a conversion from frequency noise to charge noise is not possible due to

non-trivial aliasing effects, the similar levels of frequency noise seen in these three independent qubit measurements suggest a common noise mechanism, despite the fact that these measurements span a range of substrate materials (Si – this work; Al_2O_3 – [80, 81]), base metal (Nb – this work; Al – [80, 81]), and cavity architecture (2D –this work; 3D – [80, 81]).

As this noise is substantially larger than what is seen in SET devices, it is instructive to consider the differences between the two systems. First, SETs are operated in the voltage state, whereas transmons are operated in the superconducting state. Naively one might expect to observe higher levels of noise in devices operated in the dissipative regime; SET measurements confirm this intuition, where higher voltage bias results in larger noise [72, 74]. The other notable distinction is the large qubit capacitor pad. For our charge-sensitive device, with qubit charging energy $E_C/h = 390$ MHz, the island dimensions are 40×180 μm^2. For typical SETs, the island dimensions are submicron and charging energy is of order 40 GHz [86, 87]. It is thus reasonable to consider whether the enhanced noise seen in our devices is related to the difference in device scale. In the most widely accepted picture of low-frequency charge noise, the fluctuating offset charge is due to dipole-like TLF involving motion of a single electron charge over microscopic scales, with dipole moments of order 1 Debye [37]. Such dipolar fluctuators can only produce large changes in offset charge when they are located within a dipole length from the junction, which represents the boundary

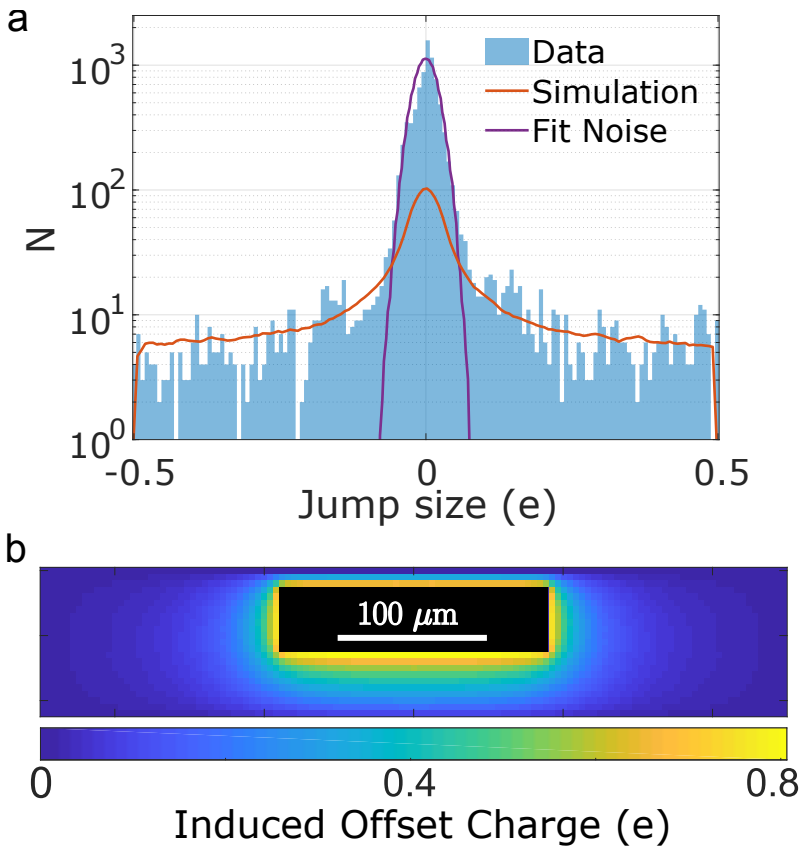

Figure 3.4: (a) Histogram of discrete jumps in offset charge taken from 60 hours of data. The histogram displays a large central peak and a long tail of large-magnitude jumps in offset charge. The purple trace is a Gaussian with width $0.02e$, corresponding to the fit uncertainty in our Ramsey-based charge measurements, while the orange trace is obtained from the numerical simulation in (b), which shows the offset charge associated with impingement of discrete $1e$ charges in the dielectric space between the qubit island and ground. Here the qubit island is shown in black and field of view extends out to the circuit groundplane. The orange trace in (a) is generated by interpolating the simulation results and aliasing large offset charges to the interval [-0.5e, 0.5e), as occurs in the measured data.

between the island and ground electrodes. For TLF with characteristic dipole moment of several Debye, this length is on the order of 1 Å. However, we observe a broad distribution of discrete jumps in offset charge, with many large jumps in excess of $0.1e$. In Fig. 3.4 we plot the histogram of discrete charge jumps obtained from the time series in Fig. 3.2. In addition to a Gaussian central peak with width $0.02e$ set by the fit uncertainty in our Ramsey-based charge measurements, the histogram displays long tails corresponding to a large number of discrete charge jumps extending out to $\pm 0.5e$ (as described above, any larger charge jumps are aliased into this interval). The frequency of large-magnitude charge jumps suggests a model involving motion or drift of charge as opposed to fluctuations of individual localized TLF.

Indeed, the measured histogram is well modeled by random impingement of charge in the dielectric space between the qubit island and the ground electrode (see Fig. 3.4). Here, we perform a COMSOL simulation to calculate the induced charge on the qubit island associated with nucleation of a discrete $1e$ charge in the dielectric space between the qubit island and the circuit groundplane (Fig. 3.4b). We then permit both charge polarities, which would correspond either to the nucleation of both positive and negative charged particles, or to the adsorption/desorption of a single charged species. We sample the entire groundplane cavity with uniform density, appropriately alias the data to account for the finite dynamic range of our charge measurement (so that, e.g., $0.6e$ is mapped to $-0.4e$), and histogram the results. This naive simulation yields surprising

agreement with the measured distribution of discrete charge jumps. Within a picture of impingement of discrete charges in the dielectric cavity of the qubit groundplane, the measured rate of charge jumps corresponds to a flux of charged particles of $17/\mathrm{cm}^2 \cdot \mathrm{s}$, which could be due, e.g., to a partial pressure of charged species of order 10^{-22} Torr. This pressure corresponds to roughly 0.4 ions in the Al box housing the sample, so the drift of charge might be better viewed as due to some element within the sample box that releases charge at a rate of ~ 500 particles per second. For example, the charge could be generated from the relaxation of strain in the PCB material used to couple signals into and out of the sample box or from the relaxation of strain in the dielectric substrate itself. Alternatively, it could be that free charge is generated by cosmic rays that are absorbed in the qubit substrate or in the material of the sample enclosure. However, the flux of cosmic rays is only $0.025/\mathrm{cm}^2 \cdot \mathrm{s}$ at sea level [88–90], likely too low to account for observed rate of discrete charge jumps.

Moreover, the large noise exponent is consistent with charge drift, as white current noise yields a charge spectrum that scales with frequency as $1/f^2$. For example, it could be that the apparent scale dependence of charge noise is due to a device-dependent sensing area to a fixed background drift of charge in the substrate or in the vacuum environment of the qubit, e.g., due to the motion of ions in the native oxide of the silicon substrate [91, 92] or to the trapping and release of charged particles in the substrate or surrounding dielectrics due to the relaxation of thermal strain. However,

other models are possible, including fluctuating patch potentials on the island electrode [93, 94], for which one would expect the charge noise to scale linearly with the area of the qubit island. We anticipate that systematic study of the dependence of charge noise on device geometry will elucidate the underlying noise mechanism. Experiments looking at the scale dependence of charge noise will be the focus of section 4.6, and will directly lead to the discovery of the correlated errors that are the focus of chapters 5 and 6.

In conclusion, we have used a charge-sensitive variant of the transmon qubit to characterize anomalous low-frequency charge noise. The large noise magnitude, the noise exponent approaching 2, and the high density of large discrete charge jumps $> 0.1e$ are incompatible with the vast body of literature on charge noise in SETs yet consistent with prior reports of frequency noise in superconducting qubits, indicating a surprising dependence of charge noise on device scale. A deeper understanding of charge noise could guide the development of noise mitigation strategies that will open the design space for superconducting qubits, leading to devices with stronger anharmonicity that are less prone to leakage errors and thus more amenable to scaling.

Chapter 4

Supplementary information for "Anomalous charge noise in superconducting qubits"[1]

4.1 Fabrication details

The devices are realized through single-layer fabrication on high-resistivity ($> 20\ \mathrm{k\Omega \cdot cm}$) Si(100) wafers. After stripping the native SiO_x with hydrofluoric acid, a 90 nm film of Nb is deposited at a rate of 45 nm/min. under conditions optimized to achieve slight compressive film stress. All features except the qubit junctions are then defined with an i-line projection aligner, and the Nb is etched using a Cl_2/BCl_3 recipe in an

[1] This chapter is a lightly edited and reformatted version of Ref. [58].

inductively coupled plasma reactive ion etch tool.

Qubit junctions are then made using a standard Dolan bridge process with a MMA/PMMA stack. Following an *in situ* ion mill to ensure good metallic contact with the base Nb layer, the Al-AlO_x-Al junctions are formed by double-angle electron-beam evaporation of Al and thermal oxidation in a 90/10 Ar/O_2 mixture.

4.2 Qubit coherence

We measured two nominally identical qubits, which we call qubit A and qubit B; qubit A is described in detail in the previous chapter. The energy relaxation time T_1 at the flux-insensitive point was 8.0 μs for qubit A and 7.6 μs for qubit B. These values are on par with those measured in other qubits made with the same junction process and do not appear to be affected by the deviation from the standard transmon regime.

Ramsey scans performed at the flux-insensitive point yield pure dephasing times T_ϕ of 9.8 μs and 11.4 μs for qubits A and B, respectively. The Ramsey envelopes are well fit by decaying exponentials (as opposed to Gaussians), hinting that photon shot noise in the readout resonator, rather than charge noise, is likely the limit of T_ϕ. The measured pure dephasing times correspond to effective temperature of the readout resonators around 70 mK.

4.3 Comparison of $S_{\delta f}$ and S_q

To compare with the power spectra of frequency fluctuations presented in [80, 81], we convert our time series of offset charge to time series of difference frequency using the relation $\delta f = |(\Delta\omega_{10}/2\pi)\cos 2\pi n_g|$. The resulting power spectra of our data and of [80, 81] are plotted in Fig. 4.1b. The spectrum from the Ristè work is taken from the fit in Fig. S4 of [80]. The spectrum from Serniak *et al.* is calculated from a raw time series provided by those authors. As the difference frequency can only vary between 0 and $\Delta\omega_{10}/2\pi$, at long time scales there is a white noise ceiling, as the variation in difference frequency is capped. To allow direct comparison of the frequency noise, we normalize all frequency spectra to match the 600 kHz charge dispersion in our qubit A: the device of Serniak *et al.* has a charge dispersion of 1.6 MHz, so we scale their spectrum by 0.14; while the device of Ristè *et al.* has an 880 kHz charge dispersion, so we scale their spectrum by 0.46.

To extract the magnitude and exponent of the frequency noise, we fit the spectrum from 10^{-3} to 10^{-2} Hz for our data and from 10^{-3} to 10^{-1} Hz for [81]. We find for our measurements $\alpha = 1.76$ and $S_{\delta f}(1\,\mathrm{Hz}) = 5.9 \times 10^7$ $\mathrm{Hz}^2/\mathrm{Hz}$; for the data of Serniak *et al.* we find $\alpha = 1.70$ and $S_{\delta f}(1\,\mathrm{Hz}) = 3.7 \times 10^7$ $\mathrm{Hz}^2/\mathrm{Hz}$; while Ristè *et al.* cite $\alpha = 1.7$ and $S_{\delta f}(1\,\mathrm{Hz}) = 3.8 \times 10^7$ $\mathrm{Hz}^2/\mathrm{Hz}$.

As noted in the previous chapter, the conversion from δf to n_g is not possible due to aliasing effects, thus there is no one-to-one mapping between the two func-

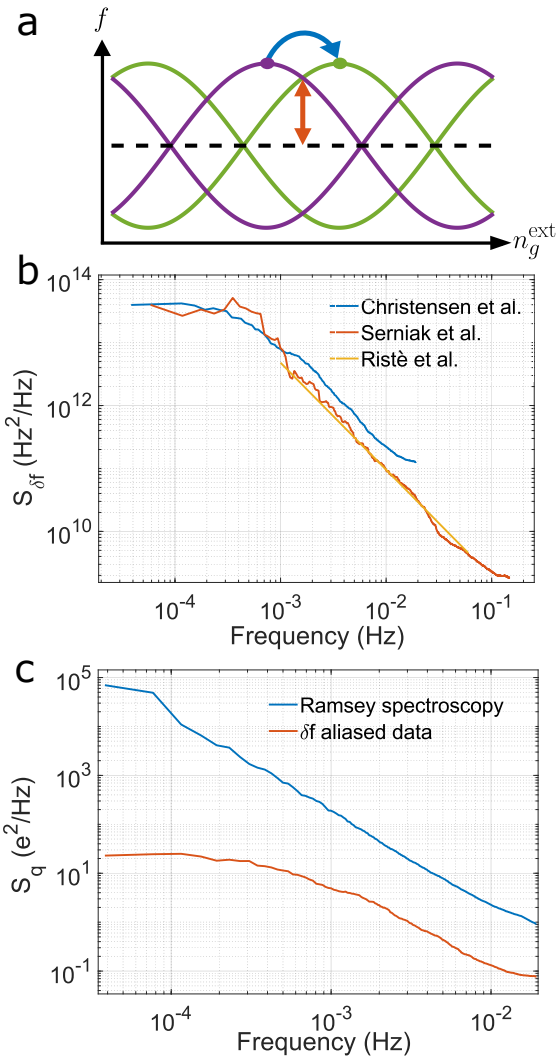

Figure 4.1: **Comparison of $S_{\delta f}$ and S_q.** (**a**) Cartoon showing the two measurement techniques. The purple and green curves correspond to two instances of δn_g. The approach used in the previous chapter (blue arrow) tracks the peak in the charge dispersion curve by sweeping n_g^{ext} and fitting the resulting curve, yielding a dynamic range $[-0.5e, 0.5e)$. The technique in [80, 81] tracks δf (red arrow), which aliases all charge fluctuations into the interval $[0, 0.5e]$. (**b**) Plot of $S_{\delta f}$ for our data and [80, 81]. The data sets show similar noise magnitude and exponent, suggesting a similar underlying noise mechanism. (**c**) Plot comparing S_q taken with the two techniques. The blue curve is the charge spectrum presented in the previous chapter, while the orange curve is the result of mapping from offset charge to difference frequency and back to the offset charge interval $[0, 0.5e]$.

tions (Fig. 4.1a). Our Ramsey-based approach can be thought of as tracking the full spectroscopy curve as a function of n_g by sweeping n_g^{ext}. By tracking the full charge dispersion curve, we can monitor long-term drifts, with the only aliasing arising when two consecutive measurements differ in offset charge by a value larger than $\pm 0.5e$. If instead (as in the works of [80, 81]) no external bias is used and only the difference frequency at a single bias point is measured, then every data point is mapped to the interval $[0, 0.5e]$. An example of this is shown in Fig. 4.1a, where two different instances of δn_g are displayed. With access only to difference frequency at a single bias point, it is impossible to uniquely determine the value of δn_g that produced the measured δf, and therefore an arbitrary choice must be made to assign a value to δn_g. This arbitrary choice must be made any time n_g nears the boundary of the interval $[0, 0.5e]$, as, e.g., $n_g = 0.6$ and $n_g = 0.4$ both correspond to the same difference frequency. Thus δn_g can never leave the interval $[0, 0.5e]$. Critically, this aliasing applies to *every* measurement, whereas the aliasing from our approach only applies to *changes* in offset charge between two measurements that exceed $\pm 0.5e$.

The impact of the aliasing is shown in Fig. 4.1c. Here, we plot the charge noise power spectral density measured via Ramsey tomography in blue. We then convert our data to a time series of δf, and finally map from δf back to the gate charge interval $[0, 0.5e]$. The power spectrum of the intentionally aliased data is plotted in orange. For the aliased data, we see a reduction of the noise exponent from 1.93 to 1.76, a

reduction in the noise power by approximately two orders of magnitude, and a white noise ceiling at frequencies below 3×10^{-4} Hz.

4.4 Measurements of qubit B

A second, nominally identical device (qubit B) was characterized in the same cooldown that yielded the data presented in the previous chapter. The only difference between the devices was a slightly reduced E_J of 9.9 GHz for qubit B compared to 10.8 GHz for qubit A. Time series of fluctuating offset charge in qubit B are shown in Fig. 4.2a. The charge power spectral density calculated from this data shows $\alpha = 1.87$ and $S_q(1\,\mathrm{Hz}) = 1.6 \times 10^{-4}$ e^2/Hz (Fig. 4.2b). The histogram of discrete charge jumps measured in qubit B is shown in Fig. 4.2c along with the results of simulations of the type described in the previous section. In this case, the measurement cycle time was 30 s and the Gaussian central peak in the charge histogram corresponds to a fit uncertainty of $0.01e$. We find large discrete jumps in offset charge at a rate of one event per 290 s, corresponding to an impingement rate of $15/\mathrm{cm}^2 \cdot \mathrm{s}$.

4.5 Charge-flux noise correlation

A complete microscopic picture of low-frequency $1/f$ charge and flux noise is still lacking. To aid in the understanding of these noise sources, we performed a series

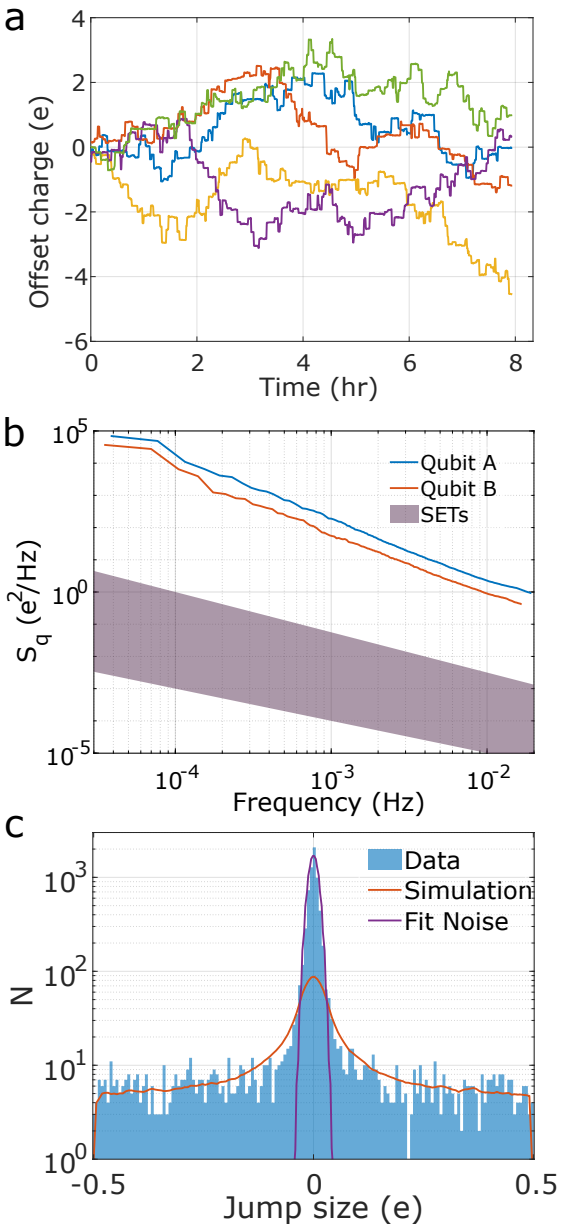

Figure 4.2: **Measurements of qubit B.** (**a**) Time series of offset charge in qubit B. (**b**) Low-frequency charge noise power spectral densities for qubits A and B, along with the range of charge noise seen in SETs. (**c**) Histogram of discrete charge jumps in qubit B. The solid traces represent the simulation of discrete charging events after the method of Section III (red) and Gaussian measurement uncertainty with width $0.01e$ (purple).

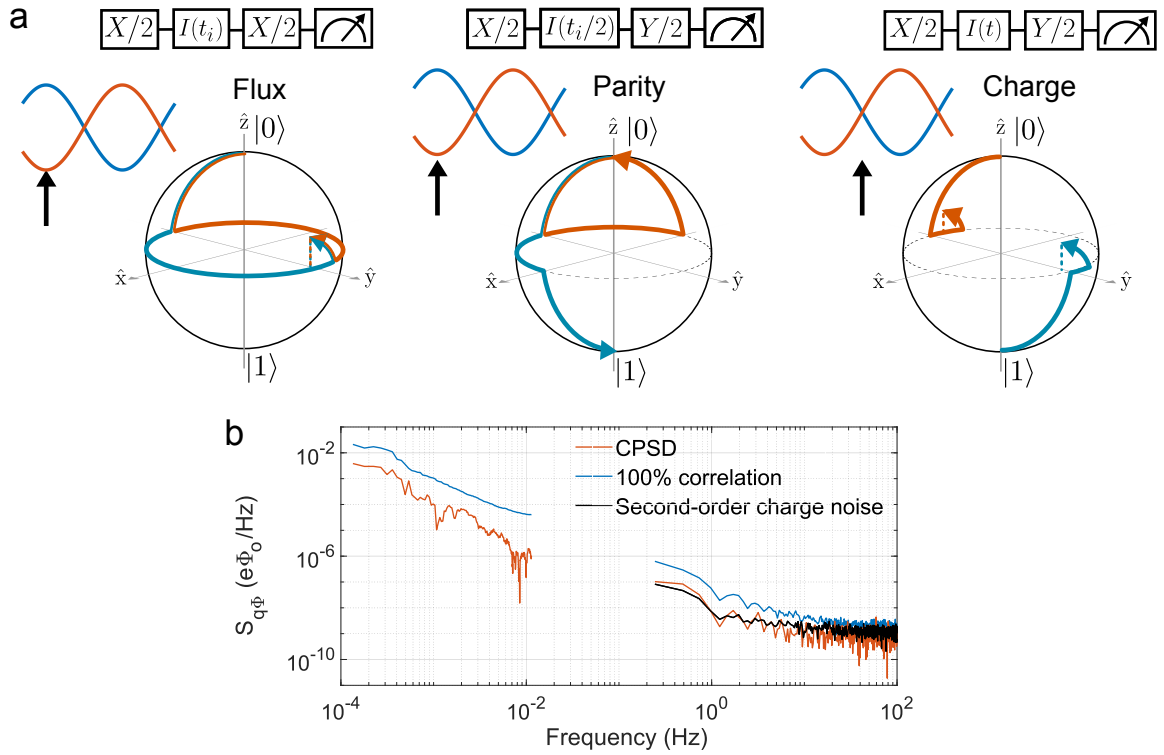

Figure 4.3: **Charge-flux correlation.** (**a**) Pulse sequence for the high-bandwidth measurement of the charge-flux CPSD $S_q\Phi$. The qubit is biased to a charge-insensitive, flux-sensitive point. A broadband $X/2$ gate followed by an appropriate idle time maps the two QP parity states to the same point on the equator of the Bloch sphere; a final $Y/2$ gate maps the accumulated phase to qubit population. Following the flux measurement, we de-populate the readout cavity and immediately follow the measurement with the same QP parity / charge sequence described in the previous chapter (Fig. 3a), with the charge noise measurement now conditioned on the flux noise measurement to account for the initial qubit state. (**b**) Cross power spectral density of charge and flux. The blue curve is the geometric mean of the direct spectra S_q and S_Φ, the orange curve is the charge-flux CPSD $S_{q\Phi}$, and the black curve is the noise floor set by the CPSD between second-order charge noise and charge noise. The low-frequency spectra are derived from interleaved time series of fluctuating offset charge (from measurements of the type described in Fig. 2) and offset flux (from a standard Ramsey experiment). We average 250 spectra acquired at a rate of 5×10^{-3} Hz, resulting in a noise floor of $S_{q\Phi}/\left(S_q S_\Phi\right)^{1/2} = 0.06$. The high-bandwidth measurement of charge-flux CPSD is dominated by second-order charge noise due to large random jumps in offset charge (black trace).

of experiments on qubit A to probe charge-flux correlations, as observation of such correlations could be used to constrain possible microscopic models. Here we describe these measurements, which allow us to place an upper bound on the level of correlation between charge and flux fluctuators.

The measurement protocol involves interleaved single-shot Ramsey sequences executed at appropriate bias points in flux and charge space that provide access to flux noise, QP parity, and charge noise. The high-bandwidth flux noise measurement is performed at a charge bias that yields zero first-order sensitivity to charge noise and maximal sensitivity to QP parity, as shown in Fig. 4.3a. The idle time is fixed so that both parity bands are mapped to the same final qubit state. Since the experiment is conducted away from the upper flux sweet spot in order to achieve sensitivity to flux fluctuations, E_J/E_C is reduced from its maximum value, resulting in a larger charge dispersion and a shorter idle time for the Ramsey-based flux noise measurements. By computing the cross power spectral density (CPSD) of single-shot flux and charge tomography scans, we probe correlations between flux and charge noise in the band from 2×10^{-1} Hz to 100 Hz.

A low-frequency cross spectrum is taken by interleaving the offset charge measurement with a low-bandwidth measurement of the flux. This can be achieved by performing a standard Ramsey measurement at a flux-sensitive bias to determine the qubit free precession frequency and using the transfer function $d\omega_{10}/d\Phi$ to extract the

fluctuating bias flux. The Ramsey measurement is done with a fixed idle time (set by the frequency separation of the parity bands) and a varying phase of the final gate. Fitting the resulting Ramsey measurement then gives an estimate of the flux deviation. From the separate charge and flux time series we compute the CPSD of charge and flux noise.

In Fig. 4.3b we combine the low- and high-bandwidth charge-flux CPSD in a single plot. To understand the strength of the correlation, it is informative to compare the cross spectrum $S_{q\Phi}$ with the geometric mean of the direct charge and flux spectra $(S_q S_\Phi)^{1/2}$. For maximally correlated noises, the magnitude of the CPSD will equal this quantity, with a well-defined phase across the spectrum. Note, however, that two uncorrelated time series will also have a CPSD with a magnitude equal to the geometric mean of the direct spectra, although in this case the phases of the cross spectrum will be random. As the magnitude of the sum of N random phasors scales as $\sqrt{N}$, the noise floor $S_{q\Phi}/\left(S_q S_\Phi\right)^{1/2}$ is then set by $1/\sqrt{N}$, where N is the number of averages per data point. For the low-bandwidth measurement, we average 250 spectra at a data rate of 5×10^{-3} Hz, corresponding to 36 hours of measurement, setting the noise floor $S_{q\Phi}/\left(S_q S_\Phi\right)^{1/2}$ at 0.06. Indeed, the upper bound on charge-flux correlation achieved around 10^{-2} Hz matches well with this noise floor set by finite averaging.

The high-bandwidth measurement protocol involves a much higher repetition rate of 10 kHz, so that finite averaging is not an issue. However, in contrast to the low-

bandwidth schemes that allow direct monitoring of charge and flux, the fast single-shot protocol monitors the accumulation of spurious phase, and we rely on known transfer functions to map this phase to fluctuating charge and flux. The flux measurement is executed at a point where we are first-order insensitive to charge noise (and *vice versa*); however, the second-order sensitivity to charge noise at the charge sweet spot is non-negligible. Indeed, by performing a check experiment at a bias point that is insensitive to first order to both charge and flux noise, we find that the noise floor in our charge-flux CPSD is set by second-order charge noise (black trace in Fig. 4.3b), putting an upper bound on charge-flux correlation at 1 Hz at the level of 0.1.

4.6 Charge noise dependence on device scale

As mentioned in the previous chapter, finding the dependence of charge noise on device geometry can help elucidate the the microscopic physics governing the observed anomalous $1/f^2$ charge noise. With this goal, we measure weakly-charge-sensitive transmon qubits at four different scales, as shown in Fig. 4.4. Each geometry has been designed to have the same qubit parameters (E_J, E_C, coupling capacitances), but the different scales allow for comparison between measured charge noise and island area, perimeter, etc. This data is summarized in Table 4.1 for six qubits across two die.

The data shows an increasing noise amplitude with increasing device size. However, the noise amplitude scales much more slowly than the scaling of the qubit island area,

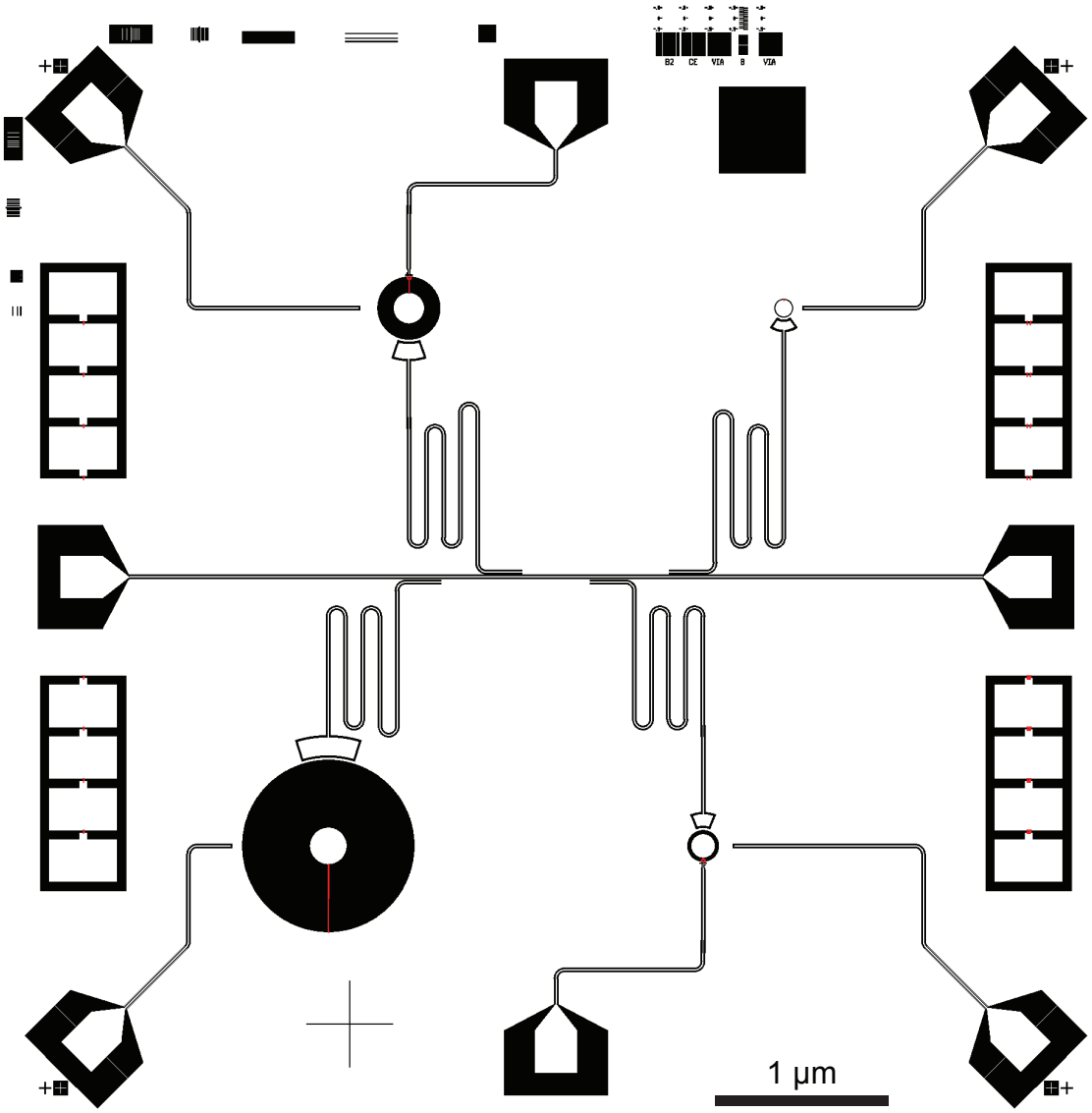

Figure 4.4: **Chip with multiple qubit geometries.** Chip design with four circular weakly-charge-sensitive transmon qubits, each capacitively coupled to a readout resonator. The readout resonators are each inductively coupled to a common feedline. Separate charge-bias lines are coupled to each qubit island with $\tilde{1}00$ aF capacitance, and two of the qubits have a flux bias line as well (coming in from the top and bottom). Etched area is in black, with junctions shown in red. The qubits have dimensions $\{r_i,r_o\}$=$\{50,53\}$,$\{70,90.5\}$,$\{90,182\}$,$\{108,500\}$ μm.

indicating patch potentials are not the source of the noise. It also scales much more slowly than the scaling of the etched area, suggesting the noise is not caused by a stream of charged particles impinging the area between the qubit island and ground plane. More detailed surface simulations like those shown in Fig. 3.4 coincidentally match our measured histogram for that device geometry, but cannot explain the scaling seen across the multiple geometries measured here.

As it turns out, an event with a large spatial footprint can soften the scaling of the expected noise amplitude. Events with large spatial footprints indicate a possibility for correlated errors. This will be the focus of the next two chapters, where we show that this anomalous charge noise derives from high energy particle impacts with the chip substrate and does indeed lead to correlated errors.

r_i	r_o	$S_q(10^{-3}$ Hz)	α	Σ(H(0.1:0.5))	$\Gamma_{\mathrm{QP}}/2\pi$
50^1	53	1	1.82	1.0(1)	1.0
70^1	90	1.12	1.77	1.6(1)	-
70^2	90	1.87	1.78	2.0(2)	4.0
90^1	182	2.86	1.77	2.0(3)	-
90^2	182	2.47	1.82	2.6(2)	53
108^2	500	4.26	1.85	2.8(3)	15

Table 4.1: **Scaling of charge noise with qubit geometry.** The device geometry is given by the inner radius r_i and outer radius r_o, each in μm, with the die index given as a superscript. The measured PSD parameters are given as an amplitude at $10^{-}3$ Hz and normalized to the value of qubit in the first line, which measured $S_q(10^{-3}\ \mathrm{Hz}) = 17.1\ \mathrm{e}^2/\mathrm{Hz}$. The noise exponent α does not seem to scale with geometry. An alternative way of measuring noise amplitude is to take the time-normalized sum of the number of jumps in the 0.1-0.5e range. This is shown in the fifth column, again normalized to the first row. The quasiparticle tunneling rates $\Gamma_{\mathrm{QP}}/2\pi$ were not relevant to the comparisons made here, but are given as an interesting aside, again normalized to the first qubit, which had a measured rate of 19.7 Hz

Chapter 5

Correlated charge noise and relaxation errors in superconducting qubits[1]

The central challenge in building a quantum computer is error correction. Unlike classical bits, which are susceptible to only one type of error, quantum bits ("qubits") are susceptible to two types of error, corresponding to flips of the qubit state about the X- and Z-directions. While the Heisenberg Uncertainty Principle precludes simultaneous monitoring of X- and Z-flips on a single qubit, it is possible to encode quantum information in large arrays of entangled qubits that enable accurate monitoring of all errors in the system, provided the error rate is low [56]. Another crucial requirement is that

[1] This chapter is a lightly edited and reformatted version of Ref. [95].

errors cannot be correlated. Here, we characterize a superconducting multiqubit circuit and find that charge fluctuations are highly correlated on a length scale over 600 μm; moreover, discrete charge jumps are accompanied by a strong transient suppression of qubit energy relaxation time across the millimeter-scale chip. The resulting correlated errors are explained in terms of the charging event and phonon-mediated quasiparticle poisoning associated with absorption of gamma rays and cosmic-ray muons in the qubit substrate. Robust quantum error correction will require the development of mitigation strategies to protect multiqubit arrays from correlated errors due to particle impacts.

The two-dimensional surface code is widely seen as a promising approach to realization of a fault-tolerant quantum computer based on superconducting integrated circuits [56]. In this architecture, quantum information is encoded in a two-dimensional fabric of superconducting qubits with nearest-neighbor connectivity. Provided that gate operations and measurements are performed above a certain *fault-tolerant threshold*, it is possible to uniquely identify and correct errors in the system by monitoring multiqubit parity operators of the form $XXXX$ and $ZZZZ$, where X and Z are single-qubit Pauli operators. In recent years, a number of groups have achieved beyond-threshold fidelities for single- and two-qubit gate operations [96, 97] and for qubit measurement [50, 98, 99], and steady improvements in performance are expected. The rigorous proof that it is possible, in principle, to achieve fault tolerance once threshold levels of fidelity are reached underpins much of the optimism for the surface code. However, this proof

rests on the assumption that errors across the multiqubit array are uncorrelated in both space and time. While it is possible to mitigate errors that are weakly correlated across neighboring qubits [57], quantum error correction will break down in the face of simultaneous errors that are correlated over large length scales.

In this article, we demonstrate spatially correlated charge fluctuations in a superconducting multiqubit chip over length scales of hundreds of microns, accompanied by correlated relaxation errors that extend over several millimeters. The data are compatible with absorption in the qubit substrate of cosmic-ray muons and γ-rays from background radioactivity. We perform detailed numerical modeling to determine the spatial profile of the charge burst associated with an absorption event; in addition, we present a simple model that describes the propagation of energy released by the event via scattering of pair-breaking phonons. These results have far-reaching implications for proposed error correction schemes such as the surface code that rely on large-scale arrays of qubits to monitor multiqubit stabilizers. A thorough understanding of the physics of particle impact events will be required to develop appropriate mitigation strategies and to engineer new approaches for fault-tolerant multiqubit arrays.

The sample geometry is shown in Fig. 5.1a-c. The 6.25×6.25 mm^2 chip incorporates four weakly charge-sensitive transmon qubits with a ratio of Josephson energy to single-electron charging energy $E_J/E_C = 24$; the detailed device parameters are presented in the next chapter. Each qubit comprises a circular superconducting Nb island with

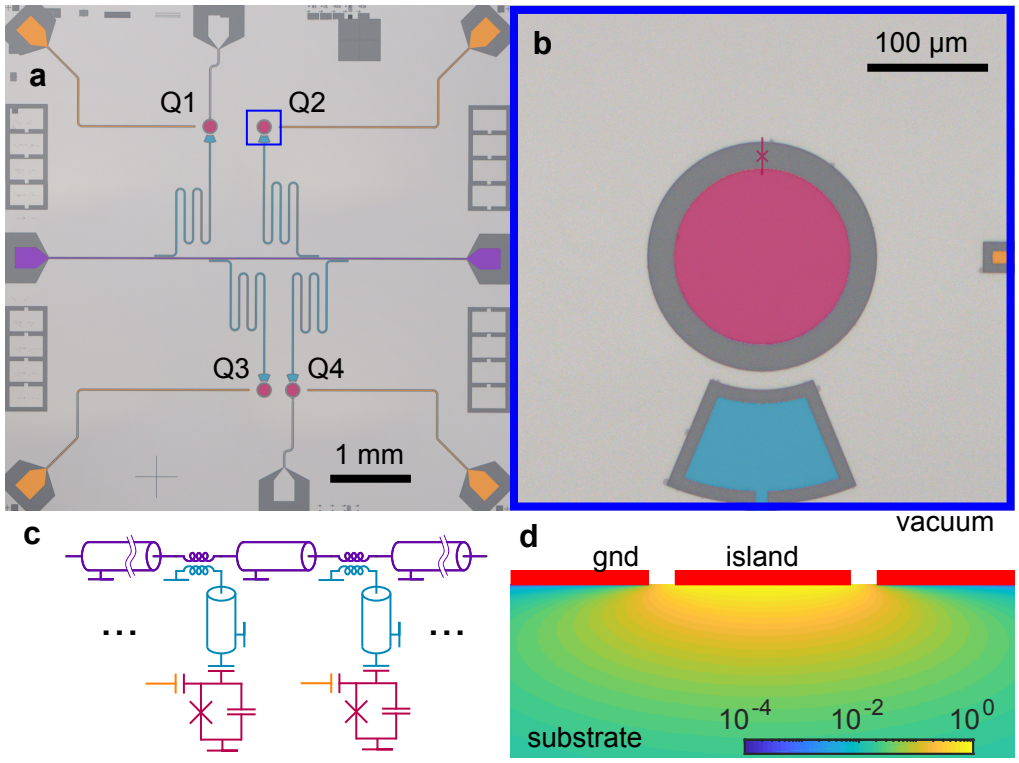

Figure 5.1: **Chip layout and charge response.** (**a**) Optical micrograph of the multiqubit chip. Four charge-sensitive transmon qubits (magenta) are coupled to local readout resonators (cyan) and charge gate lines (orange). The readout resonators are coupled to a common feedline (purple). (**b**) Closeup view of a single qubit. (**c**) Circuit diagram of the chip. Color coding matches the false coloring in parts (a) and (b). (**d**) Simulation of the charge induced on the qubit island from a unit point charge at various locations in the Si substrate.

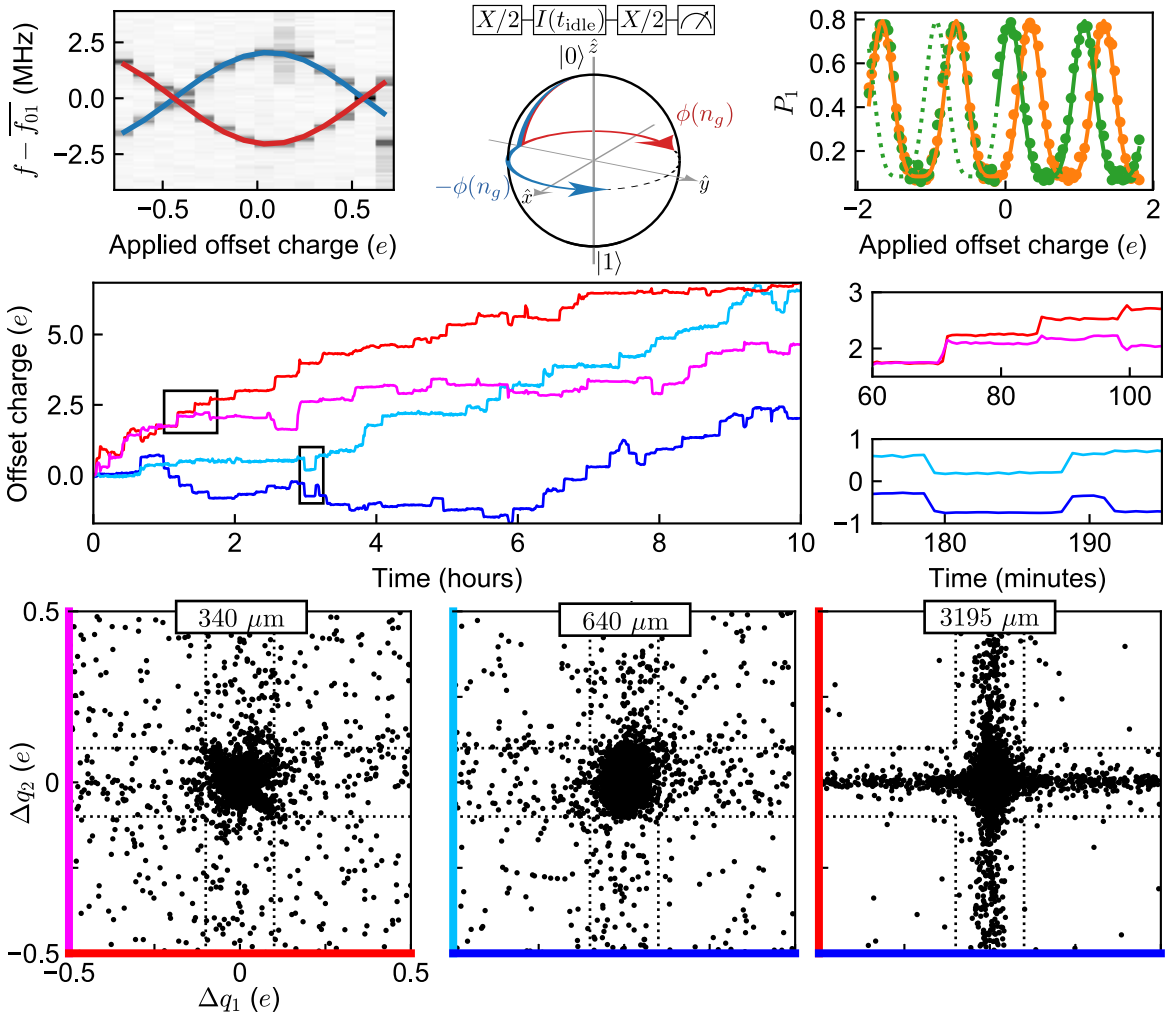

Figure 5.2: **Characterization of correlated charge fluctuations.** (**a**) Qubit spectroscopy *versus* applied offset charge showing the two quasiparticle parity bands; a discrete jump in offset charge can be seen in the rightmost column of data. (**b**) Ramsey sequence used to detect offset charge $n_g \equiv \Delta q/2e$, and trajectory of the qubit state vector for the two values of quasiparticle parity, following $\phi(n_g) = \Delta\omega_{01} t_{\text{idle}} \cos(2\pi n_g)$. (**c**) Two sequential scans of Ramsey amplitude *versus* offset charge; points are data and solid traces are theoretical fits. In the first scan (orange points), the offset charge was constant throughout the acquisition, while in the second scan (green points) a discrete jump in offset charge occurred during the scan. (**d**) Time series of offset charge on the four qubits measured simultaneously over 10 hours. Trace colors identify the locations of the four qubits, as shown in the figure inset. Panels to the right show detailed views of correlated offset charge jumps in qubit pairs. (**e**) Joint charge histograms measured on three qubit pairs; coloring of axes encodes the qubit location, and center-to-center separation is shown above the plots. Correlated charge fluctuations appear in the regions $|\Delta q| > 0.1e$ for both qubits in a pair.

radius $r_i = 70$ μm embedded in a circular cavity with radius $r_o = 90.5$ μm in the superconducting Nb groundplane. Two of the qubits are positioned on one side of the chip with a center-to-center separation of 340 μm, while two of the qubits are on the opposite side of the chip with 640 μm center-to-center separation. The qubit pairs are separated by around 3 mm. Each qubit is coupled to a local readout resonator that is in turn coupled to a common feedline.

For the purposes of interpreting the experiments described here, it is useful to consider the qubits as electrometers with a large effective sensing area for electric fields in the substrate. For our concentric qubit geometry, the sensing area for uniform electric fields is $\pi\epsilon r_i r_o$, where ϵ is the relative permittivity of the medium. In Fig. 5.1d we display the numerically computed offset charge on the qubit island induced by a unit point charge at various locations in the substrate; for an applied unit charge, the induced offset charge is simply the fraction of electric field lines that terminate on the qubit island.

In a first series of experiments, we perform simultaneous Ramsey tomography on the four qubits to generate time series of fluctuating offset charge. In Fig. 5.2a we show representative qubit spectroscopy and in Fig. 5.2b we show the experimental pulse sequence for the charge measurements [58]. The Ramsey $X/2 - Idle - X/2$ sequence maps precession frequency to occupation of the qubit $|1\rangle$ state irrespective of the quasiparticle parity of the qubit island. We perform a series of such experiments

for different applied gate charge as shown in Fig. 5.2c; the phase of the resulting curve reveals the offset charge on the qubit island. Note that this approach only allows measurement of offset charge modulo the fundamental charge e; large discrete jumps in offset charge will be aliased to the interval from -0.5e to +0.5e.

In Fig. 5.2d, we show a typical time series of offset charge measured on the four qubits simultaneously. The Ramsey-based charge measurement involves 3000 projections of the qubits across 10 applied gate charges, with a total cycle time of 44 seconds. Focusing on large discrete changes Δq in offset charge in the range $0.1e < |\Delta q| \leq 0.5e$, we find a rate of charge jumps of 1.35(3) mHz averaged over the four qubits. The right panel shows the detailed structure of the charge traces for nearest-neighbor pairs measured at shorter timescales. We observe numerous simultaneous discrete jumps in the offset charge of neighboring qubits. In Fig. 5.2e we show joint histograms of charge jumps measured in various qubit pairs. For all qubits, there is a Gaussian peak at the center of the distribution due to experimental uncertainty in the reconstructed offset charge. For the pairs separated by 340 and 640 μm, however, we find many simultaneous discrete changes in offset charge. Again focusing on large charge jumps in the range $0.1e < |\Delta q| \leq 0.5e$ and correcting for random coincidence, we find a correlation probability of 54(4)% for the qubit pair separated by 340 μm and a correlation probability of 46(4)% for the qubit pair separated by 640 μm (see chapter 6). For qubits on opposite sides of the chip with separation of order 3 mm, the rate of simultaneous

charge jumps is consistent with random coincidence.

As mentioned above, the characteristic length $\sqrt{r_i r_o}$ sets the scale over which charge is sensed in the bulk substrate. The high degree of correlation in charge fluctuations sensed by qubits with 640 μm separation indicates charging events with a large spatial footprint. There are two obvious candidates for such events: absorption of cosmic-ray muons in the qubit substrate and absorption of γ-rays from background radioactivity [100]. These events deposit energy of order 100 keV in the qubit substrate, roughly ten orders of magnitude greater than the $\sim$10 μeV energy scale of the qubit states. In both cases, the absorption event liberates charge in the substrate; a significant fraction of the free charge diffuses over hundreds of microns, leading to a large spatial footprint for the charging event that can be sensed by multiple qubits.

We perform detailed numerical modeling of charge bursts induced by the absorption of cosmic rays and background radioactivity. We use the GEANT4 toolkit [101–103] to calculate the energy deposited in the Si substrate. A simplified model of the cryostat (including vacuum can, radiation shields, stage plates, etc.) is used to calculate the flux of muons and γ-rays at the chip (see chapter 6). The angular and energy distribution of simulated muons reproduces measurements of cosmic ray muons at sea level [104], and the photons from background radioactivity are generated isotropically according to the measured energy distribution of γ-rays from environmental radioactivity (see chapter 6).

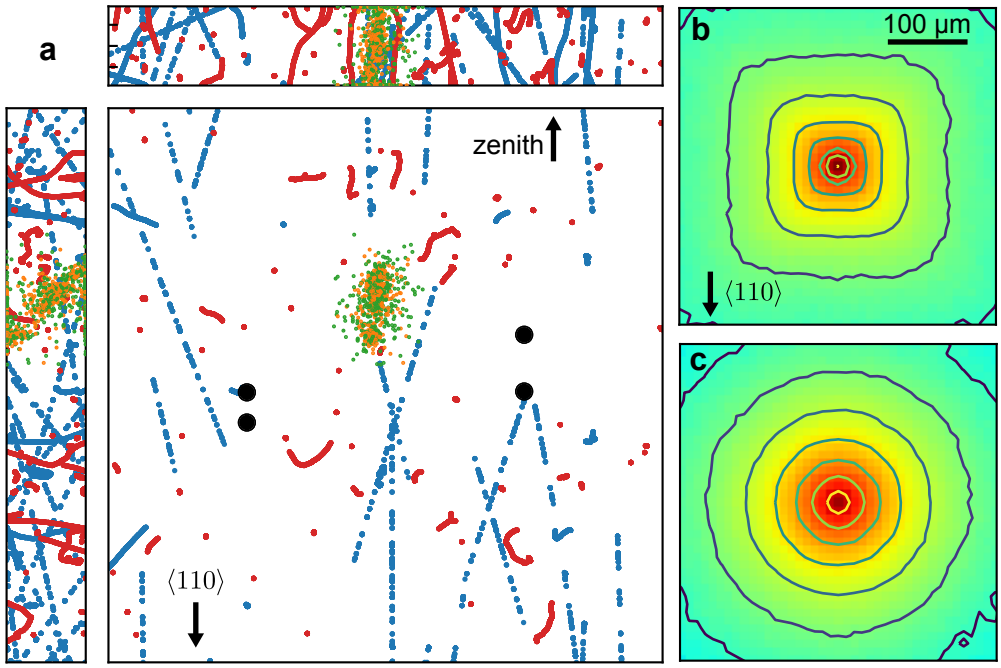

Figure 5.3: **Modeling of muon and γ-ray impacts.** (**a**) Top and side views of muon (blue, 30 events) and γ-ray (red, 60 events) tracks for a collection of simulated impact events in the 6.25×6.25 mm^2 chip. For a single muon track, a sample distribution of generated electrons (green) and holes (orange) is shown. Qubit locations are indicated by black circles. The crystal orientation of the Si substrate is $\langle 001 \rangle$; the crystal $\langle 110 \rangle$ direction is as indicated. The chip is oriented within the cryostat as indicated (orientation is relevant for the simulation of cosmic ray muons, which predominantly arrive from the vertical direction). Electron (**b**) and hole (**c**) probability distributions used to simulate induced offset charge. Electrons tend to travel along the crystal valleys, while the distribution of holes is spherically symmetric.

Each energy deposit liberates one electron-hole pair per 3.6 eV of energy transferred to the substrate [105]. The subsequent diffusion of charge is modeled using G4CMP [106, 107]. This charge transport simulation takes into account anisotropy in the electron band structure, which leads to a separation of the positive and negative charge liberated by the burst event, as demonstrated in Ref. [108]. The characteristic trapping length λ_{trap} is taken to be energy- and species-independent; λ_{trap} and the charge production efficiency f_q are tuned to match the experimentally measured charge histograms (see chapter 6 for details). We find for $\lambda_{\text{trap}} = 300$ μm and $f_q = 0.2$ that the simulated single- and two-qubit charge histograms are in good qualitative agreement with the measured histograms and provide a reasonable quantitative match with the correlation probabilities and charge asymmetries extracted from the data. The trapping length λ_{trap} is a critical materials parameter that determines the electrostatic coupling of particle impact events to nearby qubits. Based on our analysis, we infer a rate of γ impacts on the 6.25×6.25 mm^2 chip of 19.8(5) mHz; the contribution of cosmic ray muons to the measured rate of charge bursts is around 40 times smaller (see chapter 6). A separate measurement of environmental radioactivity in the laboratory using a NaI scintillation counter yields an inferred rate of γ impacts on the qubit chip of 9 mHz. The factor of two discrepancy could indicate a local source of radioactive contamination within the cryostat.

Ultimately, the energy released by particle absorption will be transferred to the

phonon reservoir in the qubit susbtrate. Phonons will rapidly scatter to the gap edge of the Nb groundplane by breaking Cooper pairs; nonequilibrium quasiparticles in the vicinity of the Al junction leads are expected to become trapped and suppress qubit relaxation time T_1 [80, 81, 109–112]. In a separate series of experiments, we use one qubit as a trigger for charge bursts while additional qubits are used as local probes of T_1. Fig. 5.4a shows the pulse sequence for the experiment. On qubit 1 (Q1) we perform the same charge Ramsey sequence as in Fig. 5.2, while on qubits 2 and 4 (Q2, Q4) we perform a stripped-down inversion recovery experiment consisting of a premeasurement to initialize the qubit, an X-gate, a fixed idle time of 10 μs, and a second measurement. The sequence is repeated continuously with a cycle time of 40 μs.

We identify burst events when there is a large discrete change in the running average of the Ramsey amplitude measured on Q1, allowing us to align and average traces from the probe qubits. In the absence of burst events, the inversion recovery sequence yields average occupations of the qubit $|1\rangle$ state that are consistent with the separately measured qubit T_1 times. When a charge burst is detected in Q1, however, we find a clear suppression in the $|1\rangle$ occupation of Q2 and Q4. Fitting this dropout with an exponential recovery convolved with a Gaussian to account for timing uncertainty in the trigger, we find a recovery timescale of 130 ± 40 μs. We conclude that the same process that gives rise to discrete jumps in offset charge also leads to correlated suppression of qubit T_1 time over length scales in excess of 3 mm. In general, quasiparticles that

trap in the junction leads in the immediate aftermath of a particle impact event will induce both upward and downward qubit transitions [54] that will be correlated across the qubit array.

The recovery timescale for quasiparticle poisoning can be understood in the following way. Phonons propagate diffusively to the boundary of the chip in a time $x_0^2/c_s z_0$, where $x_0 = 6.25$ mm is the lateral dimension of the chip, $c_s = 6 \times 10^3$ m/s is the sound speed in the Si substrate, and $z_0 = 375$ μm is the chip thickness. The chip is thermally anchored at four corners, with a fraction $\beta = 0.2$ of the chip perimeter acoustically coupled to the chip enclosure. We therefore find a characteristic dwell time for athermal phonons in the substrate of order $x_0^2/\beta c_s z_0 \sim 100$ μs, in qualitative agreement with the measured recovery time.

We briefly discuss the implications of these results for the realization of fault-tolerant superconducting qubit arrays in the surface code; for a detailed discussion, see chapter 6. We define correlation degree m as the number of qubits in a line to which an error couples. It can be shown that the fault-tolerant threshold p_m for correlated errors of degree m is given by $p_m \approx p^m$, where p is the fault-tolerant threshold for uncorrelated errors [57]. The relaxation (bit-flip) errors associated with phonon-mediated quasiparticle poisoning are particularly damaging, as they couple to all qubits in a mm-scale chip. We identify two additional correlated error mechanisms: correlated phase-flip errors due to exponentially small (but nonzero) frequency shifts induced by correlated

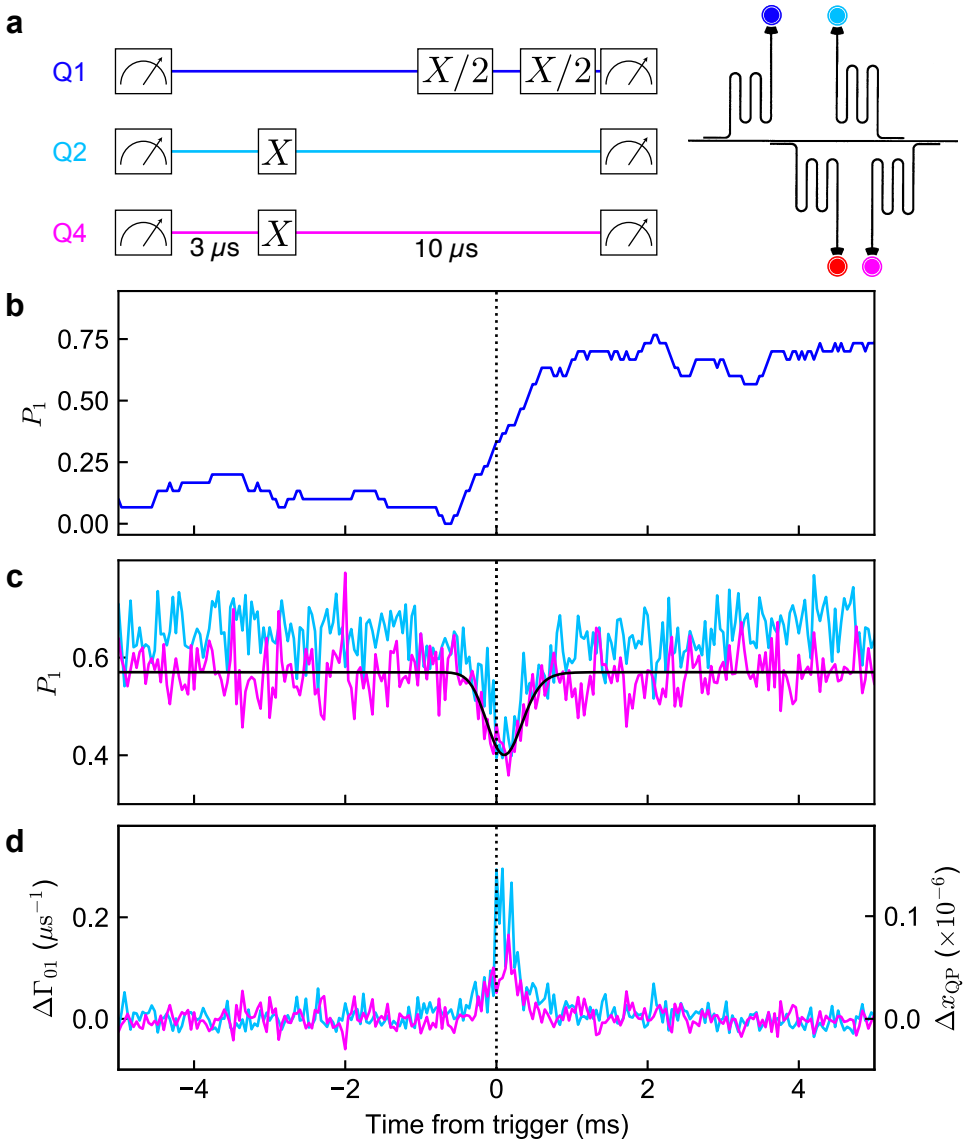

Figure 5.4: **Characterization of correlated relaxation errors.** (**a**) Experimental pulse sequence. Qubit 1 (Q1) acts as a charge trigger, while qubits 2 and 4 (Q2, Q4) act as local probes of T_1. (**b**) Representative trace of the Ramsey amplitude of Q1 during a burst event; qubit occupation is a moving average of 30 single-shot projections of the qubit state. (**c**) Average single-shot occupation for Q2 (blue, 340 μm from Q1; 142 events) and Q4 (pink, 3 mm from Q1; 121 events) *versus* time with respect to a detected charge burst. Black trace is a fit to the data from Q4, yielding a recovery timescale 130±40 μs. (**d**) Average change $\Delta\Gamma_{01}$ in qubit relaxation rate and average change Δx_{QP} in reduced quasiparticle density calculated from the data in (c).

charge noise, and correlated bit-flip errors induced by the sudden charge transient associated with particle impact. Even for a nominally charge-insensitive qubit such as the transmon with $E_C/h = 250$ MHz and $E_J/E_C = 50$, we find that the rate of correlated phase-flip errors is significant, with 0.9% (3.8%) of γ-ray (muon) impacts giving rise to correlated phase-flip errors above the 10^{-4} level in qubit pairs separated by 640 μm, and with 7.2% of muon impacts giving rise to correlated phase-flip errors above the 10^{-6} level in qubit pairs separated by 3 mm. In general, the exponential sensitivity of the qubit array to correlated errors represents a serious design constraint: for a given error mechanism with fixed spatial footprint, the need to protect against correlated errors will dictate how closely spaced the qubits can be.

A clear understanding of the underlying physics of particle impact events in the qubit substrate will allow the development of mitigation strategies to suppress or even eliminate correlated errors. We discuss several possible approaches below.

First, one can operate the quantum processor in a clean environment that provides shielding against cosmic ray muons and background γ-rays. Such measures are routinely taken in ultrasensitive searches for rare events, such as neutrinoless double beta decay [113, 114] or dark matter interactions [115, 116]. Underground sites enable the reduction of cosmic-ray muon flux to negligible levels [117–119]. Similarly, the cryostat can be shielded in massive lead and copper structures to absorb γ-rays. A few centimeters of lead shielding guarantees a suppression of the γ flux by 1-2 orders of magnitude.

Finally, the materials used to construct the device and its enclosure can be selected to be radio-pure and processed through electrochemical treatments that remove surface contamination [120–124].

Second, one could reduce the sensitivity of the qubit to the burst events. Reduction of the size of the qubit island and reduction of the gap from the island to ground will limit the sensitivity of the qubit to electric fields in the substrate. It is important to note that the near-continuous groundplane in the geometry studied here provides excellent electrostatic screening against charge in the bulk. We anticipate that a multiqubit architecture that lacks a groundplane will be much more susceptible to correlated phase-flip errors induced by charge bursts.

In order to combat quasiparticle-induced T_1 suppression, mitigation strategies could be adopted to prevent the direct diffusion of quasiparticles, for example involving superconducting bandgap engineering [125] or normal-metal quasiparticle traps [126, 127]. Finally, steps could be taken to promote the relaxation of high-energy phonons below the gap edge and to enhance the rate of removal of phonons from the qubit substrate [128]. Modest improvements in the acoustic anchoring of the substrate could accelerate recovery of the chip following particle absorption, minimizing correlated relaxation errors due to quasiparticles.

Chapter 6

Supplementary information for "Correlated charge noise and relaxation errors in superconducting qubits"[1]

6.1 Device fabrication

Our devices are fabricated in a single-layer process on high-resistivity (>10 kΩ cm) Si(001) wafers. Following a hydrofluoric acid strip of the native SiO_x, we sputter a 90-nm film of Nb at a rate of 45 nm/min. We cap this film *in situ* with a 20-nm layer of Al

[1] This chapter is a lightly edited and reformatted version of Ref. [95].

	Quantity	Q1	Q2	Q3	Q4	Units
$g/2\pi$	Designed qubit-resonator coupling			27		MHz
κ	Designed decay rate of readout resonators			295		ns^{-1}
f_{01}	Mean qubit transition frequency	4.5641	4.4330	4.2939	4.3973	GHz
f_r	Measured frequency of readout mode	6.195	5.835	6.082	5.966	GHz
$2\Delta f_{01}$	Measured pk-pk charge dispersion	4.1	5.3	7.2	6.3	MHz
$\eta/2\pi$	Measured qubit anharmonicity	435	434	430	–	MHz

Table 6.1: **Parameters of devices used in the experiments.**

grown at a rate of 8 nm/min. The Nb deposition parameters are tuned to yield films with slight compressive stress. We use an i-line projection aligner to define the qubit islands and all readout and control structures, and we etch the metal using a Cl_2/BCl_3 recipe in an inductively coupled plasma reactive ion etch tool. The qubit junctions are realized using a standard Dolan bridge process [129]. We pattern the MMA/PMMA stack with a 100-keV electron-beam writer. We shadow evaporate the Al-AlO_x-Al stack in an electron-beam evaporation tool with base pressure 1×10^{-8} Torr; prior to junction growth we perform an ion mill clean of the substrate to ensure good metallic contact to the base metal layer.

6.2 Circuit parameters

In Table 6.1, we list the designed and measured parameters of the devices used in these experiments.

6.3 Measurement setup

Our measurement setup is shown in Fig. 6.1. We use a standard microwave heterodyne setup involving single-sideband modulation of a local oscillator for both qubit and resonator drive. Each microwave control line passes through multiple stages of filtering and attenuation at the 4 K and mK plates of the dilution refrigerator, including low-pass Eccosorb filters with a cutoff at 20 GHz. Quasistatic charge bias lines pass through lower-frequency Eccosorb filters with a cutoff at 300 MHz. For the measurements described in Fig. 5.4, readout signals are preamplified by a traveling-wave parametric amplifier (TWPA) at the mK stage followed by a high electron mobility transistor (HEMT) amplifier at the 4 K stage. The TWPA requires a separate microwave pump tone and can be switched in and out of the readout chain by a pair of microwave coaxial relays (not shown).

6.4 T_1 dropout

We fit the T_1 dropout data of Fig. 5.4 with an exponential recovery convolved with a Gaussian to account for timing imprecision of our Ramsey-based charge trigger. We use the fit function

$$P_1(t) = \frac{1}{2} \exp\left(\frac{\sigma^2 - 2\tau t}{2\tau^2}\right) \operatorname{erfc}\left(\frac{\sigma^2 - \tau t}{\sqrt{2}\sigma\tau}\right) \tag{6.1}$$

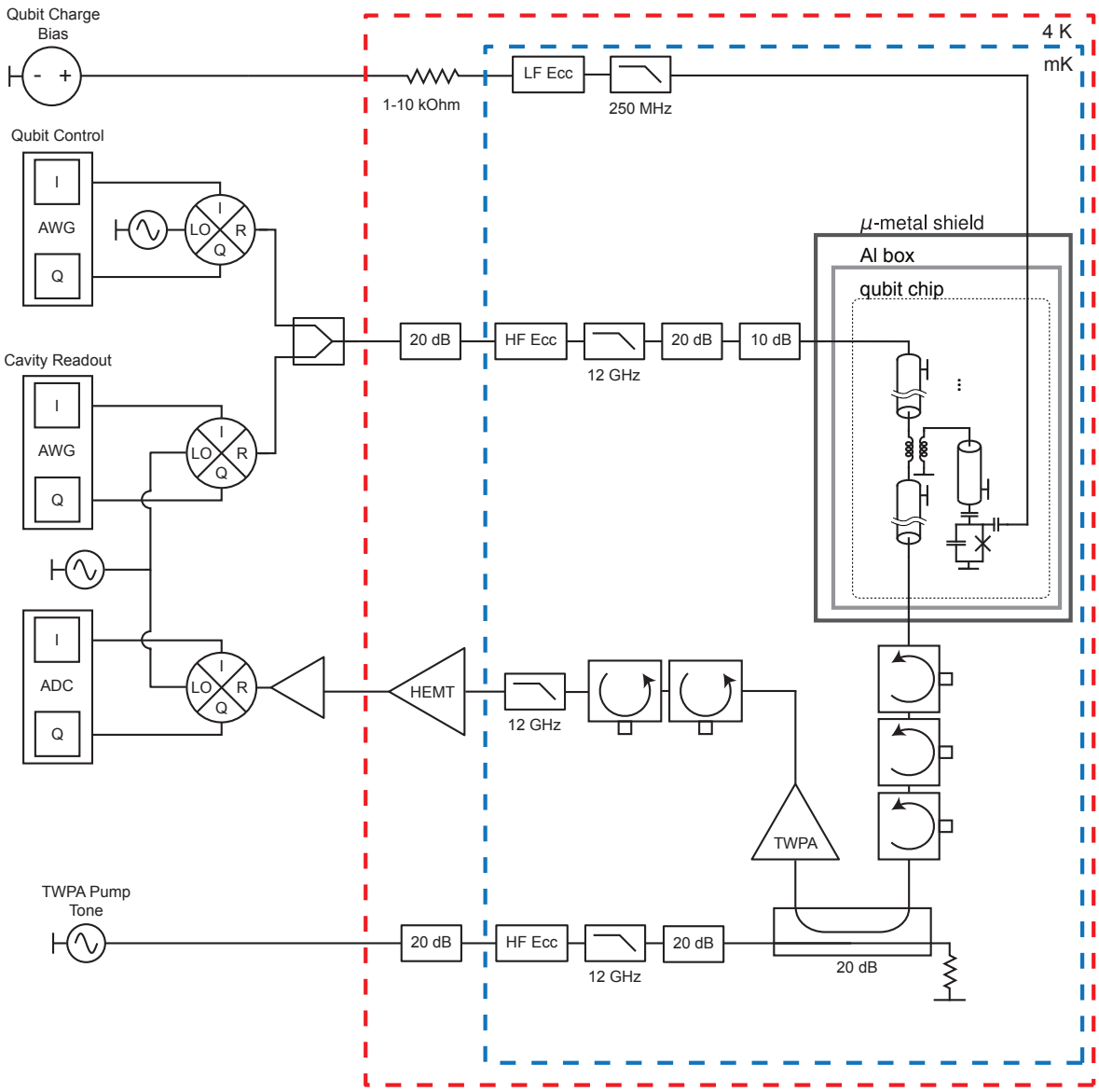

Figure 6.1: **Wiring diagram of the experiments.**

to extract the characteristic recovery time τ, where t is the elapsed time from the charge trigger and σ is the standard deviation of the Gaussian. A fit to the data of Fig. 5.4c yields a recovery time of $\tau = 130 \pm 40$ μs and a timing jitter $\sigma = 210 \pm 30$ μs.

We ascribe the average suppression in P_1 to an enhanced qubit relaxation rate $\Delta\Gamma_{01}$ due to quasiparticle poisoning. To convert the average change in relaxation rate to an increased density of nonequilibrium quasiparticles, we use the expression [112]

$$\Delta\Gamma_{01} = \frac{x_{\mathrm{QP}}}{\pi}\sqrt{\frac{2\Delta}{\hbar}\omega_{01}}, \tag{6.2}$$

where x_{QP} is the reduced density of quasiparticles (i.e., density of quasiparticles n_{QP} relative to the Cooper pair density n_{CP}; for Al, $n_{\mathrm{CP}} = 4\times10^6$ $\mu\mathrm{m}^{-3}$) and $2\Delta/e = 380$ μV is the superconducting gap of Al.

6.5 Correlation probabilities and event rates

It is necessary to differentiate true correlated charging events in which a single charge burst is sensed by multiple qubits from apparent correlations that arise from our finite sampling rate. We label two qubits A and B; we define p_A^{obs} (p_B^{obs}) as the probability that a large discrete charge jump is registered in a given 44-second measurement cycle on qubit A (qubit B), while p_{AB}^{obs} is the probability that we observe a jump in both qubits. The events that are seen by qubit A have two contributions: some of these events are due to charge bursts that couple to both qubits (occurring with probability

p_{AB}), while some are due to events that are seen only by qubit A (occurring with probability p_A). We thus have

$$p_A^{\text{obs}} = p_{AB} + p_A(1 - p_{AB}), \tag{6.3}$$

and similarly for p_B^{obs}. In the same way, there are two contributions to p_{AB}^{obs}: one contribution from burst events that couple to both qubits simultaneously (again, occurring with probability p_{AB}), and one contribution from random coincidence, where independent charging events, each seen by only one of the qubits, occur during the same measurement cycle. We have

$$p_{AB}^{\text{obs}} = p_{AB} + p_A p_B(1 - p_{AB}). \tag{6.4}$$

Solving for the probability of true correlated events in terms of the observed probabilities, we find

$$p_{AB} = \frac{p_{AB}^{\text{obs}} - p_A^{\text{obs}} p_B^{\text{obs}}}{1 + p_{AB}^{\text{obs}} - (p_A^{\text{obs}} + p_B^{\text{obs}})}. \tag{6.5}$$

In Table 6.2 we list the observed (p_i^{obs}, p_{ij}^{obs}) and inferred (p_i, p_{ij}) probabilities for discrete charge jumps per measurement cycle extracted from the dataset of Fig. 5.2; here the indices i, j specify the qubit or qubit pair.

We define correlation probability p_{AB}^{corr} as the ratio of the probability of a true correlated event to the average of the probabilities of observed events in qubits A and B:

$$p_{AB}^{\text{corr}} = \frac{2p_{AB}}{p_A^{\text{obs}} + p_B^{\text{obs}}}. \tag{6.6}$$

With this definition, p_{AB}^{corr} represents the probability that a large discrete offset charge jump seen by one qubit will also be seen by a neighboring qubit at a given separation. As we discuss below, comparison of simulated and measured values for p_{AB}^{corr} provides a means to pin down the charge trapping length scale and charge production efficiency associated with charge diffusion following an absorption event. We obtain correlation probabilities of 0.54(4) for Q3-Q4 (340 μm), 0.46(4) for Q1-Q2 (640 μm), and 0.00(1) for Q1-Q3 (3195 μm).

It is instructive to connect the observed rate of discrete charge jumps in the range $0.1e < |\Delta q| \leq 0.5e$ to an absolute rate of particle impacts on the qubit chip. In Table 6.2 we show the rates Γ_i^{obs} of large discrete jumps observed on each qubit along with the inferred rates of correlated jumps Γ_{ij} in the various qubit pairs. We find a rate of discrete charge jumps of 1.35(3) mHz averaged across the four qubits. From

Separation	Qubit(s)	$p_i^{\text{obs}}, p_{ij}^{\text{obs}}$	p_i, p_{ij}	$\Gamma_i^{\text{obs}}, \Gamma_{ij}$ (mHz)
-	Q1	0.055(2)	0.030(3)	1.27(5)
-	Q2	0.061(3)	0.035(4)	1.38(6)
-	Q3	0.060(3)	0.029(3)	1.38(6)
-	Q4	0.060(3)	0.029(4)	1.38(6)
340 μm	Q3-Q4	0.033(2)	0.033(2)	0.74(6)
640 μm	Q1-Q2	0.027(2)	0.026(2)	0.60(5)
3195 μm	Q1-Q3	0.004(1)	0.000(1)	0.00(2)

Table 6.2: **Probabilities and rates of impact for qubits and qubit pairs.**

the GEANT4 simulations, we expect an absolute rate of muon impacts on the chip of 0.5 mHz. Similarly, from the GEANT4 and charge transport simulations described below, we know that 16% of these muon events will lead to an aliased offset charge jump above the threshold of $0.1e$. We ascribe the remaining jump events to γ-ray absorption in the qubit substrate, with rate 1.27(3) mHz. Again using the results of the GEANT4 and charge transport simulations, we can map this rate of charge bursts seen by the individual qubits to a rate of γ impacts on the qubit chip. We find that the only 6% of γ-ray absorptions lead to an aliased offset charge jump above $0.1e$, implying the rate of γ impacts on the 6.25×6.25 mm^2 qubit chip is 19.8(5) mHz. Thus, if we we consider only the rate of impacts on the qubit chip, the contribution of environmental radioactivity is roughly a factor 40 larger than that of cosmic ray muons. However, as we show below, the muon impact events lead to stronger correlations across qubit devices.

6.6 Modeling of charge bursts

We use the GEANT4 software framework to model the absorption of energy in the qubit chip [101–103]. We consider a simplified model of the dilution refrigerator cryostat, including the vacuum can, nested radiation shields, copper stage plates and sample stage, and aluminum sample enclosure; see Fig. 6.2a-b. We focus on two contributions to the measured rate of charge bursts: γ-rays produced by environmental radioactivity

and cosmic-ray muons.

Environmental radioactivity is commonly ascribed to ^{40}K in addition to ^{232}Th and ^{238}U and their daughter nuclei. These contaminants are generally found throughout building materials, cryogenic infrastructure, and in the air itself. Their relative abundance and activity can vary from site to site. Nevertheless, the energy scale of interest is a few MeV, and the typical flux is of order 1 $\gamma/\mathrm{cm}^2/\mathrm{s}$. As input for the simulations, we use the spectrum of background radiation measured in Hall C of the Laboratori Nazionali del Gran Sasso (LNGS) in Italy; as we discuss in Section 6.10 below, this spectrum is comparable to that measured in the qubit laboratory in Madison apart from an overall reduction in the absolute rate by a factor 2.8, which does not impact the simulation results.

We generate 10^{10} γ-rays uniformly distributed on a cylindrical surface centred around the cryostat and record the track of each particle. Most γ-rays cross the setup without interacting, while a small fraction of γ-rays hit the qubit chip and produce an electron. Typical electron tracks produced by γ interactions are shown in Fig. 5.3. The spectrum of energy deposited by these electrons is shown in Fig. 6.2c. The spectrum extends to around 1 MeV with a mean energy deposit of 100 keV; the distribution of energy deposited in the substrate is insensitive to the detailed shape of the spectrum of incident γ-rays.

Cosmic-ray muons provide a subdominant contribution to the measured rate of par-

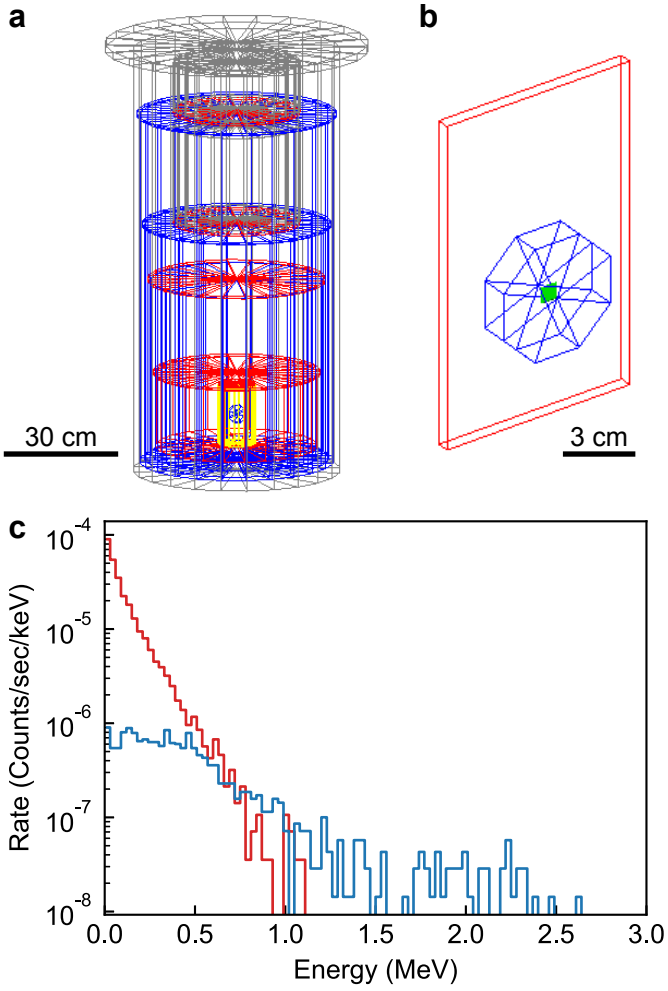

Figure 6.2: **GEANT4 modeling of the experiment.** (**a**) Model of the dilution refrigerator cryostat used in GEANT4 simulations of particle absorption events. (**b**) Model of the silicon chip, aluminum sample enclosure, and copper stage plate used in the simulations. The materials of the cryostat and chip enclosure include stainless steel (grey), copper (red), aluminum (blue), and cryoperm (yellow); the silicon chip is shown in green. (**c**) Energy deposited in the qubit substrate from environmental radioactivity (red) and cosmic ray muons (blue). The simulation of environmental radioactivity assumes a γ flux of $2.8\,\gamma/\mathrm{cm}^2/\mathrm{s}$. The γ-rays deposit an average energy of 100 keV, while the average energy deposited by muons and their secondary γ-rays is 460 keV.

ticle impacts. Muons release energy by ionization with a typical flux of $1\,\mu/\mathrm{cm}^2/\mathrm{min}$. We generate 10^8 muons on a flat surface above the cryostat using the energy distribution and angular distribution reported in Ref. [104]. We record the track of each muon; like γ-rays, the vast majority of muons cross the setup without interacting, while a small fraction hit the substrate, producing a continuous track that deposits a mean energy of 460 keV (see Fig. 5.3 and Fig. 6.2c). In some cases, the muons interact with the cryostat material, producing secondary γ-rays. The total rate of muon events in the substrate (primary + secondary γ events) is 0.5 mHz.

Using the tracks generated by GEANT4 as a starting point, we model the diffusion of electrons and holes in the qubit substrate. To construct the charge PDFs, we simulate 10^8 electron-hole pairs originating uniformly along a line in the z-direction in the Si substrate (the direction normal to the chip surface). The substrate thickness and crystal orientation are chosen to match the parameters of the qubit chip under test; namely, we take a thickness of 375 μm, and we take the $\langle 001 \rangle$ direction to be normal to the chip surface while the $\langle 110 \rangle$ and $\langle$1-10$\rangle$ directions are aligned with the chip edges. Each electron-hole pair is given 3.6 eV of initial total energy (2.6 eV of kinetic energy) and the momenta are randomized. In the case of electrons, randomization occurs in a spherically symmetric way before application of a Herring-Vogt transform to simulate the valley anisotropy [130]; the initial valley occupation is randomly chosen. The charges are then propagated and allowed to emit phonons. Charges diffuse until

they either trap (with a probability set by the trapping length λ_{trap}) or until they encounter a surface. Details on tuning of the scattering parameters for this simulation can be found in ref [108].

We then divide these simulations into bins by initial z-position using a bin width of 10 μm. For each of the initial z-positions, we compute the probability that the final charge position falls within a bin of width 10 μm in x and y and 3.71 μm in z at a given point in a three-dimensional grid the size of the chip under test; with this choice, each dimension has 101 total bins centered at the origin. This bin width allows the PDF to have a resolution much smaller than the lateral extent of the qubits, while the number of bins is large enough to ensure convergence at the tails of the distribution. This set of PDFs over the range of z-positions of the impact event is then used to generate final positions of the electrons and holes by random weighted choice.

Using the γ and muon tracks derived from the GEANT4 simulations and the charge distributions described above, we generate single- and two-qubit offset charge histograms for a range of values of the characteristic charge trapping length λ_{trap} and charge production efficiencies f_q. Here, f_q represents the fraction of free charge that avoids immediate recombination at the impact site. In the absence of an applied electric field, we expect $f_q < 1$ [131, 132]. To compare our simulations to the measured results, we consider three quantities derived from the charge histograms, described here in order of importance. The first, *correlation probability* (denoted p_{ij}^{corr} above),

is the probability that a discrete jump in offset charge that is registered by one qubit is also registered by its neighbor. Second, *charge asymmetry* is the number of large positive jumps in offset charge divided by the total number of large jumps, averaged over all four qubits. While in many cases the change in offset charge measured by the qubit is aliased to the interval from -0.5e to 0.5e, no aliasing will occur for a distant source of charge that induces a small change in offset charge $|\Delta q| < 0.5e$. We find in our measurements a clear excess of positive offset charge, corresponding to an excess of negative charge in the substrate near the qubit island. We understand the charge asymmetry to arise from the different ways that electrons and holes diffuse in the Si substrate, a consequence of Si valley physics (see discussion above). Finally, we examine *13/24 asymmetry*, the asymmetry in the rate of joint events in quadrants 1 and 3 as opposed to quadrants 2 and 4. We observe a clear excess of events in quadrants 1 and 3, corresponding to distant charge bursts that are not aliased and which couple more or less equally to the two qubits.

In Fig. 6.3, we show extracted values of correlation probability, charge asymmetry, and 13/24 asymmetry for simulations performed for a range of values of λ_{trap} and f_q for both γ-ray and muon events. For all simulated data, we have added Gaussian charge noise derived from the experimental uncertainties associated with Ramsey-based reconstruction of charge. The color scale is set such that white is a match to the value measured experimentally. As the rate of γ impacts on the chip exceeds the muon rate by

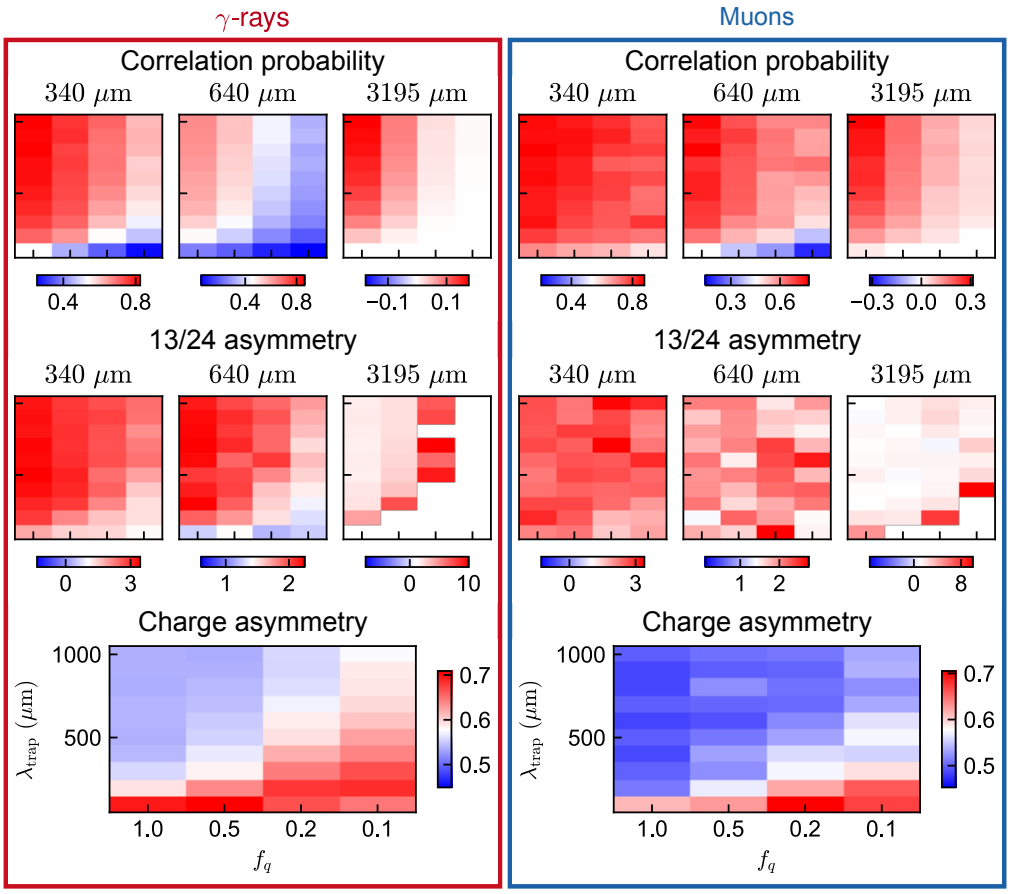

Figure 6.3: **Comparison of measured and simulated charge histograms.** Correlation probability, 13/24 asymmetry, and charge asymmetry for simulated joint and single-qubit charge histograms associated with γ-ray (left) and cosmic ray muon (right) absorption. For correlation probability and 13/24 asymmetry, results are derived from joint histograms calculated for qubits with separation 340 μm, 640 μm, and 3195 μm; for charge asymmetry, results are derived from simulated single-qubit charge histograms. The color scale is adjusted for each plot so that white matches the value derived from the experimentally measured charge histogram. For all plots, the vertical axis corresponds to charge trapping length λ_{trap} in the range from 100 μm to 1000 μm while the horizontal axis corresponds to charge production efficiency $f_q = 1.0, 0.5, 0.2,$ and 0.1; the axis labels and scales shown in the plots of charge asymmetry apply to all subplots of this figure. For comparison with measurement, we focus on the simulated histograms corresponding to γ-ray events, which account for over 97% of the impact events on the qubit chip. From these simulations, we find that the parameter choice $\lambda_{\text{trap}} = 300$ μm and $f_q = 0.2$ provides a good overall match to the experimentally measured data.

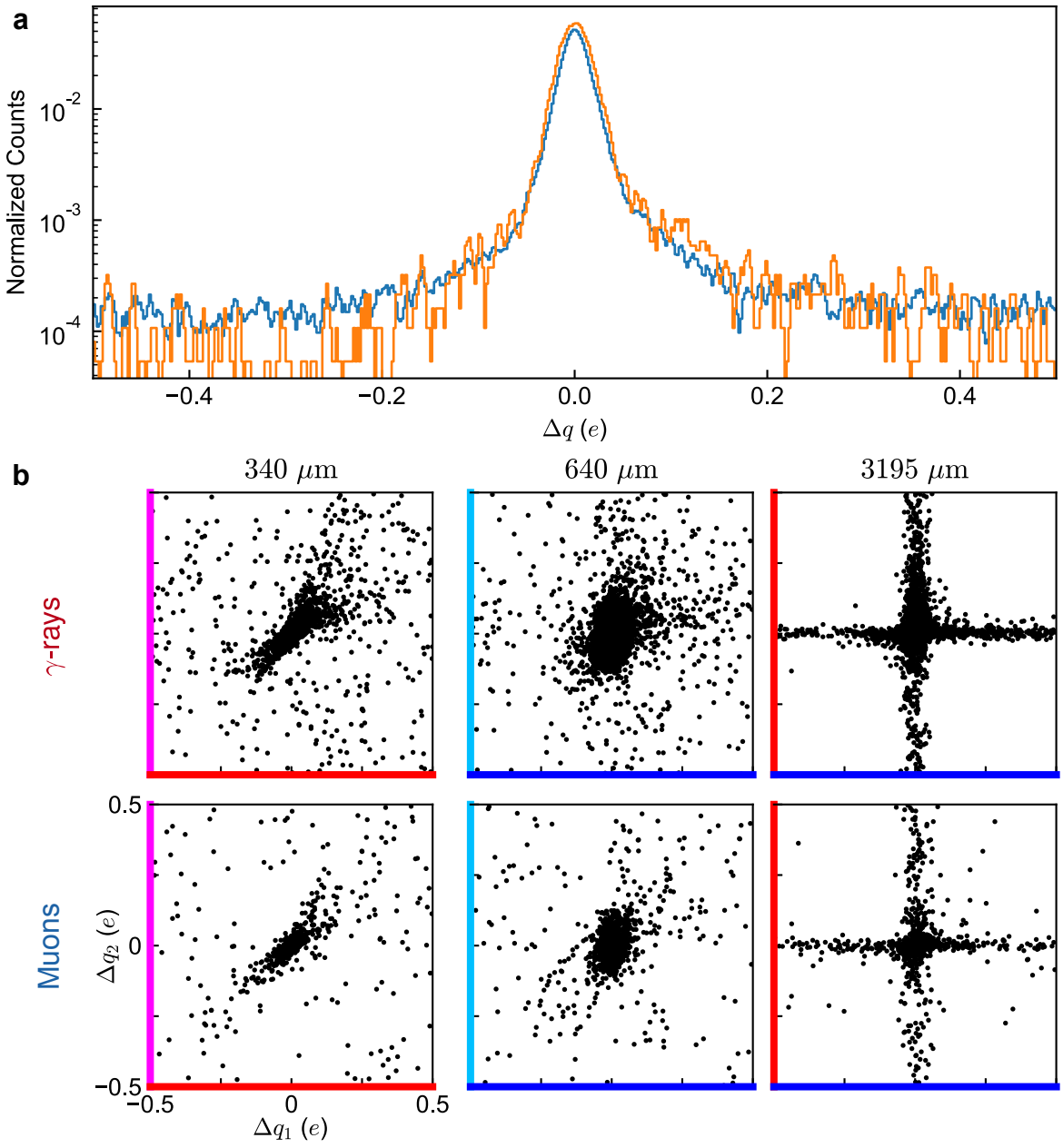

Figure 6.4: **Simulated histograms of charge jumps.** (**a**) Histogram of charge jumps on qubit 1. The experimentally measured data is shown in blue, while the simulated data is shown in orange. (**b**) Simulated joint charge histograms for the three qubit pairs studied in this work. The charge histograms from 7895 γ-ray events are shown in the top row, while the charge histograms from 1162 cosmic ray muon events are shown in the bottom row. All simulations were performed with $\lambda_{\text{trap}} = 300$ μm and $f_q = 0.2$ and include Gaussian charge noise comparable to that in the measurements.

roughly a factor 40, we focus on simulated γ-ray events for the purposes of comparison with the measured data. While simulations performed at large λ_{trap} and small f_q yield qualitatively similar results for correlation probability, charge asymmetry, and 13/24 asymmetry as simulations performed at small λ_{trap} and large f_q, the degeneracy with respect to the choice of parameters can be broken by examining the detailed shape of the single- and two-qubit charge histograms. We find that the parameter choice $\lambda_{\text{trap}} = 300$ μm and $f_q = 0.2$ provides the best overall agreement with the measured data. This implies a low mean charge collection, consistent with zero-field measurements in comparable crystals [132].

In Fig. 6.4a, we display the single-qubit charge histogram derived from the simulated γ-ray events along with the measured histogram of discrete charge jumps on Q1. In Fig. 6.4b, we show the simulated two-qubit histograms for the γ-ray and muon events. Despite good agreement with the measured joint charge histograms across correlation probability, charge asymmetry, and 13/24 asymmetry, the simulated joint histogram for the smallest qubit separation of 340 μm displays a pronounced charge "jet" in quadrants 1 and 3. This feature arises from distant charge bursts that couple equally to the two qubits. We believe that in the experimental system this feature will be suppressed, as field lines from faraway bursts will close on the surrounding metal of the qubit enclosure, providing a natural cutoff in the response to distant charge. More sophisticated modeling of the qubit setup, including the detailed geometry of the

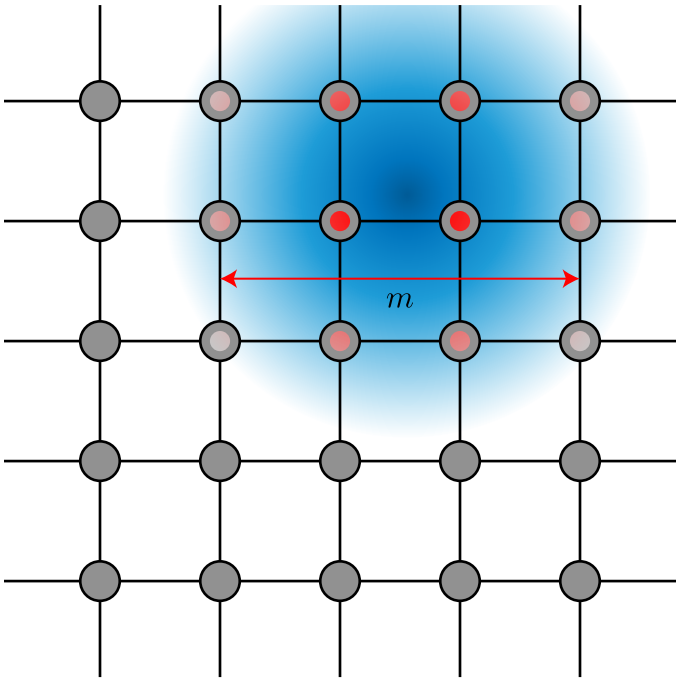

Figure 6.5: **Correlated errors in the surface code.** Schematic of a surface code array subjected to a correlated noise source, shown here in blue. The number m of qubits in a line to which the noise couples determines the sensitivity of the array to correlated errors.

sample enclosure, could capture this physics; however, this is beyond the scope of the current work.

6.7 Implications for fault tolerance

Here we briefly discuss the impact of correlated errors on error identification in the surface code; for a complete analysis, see Ref. [57]. The surface code consists of a two-dimensional fabric of qubits with nearest-neighbor connectivity. We define correlation degree m as the number of qubits in a line to which an error couples (see Fig. 6.5). It

can be shown that the fault-tolerant threshold p_m for correlated errors of degree m is given by

$$p_m \approx p^m, \tag{6.7}$$

where p is the fault-tolerant threshold for uncorrelated errors. Thus, for a threshold error level $p = 10^{-2}$, the threshold for correlated errors of degree 2 is $p_2 \approx 10^{-4}$; the threshold for correlated errors of degree 3 is $p_3 \approx 10^{-6}$, etc. These considerations must inform the design of large-scale qubit arrays that are susceptible to correlated errors: for a given error mechanism with a fixed spatial footprint, the need to protect against correlated errors will dictate how closely spaced the qubits can be.

Due to the exponential dependence of the fault-tolerant threshold on correlation degree, errors due to widespread quasiparticle poisoning are particularly damaging. In the following, we separately analyze in detail two additional correlated error mechanisms, in order of importance: correlated phase errors due to exponentially small (but nonzero) frequency shifts induced by correlated charge noise, and correlated bit-flip errors induced by pair production and charge reconfiguration in the substrate at the moment of particle impact.

6.8 Qubit phase flips from correlated charge noise

The devices used in this work were intentionally designed to be sensitive to charge. For a conventional transmon qubit optimized for high-fidelity gates, the sensitivity

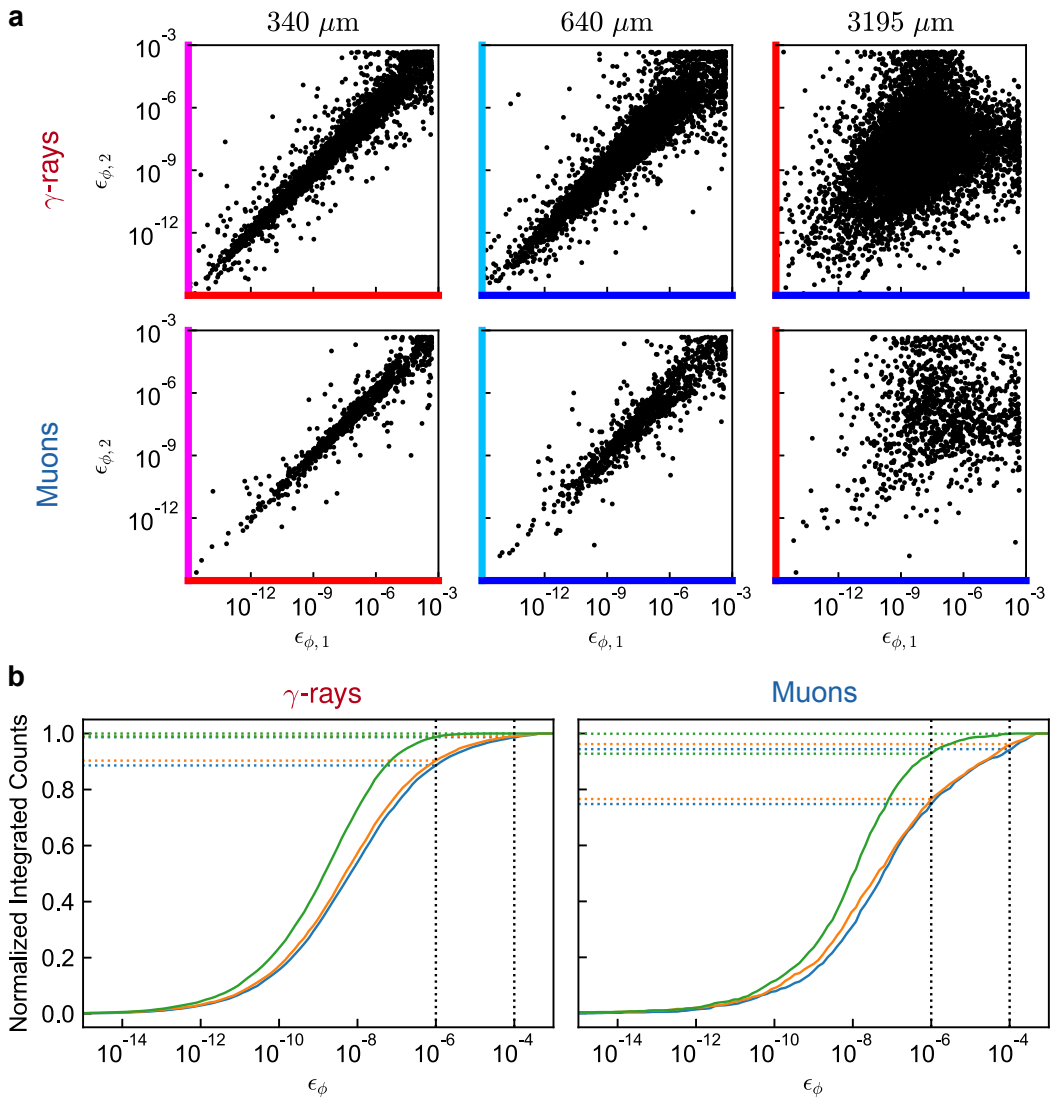

Figure 6.6: **Phase-flip errors from correlated charge fluctuations.** (**a**) Histograms of joint phase-flip errors from correlated charge noise induced by particle impacts. From left to right, the plots correspond to qubit pairs with center-to-center separation 340 μm, 640 μm, and 3195 μm; the top row corresponds to 7895 simulated γ-ray events, while the bottom row corresponds to 1162 simulated muon events. The qubit geometry and chip layout are identical to those considered throughout this work, but we take the more typical transmon parameters $E_J/h = 12.5$ GHz and $E_C = 250$ MHz. (**b**) Integrated histogram of correlated phase-flip errors from charge fluctuations induced by γ-ray (left) and muon (right) impacts. Blue, orange, and green traces correspond to qubit pairs with center-to-center separation 340 μm, 640 μm, and 3195 μm, respectively.

to charge is exponentially small, and charge noise has negligible impact on device coherence. However, due to the exponential sensitivity of the qubit array to correlated errors, it is necessary to carefully examine errors due to charge fluctuations that are sensed by multiple qubits. For a transmon qubit, the charge dispersion of the 01 transition $\Delta\omega_{01}$ (defined as half the peak-to-peak value) can be written as [28]

$$\Delta\omega_{01} = 16\sqrt{\frac{2}{\pi}}\frac{E_C}{\hbar}\left(\frac{\xi}{2}\right)^{3/4} e^{-\sqrt{8\xi}}\left[16\left(\frac{\xi}{2}\right)^{1/2}+1\right], \tag{6.8}$$

where we have defined $\xi \equiv E_J/E_C$. The qubit transition frequency depends on charge as follows:

$$\omega_{01} = \overline{\omega_{01}} - \Delta\omega_{01}\cos\left[\frac{\pi}{e}\left(q_0+\Delta q\right)\right], \tag{6.9}$$

where $\overline{\omega_{01}}$ is the mean qubit transition frequency, q_0 is a random offset charge, and Δq is a discrete change in offset charge due to particle impact in the qubit substrate. The mean-square frequency shift associated with the charge jump Δq is given by

$$\langle\delta\omega_{01}^2\rangle = 2\Delta\omega_{01}^2\sin^2\left(\pi\frac{\Delta q}{2e}\right), \tag{6.10}$$

where we have averaged over the random offset charge q_0. We can convert the frequency shift to a phase error accumulated during a surface-code cycle time τ_{sc} as follows:

$$\langle\phi^2\rangle = \langle\delta\omega_{01}^2\rangle\tau_{\text{sc}}^2. \tag{6.11}$$

Averaging over qubit states aligned along the six cardinal directions of the Bloch sphere, we find a phase-flip error probability ϵ_ϕ associated with charge jumps that is given by

$$\epsilon_\phi = \frac{\Delta\omega_{01}^2 \tau_{\rm sc}^2}{3} \sin^2\left(\pi \frac{\Delta q}{2e}\right). \tag{6.12}$$

In Fig. 6.6a we plot histograms of two-qubit phase-flip errors derived from the simulations presented in Fig. 6.4. Here we take $\tau_{\rm sc} = 1$ μs and we take conventional transmon parameters E_C/h = 250 MHz and E_J/h =12.5 GHz, corresponding to a mode frequency around 5 GHz and a charge dispersion $\Delta\omega_{01}/2\pi$ = 6.0 kHz. It is important to note that while our Ramsey-based charge measurement aliases charge fluctuations into the interval from -0.5e to +0.5e, for the purposes of dephasing the qubit will be sensitive to charge fluctuations in the interval from $-e$ to $+e$, as the surface code cycle time $\tau_{\rm sc}$ is short compared the characteristic quasiparticle parity dwell time. In Fig. 6.6b we plot integrated histograms of correlated phase-flip errors. We find that 11% (1.3%) and 9.7% (0.99%) of γ-ray events induce correlated errors above the 10^{-6} (10^{-4}) level in qubit pairs with separation 340 μm and 640 μm, respectively. For muon absorption, 25% (5.6%) and 23% (3.8%) of events induce simultaneous errors above the 10^{-6} (10^{-4}) level in qubit pairs with separation 340 μm and 640 μm, respectively. Finally, 7.2% of muon events induce correlated phase-flip errors above the 10^{-6} level for qubits separated by 3195 μm.

Based on the analysis presented above, correlated charge fluctuations can be a significant error mechanism for surface-code arrays implemented using the transmon qubit. The sensitivity of the transmon to charge noise can be further suppressed by increasing the ratio E_J/E_C; for fixed mode frequency, however, such an approach leads

to reduced anharmonicity $\omega_{01} - \omega_{12} \approx E_C/\hbar$ and increased leakage errors for fixed gate times. The need to protect against correlated phase-flip errors due to charge noise from particle impacts thus represents an important constraint to the design of fault-tolerant transmon qubit arrays.

6.9 Qubit bit flips from charge bursts

We identify two mechanisms for spurious qubit bit flips due to nonadiabatic reconfiguration of charge in the substrate following particle absorption. The first is associated with the sudden release of charge in the immediate aftermath of the impact, while the second is associated with single discrete charges that propagate from the impact site all the way to the qubit island. We discuss the relevant physics below.

The charges liberated by energy absorption in the substrate at point $\boldsymbol{r}$ very quickly emit phonons and relax to an energy where further phonon emission is kinematically forbidden; at this point, electrons and holes are moving ballistically at c_s, the sound speed in the substrate. We can fully characterize any charge distribution by specifying its multipole moments; the highest nonvanishing multipole moment will dominate the coupling to distant qubits. The electrons and holes liberated by the impact preserve charge neutrality; therefore, the monopole moment (net charge) is zero. There will, however, be a nonvanishing random dipole moment $\boldsymbol{d}(\boldsymbol{r})$ that grows linearly in time t with respect to the moment of impact:

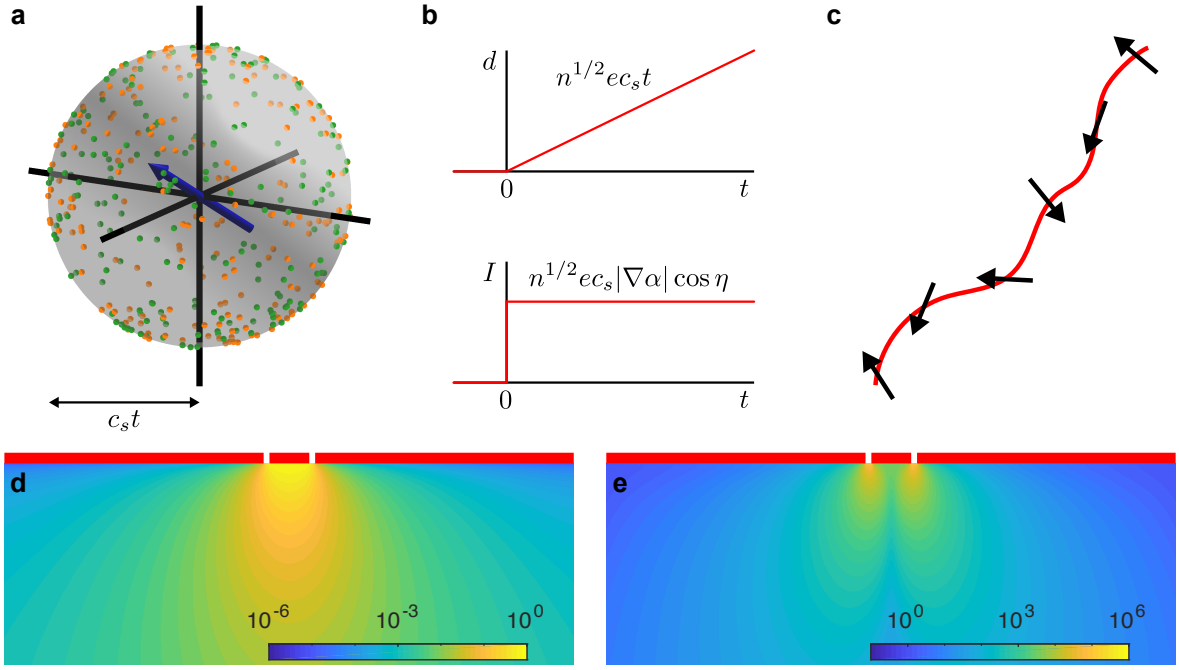

Figure 6.7: **Qubit response to nonadiabatic charge bursts.** (**a**) As electrons (green) and holes (orange) move ballistically with speed c_s from the site of pair production, the randomly oriented electric dipole moment associated with the charge distribution grows linearly with time t following the impact event. (**b**) Dipole moment d and effective current drive I to a neighboring qubit *versus* t. (**c**) The net response of the qubit to the nonadiabatic charge shifts associated with particle absorption in the substrate can be obtained by summing over the responses to the random electric dipoles that are nucleated along the particle track. (**d**) Dimensionless offset charge $\alpha(\boldsymbol{r})$ induced on the qubit island by a unit charge at point $\boldsymbol{r}$. Vertical extent of the plot corresponds to the 375 μm thickness of the chip, while the horizontal extent corresponds to 2 mm centered on the qubit island (not to scale). (**e**) Gradient $|\boldsymbol{\nabla}\alpha(\boldsymbol{r})|$, in units of m^{-1}.

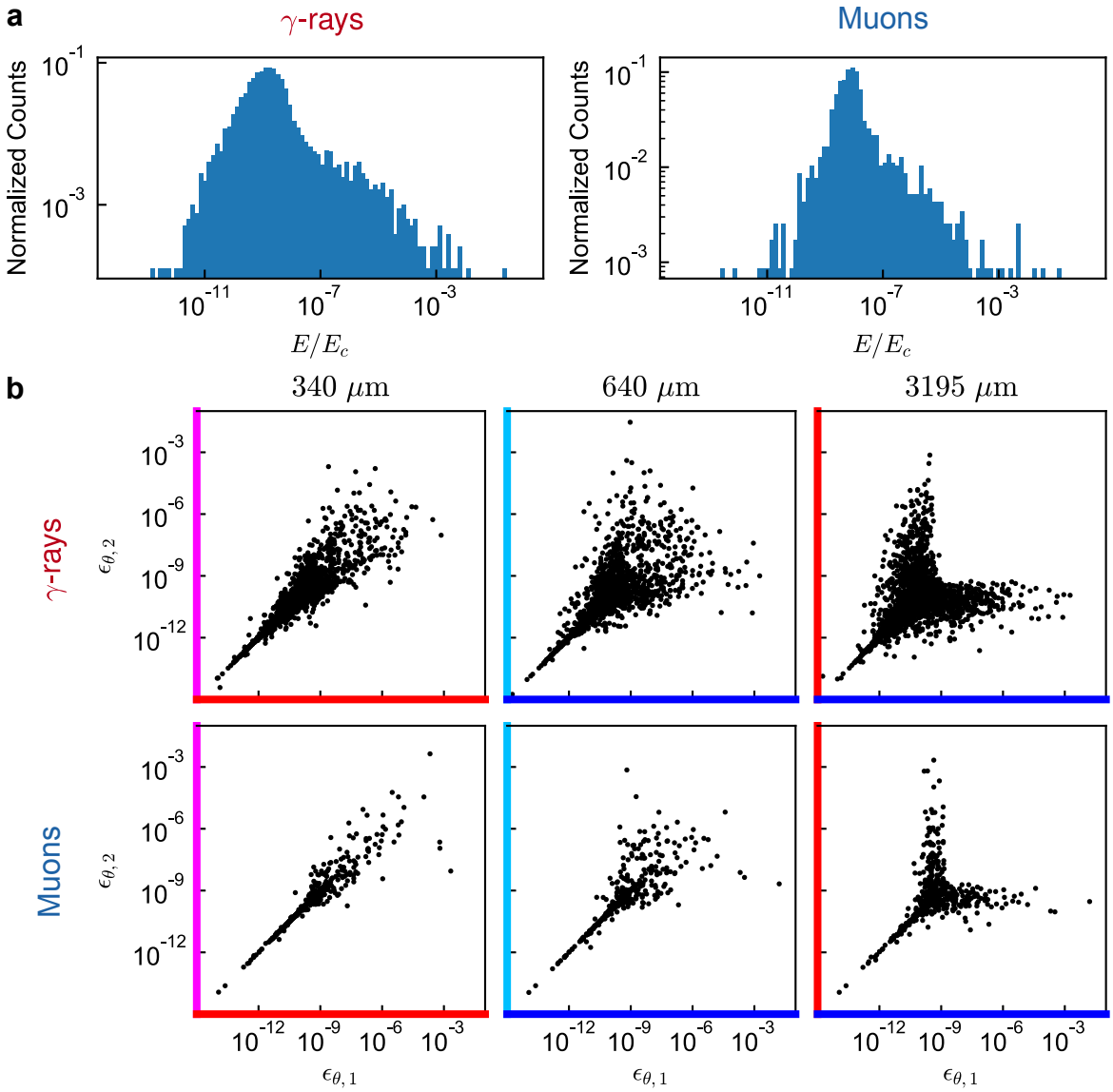

Figure 6.8: **Bit-flip errors from nonadiabatic charge bursts.** (**a**) Histogram of energy E deposited in the qubit mode by the charge transient associated with particle impact in the substrate. Energy is expressed in terms of the single-electron charging energy E_C. The plot on the left is calculated from 7895 simulated γ-ray absorption events, while the plot on the right is calculated from 1162 simulated muon absorption events. The qubit geometry and chip layout are identical to those considered throughout this work. (**b**) Histograms of joint error associated with the charge transients. From left to right, the plots correspond to qubit pairs with center-to-center separation 340 μm, 640 μm, and 3195 μm; the top row corresponds to γ-ray events, while the bottom row corresponds to muon events.

$$d(t) = n^{1/2} e\, c_s t, \tag{6.13}$$

where n is the number of discrete charges liberated by the impact event (see Fig. 6.7). This random dipole will induce an offset charge on the qubit island given by

$$Q(t) = \boldsymbol{d}(\boldsymbol{r}, t) \cdot \boldsymbol{\nabla}\alpha(\boldsymbol{r}), \tag{6.14}$$

where $\alpha(\boldsymbol{r})$ is the offset charge induced on the qubit island by a unit point charge at location $\boldsymbol{r}$. Note that the time dependence of $Q(t)$ is the same as that of $d(t)$: we have $Q(t) = 0$ for $t < 0$, and $Q(t) \propto t$ for $t > 0$. The abrupt transient at the moment of impact $t = 0$ is what drives qubit transitions. This transient corresponds to a current step:

$$I(t) = n^{1/2} e c_s \left|\boldsymbol{\nabla}\alpha\right| \cos\eta\, H(t), \tag{6.15}$$

where η is the angle between $\boldsymbol{\nabla}\alpha$ and the random dipole $\boldsymbol{d}$ and $H(t)$ is the Heaviside step function. This transient current deposits an energy in the qubit given by

$$\begin{aligned} E(\boldsymbol{r}) &= \frac{1}{2C}\left|\tilde{I}(\omega_{01})\right|^2 \\ &= \frac{n c_s^2 \left|\boldsymbol{\nabla}\alpha\right|^2}{\omega_{01}^2} E_C \cos^2\eta, \end{aligned} \tag{6.16}$$

where C is the self-capacitance of the qubit and $\tilde{I}(\omega_{01}) = \int_{-\infty}^{+\infty} I(t) e^{-i\omega_{01} t}\, dt$ is the Fourier transform of the current step evaluated at the qubit frequency.

We can equivalently express the coupling of the random dipole to the qubit in terms of a spurious rotation angle θ using the relation

$$E(\boldsymbol{r}) \approx \hbar\omega_{01}\,\frac{\theta^2}{4}. \tag{6.17}$$

We find

$$\theta(\boldsymbol{r}) = 2n^{1/2}c_s\,|\boldsymbol{\nabla}\alpha|\left(\frac{E_C}{\hbar\omega_{01}^3}\right)^{1/2}\cos\eta. \tag{6.18}$$

Similarly, we can express the coupling of the random dipole to the qubit as a bit-flip error probability $\epsilon_\theta = \theta^2/6$, where we have performed an average of the qubit response to the charge burst over qubit states aligned along the six cardinal directions on the Bloch sphere. We find

$$\epsilon_\theta(\boldsymbol{r}) = \frac{2}{3}nc_s^2\,|\boldsymbol{\nabla}\alpha|^2\,\frac{E_C}{\hbar\omega_{01}^3}\cos^2\eta. \tag{6.19}$$

For a γ-ray or muon track, we expect to have energy deposited over a range of points in the substrate at times that are short compared to the qubit oscillation period. In this case, we need to add the rotations induced by the separate energy deposits. Using this model, we have calculated single-qubit and joint error probabilities associated with γ-ray and muon absorption in the substrate. In Fig. 6.8a we plot the total energy deposited in the qubit in terms of E_C for γ-ray and muon tracks; here, we use the γ-ray and muon tracks calculated using GEANT4 as described above, the electrostatic response function $\alpha(\boldsymbol{r})$ calculated for our geometry, and we take the typical qubit frequency $\omega_{01}/2\pi = 5$ GHz. In Fig.6.8b, we plot joint errors for this set of γ-

ray and muon tracks. Again we take a qubit frequency of 5 GHz and we take a charging energy $E_C/h = 250$ MHz. We find that 1.2% and 0.7% of γ-ray events induce simultaneous errors above the 10^{-8} level in qubit pairs with separation 340 μm and 640 μm, respectively. For muon absorption, 4.0% and 3.1% of events induce simultaneous errors above the 10^{-8} level in qubit pairs with separation 340 μm and 640 μm, respectively.

Following the initial transient associated with particle absorption, a charge-insensitive qubit will follow the slow drift of distant charge in the substrate adiabatically. However, it is possible that a charge that propagates all the way to the qubit island will give rise to a nonadiabatic shift in island charge as it passes through a region where $|\boldsymbol{\nabla}\alpha(\boldsymbol{r})|$ is large. The crossover from adiabaticity to nonadiabaticity can be expressed as

$$\begin{aligned} \frac{d\omega_{01}}{dt} &\sim \omega_{01}^2 \\ \frac{c_s\,|\boldsymbol{\nabla}\alpha(\boldsymbol{r})|}{\hbar}\,E_C &\sim \omega_{01}^2. \end{aligned} \tag{6.20}$$

This relation defines a surface surrounding the qubit island; charges that cross this surface will induce a sudden, nonadiabatic shift in offset charge, resulting in an error of order $E_C/\hbar\omega_{01}$. For the electrostatic response function $\alpha(\boldsymbol{r})$ associated with our qubit geometry, we find that rotation errors induced by direct charge impingement on the qubit island will be negligible; however, this error mechanism could be important for

other device geometries or parameters.

6.10 Characterization of background radiation

We use a 1.5" NaI scintillation detector to characterize the spectrum of background radioactivity in the qubit laboratory in Madison. We use sealed sources of ^{137}Cs and ^{60}Co with known activity to calibrate the detector at the photopeak energies 662 keV, 1.17 MeV, and 1.33 MeV. To bootstrap the calibration to higher energy, we use the 1.37 and 2.75 MeV γ-ray emission from ^{24}Na obtained by proton irradiation of a piece of Al in the UW-Madison Cyclotron Laboratory. In Fig. 6.9 we plot the measured γ-ray spectrum, along with the γ-ray spectrum measured with a 3" NaI detector in the underground laboratory at LNGS in Gran Sasso, which was used as input to the γ-ray simulations performed using GEANT4. Here the spectrum measured in Madison has been scaled by a factor 5.2 to account for the smaller detector dimension [133], facilitating direct comparison with the spectrum from LNGS. Apart from a factor 2.8 difference in absolute rate, the spectra are similar. Fitting the Madison spectrum with known decay chains yields the contributions from ^{40}K (30%), ^{232}Th (50%), and ^{238}U (20%). The background activity is dominated by the 1.46 MeV γ emission of ^{40}K and the 2.61 MeV γ emission of ^{208}Tl, both of which are known to be common radioactive contaminants. Again, the spectrum of energy deposited in the qubit chip is insensitive to the fine details of the spectrum of background radiation used for the simulations.

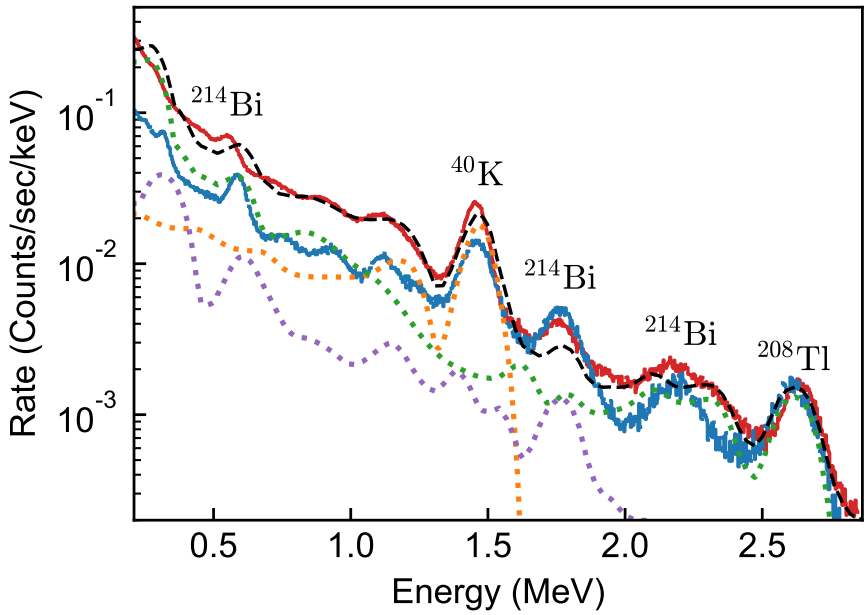

Figure 6.9: **Spectrum of background radioactivity.** Red: spectrum of environmental γ radiation measured in the laboratory in Madison with a 1.5" NaI scintillation detector. Blue: spectrum of environmental γ radiation measured in LNGS with a 3" NaI scintillation detector and used for the simulations (see Sec. 6.6). The Madison spectrum has been scaled by a factor 5.2 to account for the smaller detector dimension [133], allowing a direct comparison with the spectrum from LNGS. The Madison spectrum is fit (dashed, black) with the contributions from ^{40}K (dotted, orange), ^{232}Th (dotted, green), and ^{238}U (dotted, purple) using an unbinned extended maximum likelihood fit performed with the RooFit toolkit. The distinguishable peaks of ^{40}K at 1.460 MeV and ^{208}Tl at 2.614 MeV, along with three peaks from ^{214}Bi, can be seen as dominant contributors to the spectra. The integrated γ-ray flux measured in Madison is a factor 2.8 larger than that measured at LNGS.

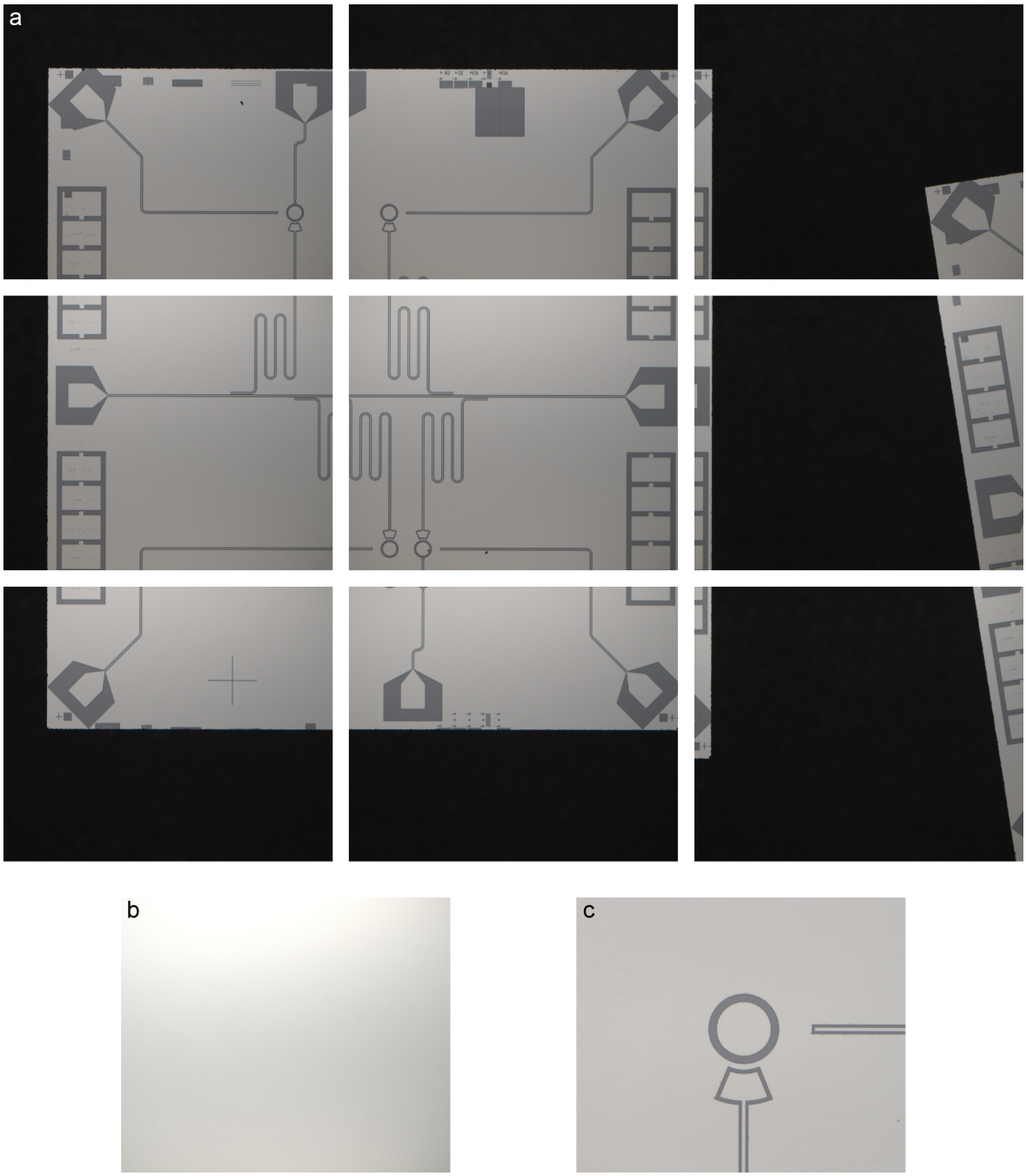

Figure 6.10: **Raw device images.** (**a**) The nine images stitched together to make Fig. 5.1a. (**b**) A blank section of the wafer was imaged to calibrate the vignetting in each image. This image was divided into each of the nine images in (a). (**c**) The unedited image from Fig. 5.1b.

From the γ-ray spectrum measured in Madison and the GEANT4 simulations, we expect a rate of γ impacts on the qubit chip of 9 mHz. As we discuss above, from our measured rate of offset charge jumps, we infer a rate of γ impacts on the chip of 19.8(5) mHz. The factor 2 discrepancy could indicate a dominant local source of radioactivity within the qubit cryostat: the qubit chip is closely surrounded by the aluminum sample enclosure, copper stage plates, mu-metal shields, stainless steel vacuum cans, etc., all of which are potential emitters of low-level γ radiation. A systematic study of the various contributions to the γ-ray impact rate in the qubit chip will the the focus of future work.

6.11 Raw device images

The composite image shown in Fig. 5.1a is made by stitching nine separate microscope images together in order to cover a larger field of view. Before stitching, a single image was taken of a blank part of the wafer and subsequently divided into each of the nine images in order to remove a constant vignette seen in each image. After aligning the nine images by hand, Adobe Photoshop's Auto-Blend Layers command was used to combine them into a single image. This tool masks the images around features it automatically detects to make them look smooth, and adjusts the brightness and contrast to blend edges. In Fig. 5.1, we have also edited out bits of surface contamination using Photoshop's Clone tool for easier viewing. Finally, the micrographs were false-colored

to highlight different parts of the circuit. The unedited images can be found in Fig. 6.10.

Bibliography

[1] Bloch, F. Nuclear induction. *Phys. Rev.* **70**, 460–474 (1946). 1

[2] Saffman, M., Walker, T. G. & Mølmer, K. Quantum information with Rydberg atoms. *Rev. Mod. Phys.* **82**, 2313–2363 (2010). 2

[3] Saffman, M. Quantum computing with atomic qubits and Rydberg interactions: progress and challenges. *J. Phys. B* **49**, 202001 (2016).

[4] Auger, J. M., Bergamini, S. & Browne, D. E. Blueprint for fault-tolerant quantum computation with rydberg atoms. *Phys. Rev. A* **96**, 052320 (2017). 2

[5] Cirac, J. I. & Zoller, P. Quantum computations with cold trapped ions. *Phys. Rev. Lett.* **74**, 4091–4094 (1995). 2

[6] Brown, K., Kim, J. & Monroe, C. Co-designing a scalable quantum computer with trapped atomic ions. *npj Quantum Information* **2** (2016). 2

[7] Loss, D. & DiVincenzo, D. P. Quantum computation with quantum dots. *Phys. Rev. A* **57**, 120–126 (1998). 3

[8] Zwanenburg, F. A. *et al.* Silicon quantum electronics. *Rev. Mod. Phys.* **85**, 961–1019 (2013).

[9] Simmons, C. B. *et al.* Single-electron quantum dot in Si/SiGe with integrated charge sensing. *Appl. Phys. Lett.* **91**, 213103, `https://doi.org/10.1063/1.2816331` (2007). 3

[10] Monroe, C. Quantum information processing with atoms and photons. *Nature* **416**, 238–246 (2002). 3

[11] Walmsley, I. A. Toward quantum-information processing with photons. *Science* **307**, 1733–1734 (2005).

[12] Kok, P. *et al.* Linear optical quantum computing with photonic qubits. *Rev. Mod. Phys.* **79**, 135–174 (2007).

[13] Milburn, G. J. Photons as qubits. *Physica Scripta* **T137**, 014003 (2009). 3

[14] Devoret, M. & Martinis, J. Implementing qubits with superconducting integrated circuits. *Quantum Inf. Process.* **3**, 163 (2004). 3

[15] Clarke, J. & Wilhelm, F. Superconducting quantum bits. *Nature* **453**, 1031–1042 (2008).

[16] Devoret, M. H. & Schoelkopf, R. J. Superconducting circuits for quantum information: An outlook. *Science* **339**, 1169–1174 (2013).

[17] Gambetta, J. M., Chow, J. M. & Steffen, M. Building logical qubits in a superconducting quantum computing system. *npj Quantum Information* **3** (2017).

[18] Liu, W.-Y., Zheng, D.-N. & Zhao, S.-P. Superconducting quantum bits. *Chinese Physics B* **27**, 027401 (2018).

[19] Neill, C. *et al.* A blueprint for demonstrating quantum supremacy with superconducting qubits. *Science* **360**, 195–199 (2018). 3, 70

[20] Josephson, B. Possible new effects in superconductive tunnelling. *Phys. Lett.* **1**, 251 (1962). 3

[21] Josephson, B. D. The discovery of tunnelling supercurrents. *Rev. Mod. Phys.* **46**, 251–254 (1974).

[22] Anderson, P. W. & Rowell, J. M. Probable observation of the josephson superconducting tunneling effect. *Phys. Rev. Lett.* **10**, 230–232 (1963). 3

[23] Barone, A. & Paterno, G. *Physics and applications of the Josephson effect* (Wiley, New York, 1982). 5

[24] Schmidt, V. V. *The Physics of Superconductors: Introduction to Fundamentals and Applications* (Springer Berlin Heidelberg, 1997).

[25] Tinkham, M. *Introduction to Superconductivity* (McGraw-Hill, New York, 1996). 5, 20

[26] McCumber, D. E. Effect of ac impedance on dc voltage-current characteristics of superconductor weak-link junctions. *J. Appl. Phys.* **39**, 3113–3118 (1968). 6

[27] Stewart, W. C. Current-voltage characteristics of Josephson junctions. *Appl. Phys. Lett.* **12**, 277–280 (1968). 6

[28] Koch, J. *et al.* Charge-insensitive qubit design derived from the Cooper pair box. *Phys. Rev. A* **76**, 042319 (2007). 14, 25, 39, 56, 70, 74, 134

[29] Vool, U. & Devoret, M. Introduction to quantum electromagnetic circuits. *International Journal of Circuit Theory and Applications* **45**, 897–934 (2017). 14

[30] Chen, Z. *et al.* Measuring and suppressing quantum state leakage in a superconducting qubit. *Phys. Rev. Lett.* **116**, 020501 (2016). 26

[31] Göppl, M. *et al.* Coplanar waveguide resonators for circuit quantum electrodynamics. *J. Appl. Phys.* **104**, 113904 (2008). 30

[32] Sank, D. *Fast, Accurate State Measurement in Superconducting Qubits*. Ph.D. thesis, UCSB (2014). 40

[33] Schoelkopf, R. J., Clerk, A. A., Girvin, S. M., Lehnert, K. W. & Devoret, M. H. *Quantum Noise*, chap. Qubits as spectrometers of quantum noise. Nato ASI (Kluwer, Dordrecht, 2002). Edited by Yu.V. Nazarov and Ya.M. Blanter. 47

[34] Milotti, E. 1/f noise: a pedagogical review `0204033` (2002). 50

[35] Kumar, P. *et al.* Origin and reduction of $1/f$ magnetic flux noise in superconducting devices. *Phys. Rev. Appl.* **6**, 041001 (2016). 52

[36] Martinis, J. M. & Megrant, A. UCSB final report for the csq program: Review of decoherence and materials physics for superconducting qubits `1410.5793` (2014). 53

[37] Martinis, J. M. *et al.* Decoherence in Josephson qubits from dielectric loss. *Phys. Rev. Lett.* **95**, 210503 (2005). 53, 79

[38] Barends, R. *et al.* Coherent Josephson qubit suitable for scalable quantum integrated circuits. *Phys. Rev. Lett.* **111**, 080502 (2013). 53

[39] Paik, H. *et al.* Observation of high coherence in Josephson junction qubits measured in a three-dimensional circuit QED architecture. *Phys. Rev. Lett.* **107**, 240501 (2011). 53

[40] Minev, Z. K., Pop, I. M. & Devoret, M. H. Planar superconducting whispering gallery mode resonators. *Appl. Phys. Lett.* **103**, 142604 (2013). 53

[41] Klimov, P. V. *et al.* Fluctuations of energy-relaxation times in superconducting qubits. *Phys. Rev. Lett.* **121**, 090502 (2018). 53

[42] Lisenfeld, J. *et al.* Electric field spectroscopy of material defects in transmon qubits. *npj Quantum Information* **5** (2019). 53

[43] Bilmes, A. *et al.* Resolving the positions of defects in superconducting quantum bits. *Scientific Reports* **10** (2020). 53

[44] Wisbey, D. *et al.* Effect of metal/substrate interfaces on radio-frequency loss in superconducting coplanar waveguides (2010). 54

[45] Dunsworth, A. *et al.* Characterization and reduction of capacitive loss induced by sub-micron josephson junction fabrication in superconducting qubits. *Applied Physics Letters* **111**, 022601 (2017). 54

[46] Sears, A. P. *et al.* Photon shot noise dephasing in the strong-dispersive limit of circuit QED. *Phys. Rev. B* **86**, 180504 (2012). 55

[47] Wang, Z. *et al.* Cavity attenuators for superconducting qubits. *Phys. Rev. Applied* **11**, 014031 (2019). 55

[48] Jr., E. L. *et al.* Digital coherent control of a superconducting qubit `arXiv: 1806.07930` (2018). 55

[49] Houck, A. A. *et al.* Controlling the spontaneous emission of a superconducting transmon qubit. *Phys. Rev. Lett.* **101**, 080502 (2008). 57

[50] Jeffrey, E. *et al.* Fast accurate state measurement with superconducting qubits. *Phys. Rev. Lett.* **112**, 190504 (2014). 57, 100

[51] Rafferty, O. *et al.* Spurious antenna modes of the transmon qubit `2103.06803` (2021). 57

[52] Catelani, G. *et al.* Quasiparticle relaxation of superconducting qubits in the presence of flux. *Phys. Rev. Lett.* **106**, 077002 (2011). 58

[53] Ristè, D. *et al.* Deterministic entanglement of superconducting qubits by parity measurement and feedback. *Nature* **1502**, 350–354 (2013). 59

[54] Catelani, G., Schoelkopf, R. J., Devoret, M. H. & Glazman, L. I. Relaxation and frequency shifts induced by quasiparticles in superconducting qubits. *Phys. Rev. B* **84** (2011). 60, 110

[55] Houzet, M., Serniak, K., Catelani, G., Devoret, M. H. & Glazman, L. I. Photon-assisted charge-parity jumps in a superconducting qubit. *Phys. Rev. Lett.* **123**, 107704 (2019). 60

[56] Fowler, A. G., Mariantoni, M., Martinis, J. M. & Cleland, A. N. Surface codes: Towards practical large-scale quantum computation. *Phys. Rev. A* **86**, 032324 (2012). 66, 67, 99, 100

[57] Faoro, L. & Ioffe, L. B. Critical behavior of surface code statistical models. *In preparation* (2020). 67, 101, 110, 131

[58] Christensen, B. G. *et al.* Anomalous charge noise in superconducting qubits. *Phys. Rev. B* **100**, 140503 (2019). 69, 85, 104

[59] Boixo, S. *et al.* Characterizing quantum supremacy in near-term devices. *Nat. Phys.* **14**, 595–600 (2018). 70

[60] Fowler, A. G. Coping with qubit leakage in topological codes. *Phys. Rev. A* **88**, 042308 (2013). 70

[61] Douçot, B. & Ioffe, L. B. Physical implementation of protected qubits. *Rep. Prog. Phys.* **75**, 072001 (2012). 70

[62] Bell, M. T., Paramanandam, J., Ioffe, L. B. & Gershenson, M. E. Protected josephson rhombus chains. *Phys. Rev. Lett.* **112**, 167001 (2014). 70

[63] Bell, M. T., Zhang, W., Ioffe, L. B. & Gershenson, M. E. Spectroscopic evidence of the Aharonov-Casher effect in a cooper pair box. *Phys. Rev. Lett.* **116**, 107002 (2016). 70

[64] Groszkowski, P. *et al.* Coherence properties of the $0-\pi$ qubit `arXiv:1708.02886` (2018). 70

[65] Kim, M. *et al.* Decoherence of near-surface nitrogen-vacancy centers due to electric field noise. *PRL* **115**, 087602 (2015). 70

[66] Brownnutt, M., Kumph, M., Rabl, P. & Blatt, R. Ion-trap measurements of electric-field noise near surfaces. *RMP* **87**, 1419–1482 (2015). 70

[67] Freeman, B. M., Schoenfield, J. S. & Jiang, H. Comparison of low frequency charge noise in identically patterned Si/SiO2 and Si/SiGe quantum dots. *Appl. Phys. Lett.* **108**, 253108 (2016). 70, 71

[68] Kuzmin, L. S., Delsing, P., Claeson, T. & Likharev, K. K. Single-electron charging effects in one-dimensional arrays of ultrasmall tunnel junctions. *Phys. Rev. Lett.* **62**, 2539–2542 (1989). 70

[69] Zimmerli, G., Eiles, T. M., Kautz, R. L. & Martinis, J. M. Noise in the Coulomb blockade electrometer. *Appl. Phys. Lett.* **61**, 237–239 (1992).

[70] Zimmerli, G., Kautz, R. L. & Martinis, J. M. Voltage gain in the single-electron transistor. *Appl. Phys. Lett.* **61**, 2616–2618 (1992).

[71] Visscher, E. H., Verbrugh, S. M., Lindeman, J., Hadley, P. & Mooij, J. E. Fabrication of multilayer single-electron tunneling devices. *Appl. Phys. Lett.* **66**, 305–307 (1995).

[72] Verbrugh, S. M., Benhamadi, M. L., Visscher, E. H. & Mooij, J. E. Optimization of island size in single electron tunneling devices: Experiment and theory. *Journal of Applied Physics* **78**, 2830–2836 (1995). 79

[73] Song, D., Amar, A., Lobb, C. J. & Wellstood, F. C. Advantages of superconducting Coulomb-blockade electrometers. *IEEE Trans. Appl. Supercond.* **5**, 3085–3089 (1995).

[74] Wolf, H. *et al.* Investigation of the offset charge noise in single electron tunneling devices. *IEEE Transactions on Instrumentation and Measurement* **46**, 303–306 (1997). 79

[75] Kenyon, M., Lobb, C. J. & Wellstood, F. C. Temperature dependence of low-frequency noise in Al-Al_2O_3-Al single-electron transistors. *J. Appl. Phys.* **88**, 6536–6540 (2000). 71

[76] Gustafsson, M. V., Pourkabirian, A., Johansson, G., Clarke, J. & Delsing, P. Thermal properties of charge noise sources. *PRB* **88**, 245410 (2013). 70

[77] Nakamura, Y., Pashkin, Y. A., Yamamoto, T. & Tsai, J. S. Charge echo in a Cooper-pair box. *Phys. Rev. Lett.* **88**, 047901 (2002). 71

[78] Dutta, P. & Horn, P. M. Low-frequency fluctuations in solids: $1/f$ noise. *Rev. Mod. Phys.* **53**, 497–516 (1981). 71

[79] Clemens Müller, J. L., Jared H. Cole. Towards understanding two-level-systems in amorphous solids - insights from quantum circuits. *arXiv:1705.01108 [cond-mat.mes-hall]* (2017). 71

[80] Ristè, D. *et al.* Millisecond charge-parity fluctuations and induced decoherence in a superconducting transmon qubit. *Nat. Commun.* **4**, 1913 (2013). 73, 74, 78, 79, 87, 88, 89, 109

[81] Serniak, K. *et al.* Hot nonequilibrium quasiparticles in transmon qubits. *Phys. Rev. Lett.* **121**, 157701 (2018). 73, 74, 78, 79, 87, 88, 89, 109

[82] Schreier, J. *et al.* Suppressing charge noise decoherence in superconducting charge qubits. *Phys. Rev. B* **77**, 180502(R) (2008). 74

[83] Lutchyn, R. M., Glazman, L. I. & Larkin, A. I. Kinetics of the superconducting charge qubit in the presence of a quasiparticle. *PRB* **74**, 064515 (2006). 74

[84] Yan, F. *et al.* Spectroscopy of low-frequency noise and its temperature dependence in a superconducting qubit. *Phys. Rev. B* **85**, 174521 (2012). 78

[85] Quintana, C. M. *et al.* Observation of classical-quantum crossover of $1/f$ flux noise and its paramagnetic temperature dependence. *Phys. Rev. Lett.* **118**, 057702 (2017). 78

[86] Schoelkopf, R. J., Wahlgren, P., Kozhevnikov, A. A., Delsing, P. & Prober, D. E. The radio-frequency single-electron transistor (rf-SET): A fast and ultrasensitive electrometer. *Science* **280**, 1238 (1998). 79

[87] Aassime, A., Johansson, G., Wendin, G., Schoelkopf, R. J. & Delsing, P. Radio-frequency single-electron transistor as readout device for qubits: Charge sensitivity and backaction. *Phys. Rev. Lett.* **86**, 3376–3379 (2001). 79

[88] Nolt, I. G. *et al.* Cosmic-ray backgrounds in infrared bolometers. *International Journal of Infrared and Millimeter Waves* **6**, 707–728 (1985). 82

[89] Lanfranchi, M., Carli, B., Gignoli, A., Lee, C. & Ridolfi, M. Cosmic-ray flux detected by an ir bolometer operated on board of a stratospheric aircraft. *Infrared Physics & Technology* **40**, 379–386 (1999).

[90] Karatsu, K. *et al.* Mitigation of cosmic ray effect on microwave kinetic inductance detector arrays. *Appl. Phys. Lett.* **114**, 032601 (2019). 82

[91] Gorodokin, V. & Zemlyanov, D. Metallic contamination in silicon processing. In *2004 23rd IEEE Convention of Electrical and Electronics Engineers in Israel*, 157–160 (2004). 82

[92] Constant, I., Tardif, F. & Derrien, J. Deposition and removal of sodium contamination on silicon wafers. *Semiconductor Science and Technology* **15**, 61–66 (2000). 82

[93] Turchette, Q. A. *et al.* Heating of trapped ions from the quantum ground state. *Phys. Rev. A* **61**, 063418 (2000). 83

[94] Deslauriers, L. *et al.* Zero-point cooling and low heating of trapped $^{111}Cd^{+}$ ions. *Phys. Rev. A* **70**, 043408 (2004). 83

[95] Wilen, C. D. *et al.* Correlated charge noise and relaxation errors in superconducting qubits. *Nature* **594**, 369–373 (2021). 99, 115

[96] Barends, R. *et al.* Superconducting quantum circuits at the surface code threshold for fault tolerance. *Nature* **508**, 500–503 (2014). 100

[97] Sheldon, S. *et al.* Characterizing errors on qubit operations via iterative randomized benchmarking. *Phys. Rev. A* **93**, 012301 (2016). 100

[98] Walter, T. *et al.* Rapid high-fidelity single-shot dispersive readout of superconducting qubits. *Phys. Rev. Applied* **7**, 054020 (2017). 100

[99] Opremcak, A. *et al.* High-fidelity measurement of a superconducting qubit using an on-chip microwave photon counter. *Phys. Rev. X* **11** (2021). 100

[100] Vepsäläinen, A. P. *et al.* Impact of ionizing radiation on superconducting qubit coherence. *Nature* **584**, 551–556 (2020). 106

[101] Agostinelli, S. *et al.* GEANT4–a simulation toolkit. *Nucl. Instrum. Methods. Phys. Res. A* **506**, 250–303 (2003). 106, 122

[102] Allison, J. *et al.* GEANT4 developments and applications. *IEEE Trans. Nucl. Sci.* **53**, 270–278 (2006).

[103] Allison, J. *et al.* Recent developments in GEANT4. *Nucl. Instrum. Methods. Phys. Res. A* **835**, 186–225 (2016). 106, 122

[104] Shukla, P. & Sankrith, S. Energy and angular distributions of atmospheric muons at the Earth. `arXiv:1606.06907` (2018). 106, 125

[105] Ramanathan, K. & Kurinsky, N. Ionization yield in silicon for eV-scale electron-recoil processes. *Physical Review D* **102** (2020). 108

[106] Brandt, D. *et al.* Semiconductor phonon and charge transport Monte Carlo simulation using GEANT4. `arXiv:1403.4984` (2014). 108

[107] Kelsey, M., Agnese, R., Brandt, D. & Redl, P. G4CMP: GEANT4 add-on framework for phonon and charge-carrier physics. https://github.com/kelseymh/G4CMP (2020). 108

[108] Moffatt, R. A. *et al.* Spatial imaging of charge transport in silicon at low temperature. *App. Phys. Lett.* **114**, 032104 (2019). 108, 126

[109] Martinis, J. M., Ansmann, M. & Aumentado, J. Energy decay in superconducting Josephson-junction qubits from nonequilibrium quasiparticle excitations. *Phys. Rev. Lett.* **103**, 097002 (2009). 109

[110] Lenander, M. *et al.* Measurement of energy decay in superconducting qubits from nonequilibrium quasiparticles. *Phys. Rev. B* **84**, 024501 (2011).

[111] Wenner, J. *et al.* Excitation of superconducting qubits from hot nonequilibrium quasiparticles. *Phys. Rev. Lett.* **110**, 150502 (2013).

[112] Wang, C. *et al.* Measurement and control of quasiparticle dynamics in a superconducting qubit. *Nat. Commun.* **5**, 5836 (2014). 109, 119

[113] Dell'Oro, S., Marcocci, S., Viel, M. & Vissani, F. Neutrinoless double beta decay: 2015 review. *Adv. High Energy Phys.* **2016**, 1–37 (2016). 112

[114] Poda, D. & Giuliani, A. Low background techniques in bolometers for double-beta decay search. *Int. J. Mod. Phys. A* **32**, 1743012 (2017). 112

[115] Baudis, L. The search for dark matter. *Eur. Rev.* **26**, 70–81 (2018). 112

[116] Pirro, S. & Mauskopf, P. Advances in bolometer technology for fundamental physics. *Annu. Rev. Nucl. Part. Sci.* **67**, 161–181 (2017). 112

[117] Szücs, T. *et al.* Background in γ-ray detectors and carbon beam tests in the Felsenkeller shallow-underground accelerator laboratory. *Eur. Phys. J. A* **55**, 174 (2019). 112

[118] Aglietta, M. *et al.* Muon "depth-intensity" relation measured by the lvd underground experiment and cosmic-ray muon spectrum at sea level. *Phys. Rev. D* **58**, 092005 (1998).

[119] Jillings, C. The SNOLAB science program. *J. Phys. Conf. Ser.* **718**, 062028 (2016). 112

[120] Alessandria, F. *et al.* Validation of techniques to mitigate copper surface contamination in CUORE. *Astropart. Phys.* **45**, 13–22 (2013). 113

[121] Aprile, E. *et al.* Material screening and selection for XENON100. *Astropart. Phys.* **35**, 43–49 (2011).

[122] Busto, J., Gonin, Y., Hubert, F., Hubert, P. & Vuilleumier, J.-M. Radioactivity measurements of a large number of adhesives. *Nucl. Instrum. Methods. Phys. Res. A* **492**, 35–42 (2002).

[123] ILIAS Database. `http://radiopurity.in2p3.fr`.

[124] Cardani, L. *et al.* Reducing the impact of radioactivity on quantum circuits in a deep-underground facility. `arXiv:2005.02286` (2020). 113

[125] Aumentado, J., Keller, M. W., Martinis, J. M. & Devoret, M. H. Nonequilibrium quasiparticles and $2e$ periodicity in single-Cooper-pair transistors. *Phys. Rev. Lett.* **92**, 066802 (2004). 113

[126] Patel, U., Pechenezhskiy, I. V., Plourde, B. L. T., Vavilov, M. G. & McDermott, R. Phonon-mediated quasiparticle poisoning of superconducting microwave resonators. *Phys. Rev. B* **96**, 220501(R) (2017). 113

[127] Martinis, J. M. Saving superconducting quantum processors from qubit decay and correlated errors generated by gamma and cosmic rays. `arXiv:2012.06137` (2020). 113

[128] Beckman, S. M. *et al.* Development of cosmic ray mitigation techniques for the LiteBIRD space mission. In Zmuidzinas, J. & Gao, J.-R. (eds.) *Millimeter, Submillimeter, and Far-Infrared Detectors and Instrumentation for Astronomy IX*, vol. 10708. International Society for Optics and Photonics (SPIE, 2018). 113

[129] Dolan, G. J. Offset masks for lift-off photoprocessing. *Appl. Phys. Lett.* **31**, 337–339 (1977). 116

[130] Jacoboni, C. & Reggiani, L. The Monte Carlo method for the solution of charge transport in semiconductors with applications to covalent materials. *Rev. Mod. Phys.* **55**, 645–705 (1983). 125

[131] Sundqvist, K. M. *Carrier Transport and Related Effects in Detectors of the Cryogenic Dark Matter Search.* Ph.D. thesis, UC-Berkeley (2012). 126

[132] Moffatt, R. *Two-Dimensional Spatial Imaging of Charge Transport in Germanium Crystals at Cryogenic Temperatures.* Ph.D. thesis, Stanford University (2016). 126, 130

[133] Courbois, T., Van Gelderen, L. & Leutz, H. Background, peak efficiency and dimensions of NaI(Tl)-crystals. *Nucl. Instrum. Methods* **69**, 93–100 (1969). 142, 143